Trodimenzionalna numerička simulacija procesa izgaranja u komori izgaranja mlaznog motora

Delić, Fran

University of Zagreb
Faculty of Mechanical Engineering and Naval Architecture

MASTER'S THESIS

Fran Delić

Zagreb, 2019

University of Zagreb
Faculty of Mechanical Engineering and Naval Architecture

MASTER'S THESIS

THREE-DIMENSIONAL NUMERICAL SIMULATION OF COMBUSTION IN A JET ENGINE COMBUSTION CHAMBER

Mentor:
prof. dr. sc. Hrvoje Jasak

Student:
Fran Delić

Zagreb, 2019

I hereby declare that this thesis is entirely the result of my own work except where otherwise indicated. I have fully cited all used sources and I have only used the ones given in the list of references.

I am profoundly thankful to prof. Hrvoje Jasak for all the guidance, help and suggestions while writing this thesis. His lectures sparked my interest in CFD, and his mentorship pushed me to do my best.

I would also like the thank the entire FSB CFD team, especially Tessa Uroić, for their continuing support. No problem was too difficult, or too trivial, for their help.

To my colleagues from room 816, I would like to thank you for creating a fun and positive work environment.

Finally, I would like to thank my family and my girlfriend Sara for all their patience, support and love, not only while writing this thesis, but during my university years.

SVEUČILIŠTE U ZAGREBU
FAKULTET STROJARSTVA I BRODOGRADNJE
Središnje povjerenstvo za završne i diplomske ispite
Povjerenstvo za završne i diplomske ispite studija zrakoplovstva

Sveučilište u Zagrebu Fakultet strojarstva i brodogradnje	
Datum	Prilog
Klasa:	
Ur.broj:	

DIPLOMSKI ZADATAK

Student: **Fran Delić** Mat. br.: 0035190751

Naslov rada na hrvatskom jeziku: **Trodimenzionalna numerička simulacija procesa izgaranja u komori izgaranja mlaznog motora**

Naslov rada na engleskom jeziku: **Three-dimensional numerical simulation of combustion in a jet engine combustion chamber**

Opis zadatka:

Numerical simulation of combustion and pollutant formation using Computational Fluid Dynamics (CFD) is an essential component in optimisation of internal combustion engines. Of particular interest is NOX-type pollutant formation in devices with high energy density, such as combustion chambers of jet engines. The objective of this study is to validate the performance of two types of NOX models for CFD and apply them to a simplified combustion chamber geometry of the Rolls-Royce Tay jet engine. Two approaches to NOX modelling shall be used: a simple 4-step combustion mechanism, followed by the extended Zeldovich NOX prediction model; and a detailed chemistry combustion model which includes the NOX species.

The candidate shall perform the following tasks within this project:

- Perform a literature survey of combustion and pollutant generation models capable of predicting NOX emissions using CFD;
- Describe in detail and implement the extended Zeldovich NOX creation model in OpenFOAM;
- Perform numerical simulations for the Sandia Flame D experimental flame using the 4-step combustion model by Jones and Lindstedt and the GRI-Mech-3.0 detailed chemistry model;
- Compare the results of the extended Zeldovich and detailed chemistry model against available experimental data, based on the 4-step and the detailed chemistry temperature fields;
- Identify the experimental data simplified combustion chamber geometry of the Rolls-Royce Tay jet engine. Perform numerical simulation of the flow, combustion and pollutant formation in the geometry to match experimental conditions with one of the NOX prediction approaches.
- Summarise the experiences on the performance of the reduced chemistry/Zeldovich and detailed chemistry NOX emissions prediction.

In all simulations use the Reynolds-averaged Navier-Stokes (RANS) turbulence models. If time and computational resources allow, attempt a Large Eddy Simulation (LES) of turbulent combustion for one of the cases and report on the experiences, accuracy and computational cost of RANS vs. LES simulations. The Thesis shall list the bibliography and any assistance received during this study.

Zadatak zadan:	Rok predaje rada:	Predviđeni datumi obrane:
17. siječnja 2019.	21. ožujka 2019.	27., 28. i 29 ožujka 2019.

Zadatak zadao: Predsjednik Povjerenstva:

Prof. dr. sc. Hrvoje Jasak Prof. dr. sc. Milan Vrdoljak

Contents

List of Figures

List of Tables

Nomenclature

Acronyms

AFR	Air/Fuel Ratio
CFD	Computational Fluid Dynamics
DNS	Direct Numerical Simulations
EBU	Eddy Break Up
EDC	Eddy Dissipation Concept
FVM	Finite Volume Method
ICAO	International Civil Aviation Organization
LES	Large Eddy Simulations
ODE	Ordinary Differential Equation
PaSR	Partially Stirred Reactor
RANS	Reynolds-Averaged Navier–Stokes
SIBS	Semi-Implicit Burlish-Stoer
UHC	Unburned Hydrocarbons

Dimensionless Numbers

Co	Courant number
Le	Lewis number
Ma	Mach number
Pr	Prandtl number
Sc	Schmidt number
RK	Runge Kutta

Greek Symbols

α	Thermal diffusivity	m^2/s

β	Temperature exponent	–
χ	Probability of ignition	–
Δt	Solver time step	s
Δh_f^0	Enthalpy of formation	$\mathrm{J/kg \cdot K}$
δ	Kronecker symbol	–
$\dot{\omega}$	Reaction rate	$\mathrm{kg/m^3 \cdot s}$
$\dot{\omega}_T$	Heat release due to combustion	$\mathrm{J/m^3 \cdot s}$
$\dot{\omega}_{k,arr}$	Laminar mass reaction rate	$\mathrm{kg/m^3 \cdot s}$
ε	Turbulent dissipation rate	$\mathrm{m^2/s^2}$
γ^*	Fine structures mass fraction	–
κ	PaSR reacting mixed fraction	–
λ	Heat transfer coefficient	$\mathrm{J/m^2 \cdot K}$
μ	Dynamic viscosity	$\mathrm{kg/(m \cdot s)}$
ν	Kinematic viscosity	$\mathrm{m^2/s}$
ν_k	Molar stoichiometric coefficient of species k	–
ρ	Density	$\mathrm{kg/m^3}$
σ_ε	k-ε model constant	–
σ_k	k-ε model constant	–
τ	Viscous tensor	–
τ_c	PaSR reacting mixed fraction	–
τ_c	Chemical time scale	s
τ_{mix}	Turbulent mixing time scale	s

Roman Symbols

$\dot{m}$	Mass transfer rate	$\mathrm{kg/s}$
$\dot{Q}$	Heat source/sink term	$\mathrm{W/m^3}$
$\mathcal{M}$	Species symbol	–
$\mathcal{R}$	Universal gas constant	$\mathrm{J/K \cdot mole}$
$\widetilde{\Theta}$	Reduced temperature	–
A	Preexponentaial coefficient	$(\mathrm{m^3/kmol})^{\mathrm{r}-1} \cdot \mathrm{s}^{-1}$ or $(\mathrm{cm^3/mol})^{\mathrm{r}-1} \cdot \mathrm{s}^{-1}$
a	Global reaction coefficient	–
$a_1 ... a_7$	JANAF coefficients	–

A_s	Sutherland's formula constant	–
b	Global reaction coefficient	–
C	Third body in chemical reaction	–
c_p	Heat capacity at constant pressure	$\mathrm{J/kg \cdot K}$
c_v	Heat capacity at constant pressure	$\mathrm{J/kg \cdot K}$
$C_{\varepsilon 1}$	k-ε model constant	–
$C_{\varepsilon 2}$	k-ε model constant	–
C_μ	k-ε model constant	–
C_{EBU}	EBU model constant	–
C_{mix}	PaSR model coefficient	–
D	Diffusion coefficient	$\mathrm{m^2/s}$
E	Activation energy	$\mathrm{cal/mol}$
f	Volume force	$\mathrm{N/m}$
h	Enthalpy	$\mathrm{J/kg}$
I	Turbulent intensity	–
K	Rate of reaction	$\mathrm{m^3/kmol \cdot s}$
k	Turbulent kinetic energy	$\mathrm{m^2/s^2}$
L	Length scale	m
M	Number of reactions	–
M_B	Third body	–
N	Number of species	–
p	Pressure	Pa
P_k	k-ε source term	$\mathrm{m^2/s^2}$
r	Global reaction coefficient sum	–
T	Activation temperature	K
t	Time	s
T_s	Sutherland's formula constant	–
u	Fluid velocity	$\mathrm{m/s}$
V	Diffusion velocity	$\mathrm{m/s}$
Y	Specie mass fraction	$\mathrm{kg/kg}$

Superscripts

*	Fine structure
$'$	Reactants
$''$	Products
$\bar{}$	Reynolds averaged
$\tilde{}$	Favre averaged

Subscripts

0	Reference value
eff	Effective
i	Cartesian coordinate component
min	Minimal
pr	Product
s	Sensible
t	Turbulent

Abstract

The objective of this thesis is to simulate the combustion process inside a jet engine combustion chamber using Computational Fluid Dynamics. The mathematical foundations and main issues of combustion modelling are presented. The partially stirred reactor (PaSR) combustion model, coupled with the k-ε turbulence model, is validated on the Sandia Flame D test case. The influence of three-dimensional effects and reaction mechanism complexity on flow characteristics is examined. The extended Zeldovich mechanism is used to calculate NO emissions, comparing results computed using reaction mechanisms of increasing complexity to experimental data. Numerical combustion simulations are performed on the Rolls Royce Tay geometry, for two flow configurations at take-off conditions. Simulation results are compared to available experimental data. The extended Zeldovich mechanism is used to model NOx emissions, which are compared to International Civil Aviation Organization emissions data.

Key words: *CFD*, *OpenFOAM*, *foam-extend*, *PaSR*, *reactingFoam*, *extended Zeldovich*, *Sandia Flame D*, *Rolls Royce Tay*.

Sažetak

U radu su opisane jednadžbe i aproksimacije koje se koriste u modeliranju procesa izgaranja. Za validaciju korištenog modela (*partially stirred reactor*), rezultati su uspoređeni s eksperimentalnim podacima mjerenim za Sandia Flame D plamen. Također je istražen utjecaj kemijskih reakcija na glavne karakteristike strujanja. Budući da su za simulacije korišteni reakcijski mehanizmi s različitim brojem kemijskih reakcija, u sklopu rada je implementiran prošireni Zeldovichev mehanizam za proračun koncentracije NO.

Validirani modeli korišteni su za simulaciju pojava u Rolls Royce Tay komori izgaranja pri različitim postavkama u uvjetima polijetanja, te su rezultati uspoređeni s eksperimentalnim podacima. Emisije NOx spojeva uspoređene su s dostupnim podacima Organizacije međunarodnog civilnog zrakoplovstva.

Ključne riječi: *CFD*, *OpenFOAM*, *foam-extend*, *PaSR*, *reactingFoam*, *extended Zeldovich*, *Sandia Flame D*, *Rolls Royce Tay*.

Prošireni sažetak

Projektiranje komore izgaranja zrakoplovnog mlaznog motora je veliki izazov. Tijekom izgaranja javljaju se pojave poput izrazito turbulentnog strujanja, miješanja goriva i zraka, oksidacije složenih ugljikovodika, i prijenosa topline. Provođenje eksperimentalnih mjerenja je skupo, te često sam postupak mjerenja utječe na tok strujanja. Nadalje, smanjenje emisija štetnih plinova u atmosferu postala je obveza svih proizvođača motora. Stoga, inženjeri koriste računalnu mehaniku fluida kako bi pomoću numeričkih simulacija dobili podatke koje mogu iskoristiti za poboljšanje performansi komore izgaranja.

Jedan od računalnih programa koji se koriste za numeričke simulacije je foam-extend [8], inačica OpenFOAM-a, u kojemu se koristi metoda kontrolnih volumena za diskretizaciju i iterativno rješavanje jednadžbi koje opisuju turbulentno izgaranje fluida.

Matematičko modeliranje turbulentnog izgaranja

Veličine u turbulentnom strujanju su stohastične prirode, što čini analitičko opisivanje turbulencije nemogućim. Jednadžbe se stoga rješavaju diskretizacijom vremenske i prostorne domene. Za egzaktno rješavanj, numerička mreža i vremenski korak trebali bi biti veoma mali, što bi zahtijevalo značajne računalne resurse. Stoga se koristi Raynoldsovo osrednjavanje, metoda u kojoj se jednadžbe vremenski uprosječuju. U strujanjima u kojima gustoća nije konstanta (stlačiva strujanja), koristi se Favreovo osrednjavanje.

Sustav jednadžbi kojima se opisuje turbulentno izgaranje je [9]:

- Zakon očuvanja mase:

$$\frac{\partial \overline{\rho}}{\partial t} + \frac{\partial \overline{\rho} \widetilde{u_i}}{\partial x_i} = 0,$$

- Zakon očuvanja količine tvari:

$$\frac{\partial \overline{\rho} \widetilde{Y_k}}{\partial t} + \frac{\partial}{\partial x_i}(\overline{\rho} \widetilde{u_i} \tilde{Y_k}) + \frac{\partial}{\partial x_i}(\overline{\rho}(\mu + \mu_t) \frac{\partial \widetilde{Y_k}}{\partial x_i} = \widetilde{\dot{\omega}_k},$$

- Zakon očuvanja količine gibanja:

$$\frac{\partial \overline{\rho}\widetilde{u_i}}{\partial t} + \frac{\partial}{\partial x_i}(\overline{\rho}\widetilde{u_i}\widetilde{u_j}) + \frac{\partial \overline{p}}{\partial x_j} = \frac{\partial}{\partial x_i}(\overline{\tau_{ij}} - \overline{\rho}\widetilde{u_i''u_j''}),$$

- Zakon očuvanja entalpije:

$$\frac{\partial \overline{\rho}\widetilde{h_s}}{\partial t} + \frac{\partial}{\partial x_i}(\overline{\rho}\widetilde{u_i}\widetilde{h_s}) + \frac{\partial}{\partial x_i}\left((\mu + \mu_t)\frac{\partial \widetilde{h_s}}{\partial x_i}\right) = \widetilde{\dot{\omega}_T}.$$

Kako bi se sustav jednadžbi mogao zatvoriti potrebno je uvesti dodatne relacije, poput jednadžbe idealnog plina i termodinamičke jednadžbe stanja. Također, Favreovim osrednjavanjem pojavljuju se dodatni izrazi koje je potrebno modelirati.

Kako bi se eliminirao Reynoldsov tenzor naprezanja, koristi se Boussinesqov koncept turbulentne viskoznosti. Turbulentna viskoznost računa se korištenjem k-ε modela turbulencije [10], kojim se uvode dvije dodatne transportne jednadžbe, jedna za turbulentnu energiju k, te druga za turbulentnu disipaciju ε. Ovaj model izabran je zbog poznatih performansi i jednostavne implementacije u sprezi s modelima kemijske kinetike.

Modeli kemijske kinetike služe za modeliranje brzine kemijskih reakcija. Brzinu kemijske reakcije moguće je izraziti korištenjem Arrheniusove jednadžbe:

$$K_{fj} = A_{fj} T^{\beta_j} \exp\left(-\frac{E_j}{RT}\right).$$

Koeficijenti A_{fj} i E_j ovise o pojedinačnoj kemijskoj reakciji, te se određuju eksperimentalno. Kemijski procesi, poput izgaranja metana, mogu se opisati pomoću različitog broja kemijskih reakcija, od nekolicine do stotina. Broj reakcija obično povećava preciznost simulacije, ali i računalni trošak. Turbulencija i izgaranje međusobno su povezani, te je njihovu interakciju potrebno modelirati. U ovome radu koristit će se model *partially stirred reactor* [11], u kojemu se pretpostavlja da brzina kemijske reacije ovisi o vremenskoj skali kemijskih reakcija i turbulentnog toka.

Matematičko modeliranje formiranja štetnih tvari

Postroživanjem zrakoplovnih regulativa vezanih uz emisije štetnih tvari, smanjivanje njihovih emisija postao je važan faktor kod projektiranja komora izgaranja. Uspoređivanjem emisijskih indeksa, vidljivo je da je potrebno posvetiti dodatnu pažnju smanjivanju emisija štetnih dušičnih spojeva, poput NO, N_2O i NO_2, pod ujedinjenim nazivom NOx. Ove su tvari štetne za okoliš, ali i za ljudsko zdravlje. Prošireni Zeldovichev mehanizam [12] temelji se na odvajanju formiranja NO od primarnog izgaranja, budući da male koncentracije NO spojeva ne utječu na svojstva primarnog toka. Stoga je koncentraciju NO moguće računati nakon završetka glavne simulacije. Prošireni Zeldovichev mehanizam povezuje nastajanje NO s temperaturom i koncentracijom molekula O, O_2, OH, NO i N_2. Reducirani reakcijski mehanizmi obično ne sadrže reakcije formiranja O i OH, te se ti spojevi također modeliraju, s pristupom djelomične ravnoteže.

Sandia Flame D validacijski slučaj

Sandia Flame D [4] je metanski plamen, često korišten za validaciju izgaranja zbog opširne dokumentacije i detaljnih eksperimentalnih podataka. Model *partially stirred reactor* spregnut je s k-ε modelom turbulencije, te su rezultati numeričkih simulacija uspoređeni s eksperimentalnim rezultatima. Oblik plamena vidljiv je na slici 1.

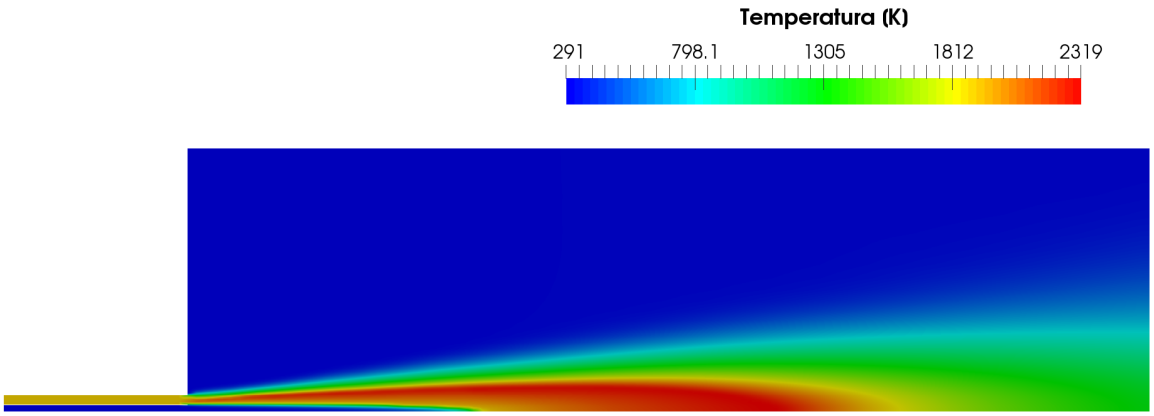

Slika 1: Oblik Sandia Flame D plamena

Numeričke simulacije provedene su koristeći dvodimenzionalnu i trodimenzionalnu numeričku mrežu, te su rezultati uspoređeni s eksperimentalnim podacima (slika 2). Numeričke simulacije

daju rezultate slične eksperimentu. Zaključeno je da trodimenzionalni efekti imaju mali utjecaj na rezultate, u slučaju osno-simetričnih rubnih uvjeta.

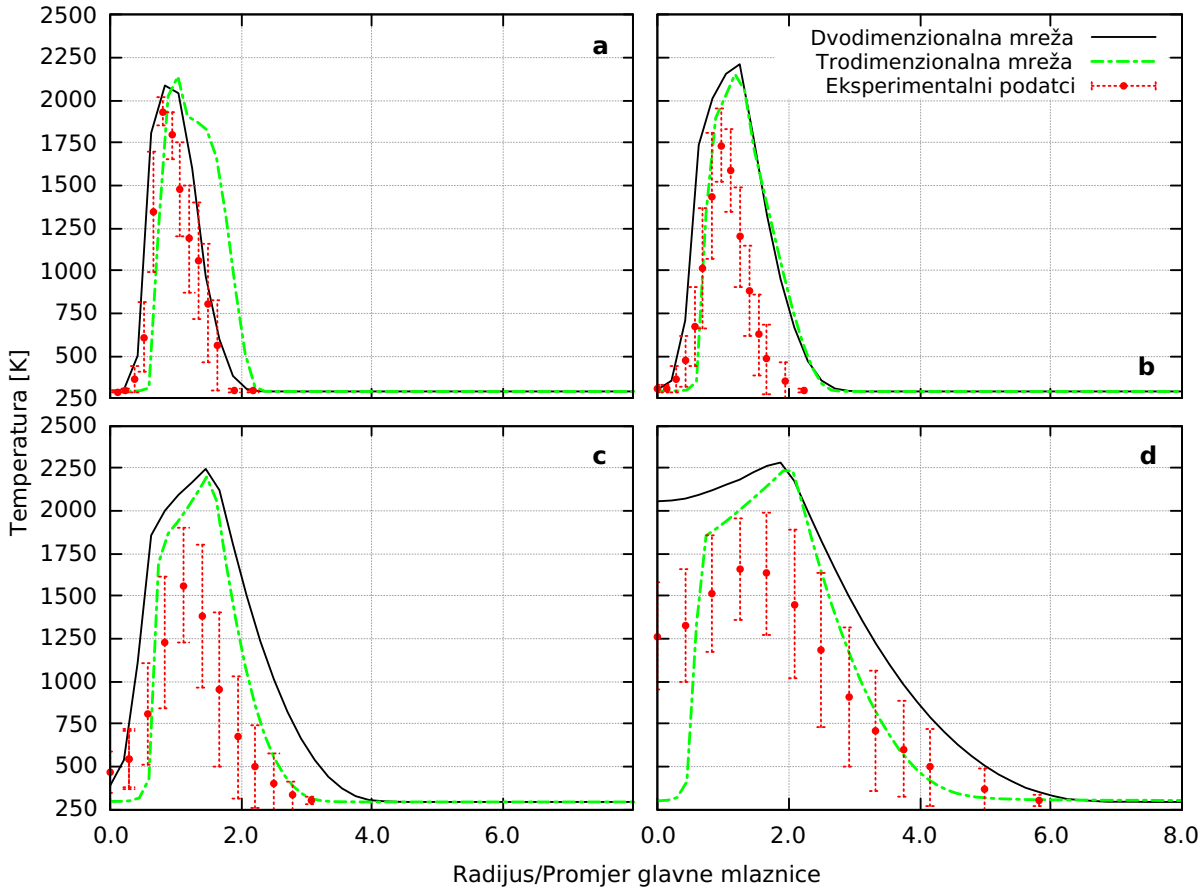

Slika 2: Temperatura na aksijalnim udaljenostima: a) x/d= 3, b) x/d= 7.5, c) x/d= 15, d) x/d= 30.

Utjecaj složenosti reakcijskog mehanizma na rezultate ispitan je koristeći mehanizam izgaranja metana s jednom, četiri i 325 reakcija. Svi reakcijski mehanizmi dobro se slažu s eksperimentalnim podacima (slika 3). Prošireni Zeldovichev mehanizam primijenjen je na rezultate s različitom složenošću reakcijskih mehanizama, te je koncentracija NO uspoređena s eksperimentalnim rezultatima (slika 4). Zaključeno je da je prošireni Zeldovichev mehanizam najbolje koristiti zajedno s reduciranim reakcijskim mehanizmima.

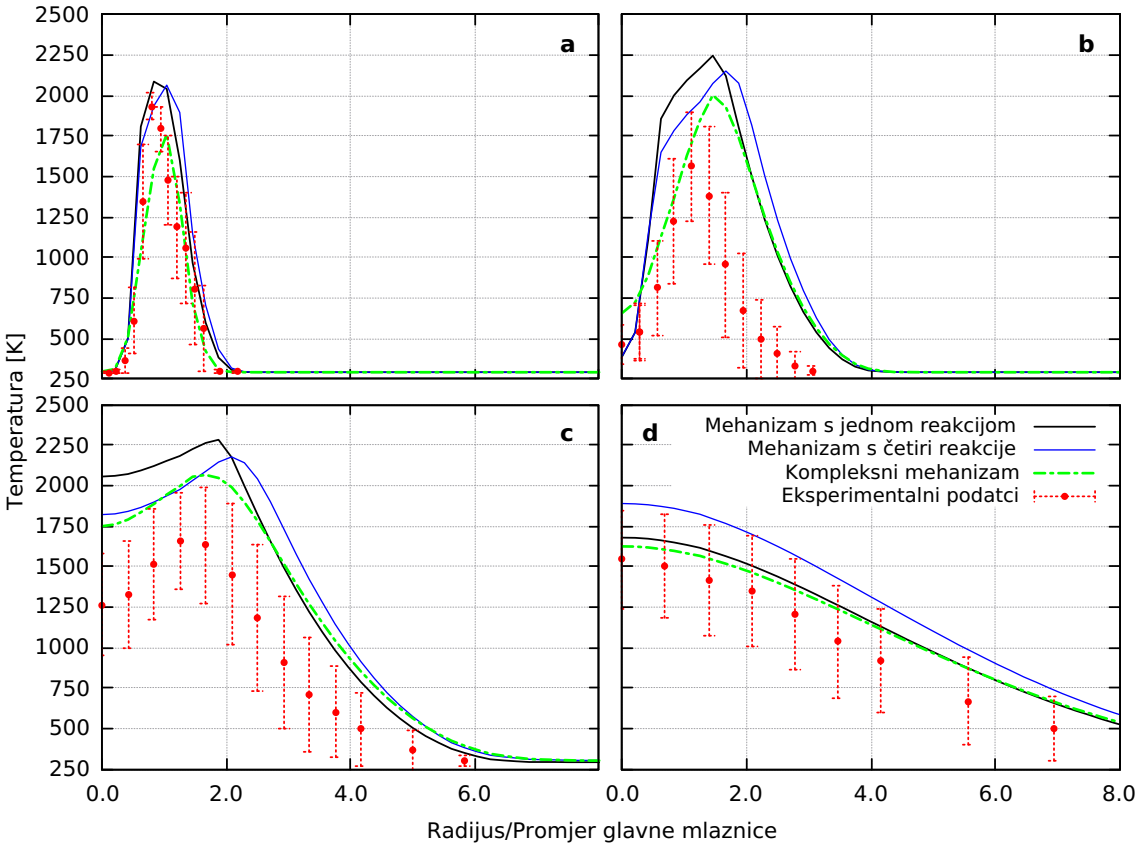

Slika 3: Temperatura na aksijalnim udaljenostima: a) x/d= 3, b) x/d= 15, c) x/d= 45, d) x/d= 60.

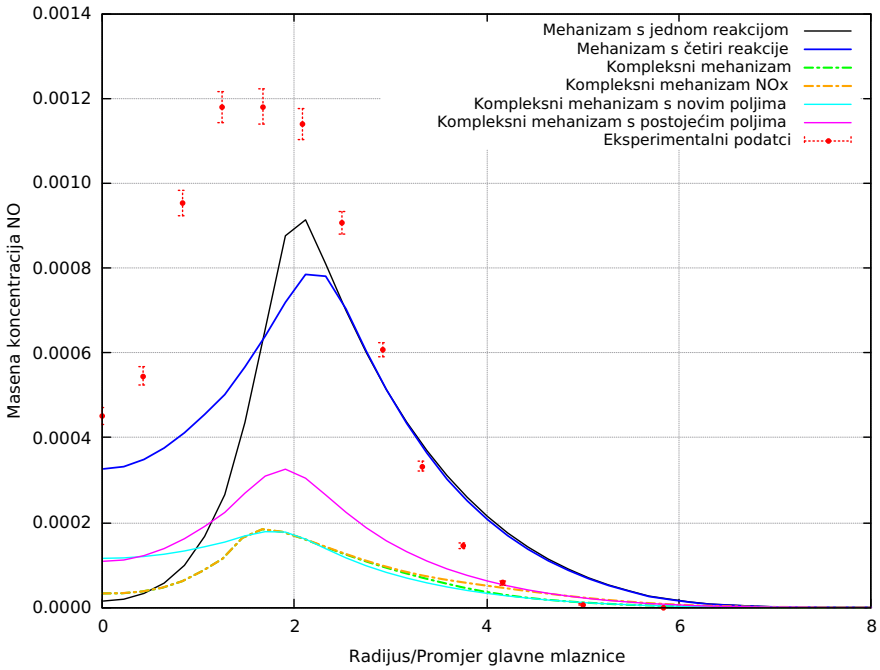

Slika 4: Maseni udio NO na aksijanoj udaljenosti x/d= 30.

Rolls Royce Tay komora za izgaranje

Komora izgaranja iz Rolls Royce Tay motora korištena je u ovom diplomskom radu zbog dostupnih eksperimentalnih rezultata [2]. Simulirane su dvije postavke strujanja, pri uvjetima polijetanja. Rezultati numeričkih simulacija se slažu s eksperimentalnim rezultatima. Na slici 5 vidljive su primarna i sekundarna recirkulacijska zona.

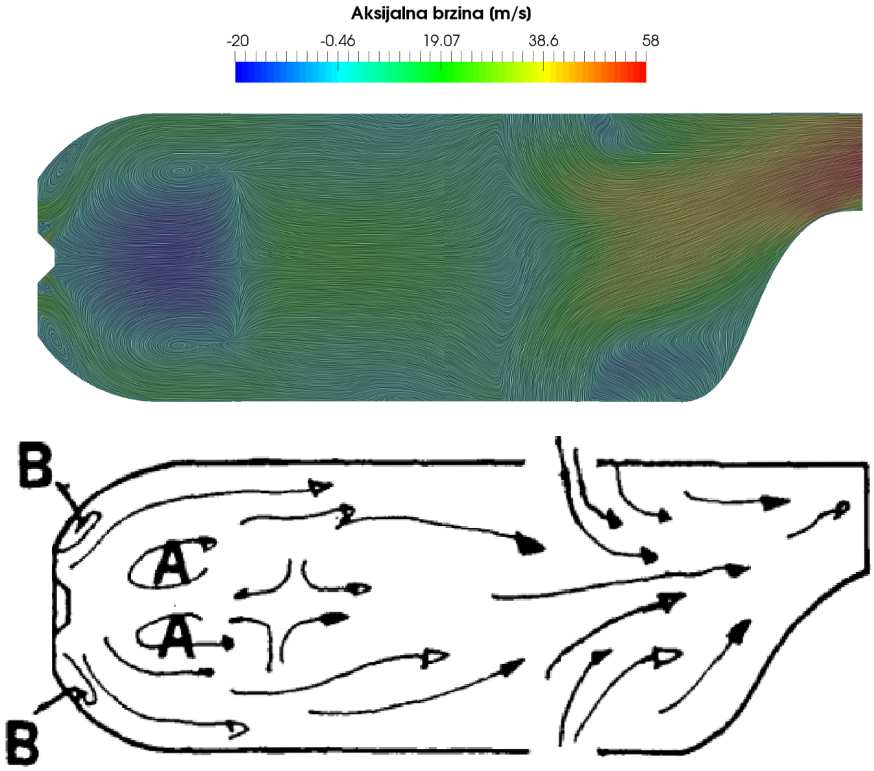

Slika 5: Usporedba strujanja i prikaz recirkulacijskih zona [1].

Slike 6 i 7 prikazuju usporedbu temperaturnih polja. Numeričkim simulacijama djelomično je prikazano strujanje unutar komore, no došlo je do otpuhivanja plamena na stijenku komore izgaranja. Najvjerojatniji uzrok ove pojave je pretpostavka nepropusne, umjesto porozne, stijenke komore izgaranja. Primjenom proširenog Zeldovichevog mehanizma izračunata je emisija NO od $66,90$ grama po kilogramu goriva. Stvarna emisija prema bazi podataka Organizacije međunarodnog civilnog zrakoplovstva [13] je $16,45 - 21,1$ grama po kilogramu goriva. Povećana emisija NO u simulacijama je vrlo vjerojatno posljedica povećane temperature i povećane fronte plamena u komori za izgaranje.

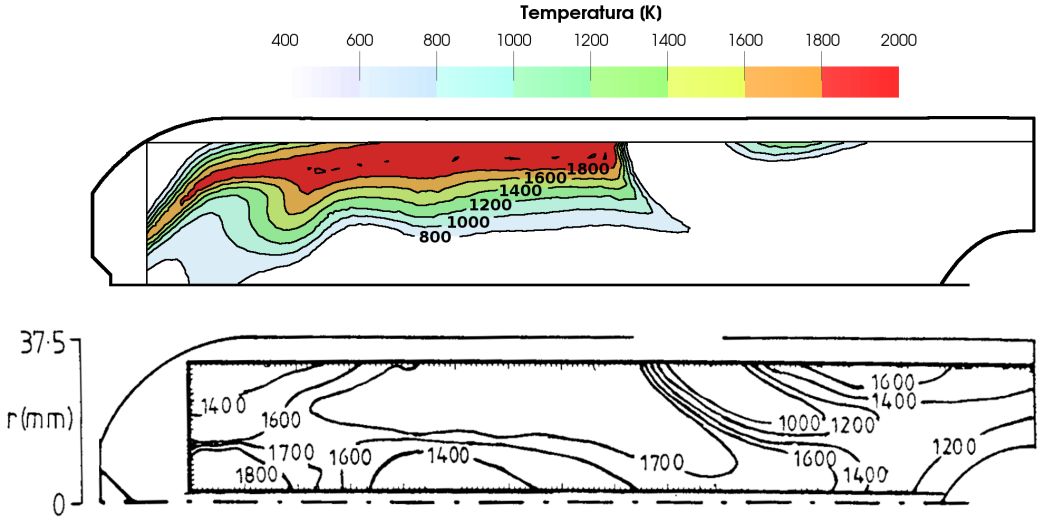

Slika 6: Usporedba temperaturnog polja s eksperimentalnim rezultatima - vertikalni presjek [2].

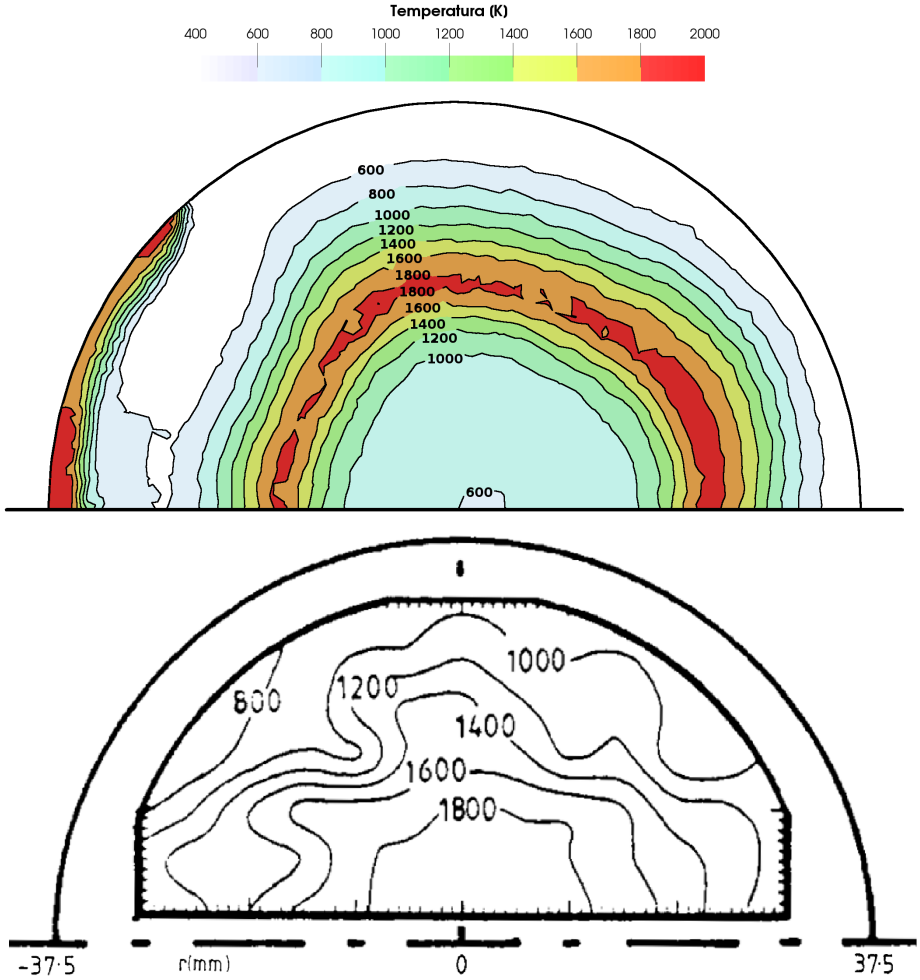

Slika 7: Usporedba temperaturnog polja s eksperimentalnim rezultatima - aksijalni presjek [2].

Zaključak

U ovom radu provedene su numeričke simulacije izgaranja pomoću programa foam-extend. Model *partially stirred reactor* je validiran koristeći Sandia Flame D, te je usporedbom numeričkih simulacija s eksperimentalnim rezultatima, zaključeno sljedeće:

- trodimenzionalni efekti imaju malen utjecaj na rezultate,
- pomoću reduciranih reakcijskhi mehanizma može se vjerodostojno opisati strujanje,
- preporuča se primjena proširenog Zeldovichevog mehanizma na reducirane reakcijske mehanizme.

Dva oblika strujanja ispitana su za Rolls Royce Tay komoru izgaranja pri uvjetima polijetanja. Zaključeno je da je numeričkim simulacijama moguće opisati glavne značajke strujanja, no dolazi do odvajanja plamena koji povećava temperaturu stijenke. Za budući rad, preporuča se implementacija konduktivnog i radijacijskog prijenosa topline, validacija reakcijskog mehanizma izgaranja propana, te implementacija porozne stijenke u komori izgaranja.

Chapter 1

Introduction

1.1 Jet Engine Combustion Chambers

The modern jet engine has perhaps been the most crucial element in the development of aviation in the mid to late 20^{th} century. Compared to a standard piston engine, the jet engine has increased thrust and reliability, with decreased fuel consumption. This has lead to a dramatic decrease in the production of aircraft equipped with piston engines, most of which are smaller sports aircraft. On the other hand, almost all larger aircraft use a variation of a jet engine: from turbojets used in military aircraft to high-bypass turbofans used on commercial aircraft to turboshafts used on helicopters. Introduction of jet engines to commercial aircraft has made air travel more affordable to general public.

At the heart of the jet engine, downstream from the compressor and upstream from the turbine, is the combustion chamber. In the combustion chamber, the chemical energy from the fuel is transformed into thermal and kinetic energy, propelling the aircraft. The purpose of a combustion chamber is to minimize the pressure drop and maximize heat release, all at a large scale and within small dimensions [14]. Therefore, the construction of the combustion chamber presents a challenge for engineers.

The most difficult obstacle to overcome is the heat release resulting from the combustion of the fuel (usually kerosene). Temperature of the gases released by combustion is about 2,000 to 2,300 K [14], far greater than what modern materials can withstand. This is solved by introduc-

ing additional air through the combustor walls, thus keeping the high-temperature combustion zone as far away from the walls as possible.

Another difficulty is the fuel dispersion and flame stabilization. In its liquid form, kerosene cannot be ignited and needs to be dispersed to achieve ignition. After the fuel is vaporized and ignited, the flame is stabilized in the recirculation zone and becomes the ignition source. The auto-ignition, along with the highly turbulent flow in the combustion chamber, are conditions where local flame extinction is possible.

With the introduction of new legislature, pollution emissions have become another limiting factor in the design of combustion chambers. Exhaust gases such as CO, CO_2, unburned hydrocarbons (UHC), SOx and NOx are being monitored, and new aircraft are required to comply with International Civil Aviation Organization (ICAO) emissions standards. The crucial element in reducing pollutant emissions is the design of the combustion chamber. Taking NOx emissions as an example, combustion chambers with a higher inlet swirl and a reduction of peak combustion temperature show reductions in NOx production.

To combat all the problems mentioned above, engineers use computational fluid dynamics to explore new ideas and optimize current designs.

1.2 Computational Fluid Dynamics of Combustion

Simulation of combustion using Computational Fluid Dynamics (CFD) can be divided into several key problems. The transient non-reacting flow structure inside the combustion chamber is highly turbulent in nature. Turbulence needs to be resolved over a wide range of length and time scales to be completely resolved. Therefore, several approaches are used to model turbulence:

- **Direct Numerical Simulations** (DNS) resolve all time and length scales of turbulence, without any modelling. This method provides the most accurate results; however, it is extremely computationally expensive and not yet applicable to practical engineering applications,
- **Large Eddy Simulations** (LES) use a filtering method to capture large scale flow structures, while the smaller eddies are modelled. This greatly reduces the computational

cost compared to DNS simulations. LES is able to describe the unsteadiness of flows and the behaviour of the largest eddies, but the subgrid stress model and the numerical discretization may introduce errors dependant on grid resolution,

- **Reynolds-Averaged Navier–Stokes** (RANS) simulations solve the ensemble averaged governing equations, modelling the turbulence on all scales. RANS is unable to describe unsteady phenomena and other complex flow elements but it is by far the least computationally expensive approach. Consequently, RANS simulations are used for many industrial applications.

Simulating even basic combustion cases with simple organic fuels, such as methane, required tens of species and hundreds of reactions [15]. Additionally, detailed reaction mechanisms are only available for a limited number of fuels. Chemical reactions present in combustion have different time scales, making their interaction with turbulence even more difficult to describe. Chemical reactions can be described using two approaches:

- **Fast chemistry models** assume that the time scale of chemical reactions is much smaller than the turbulence time scale. This approach assumes that the chemical reactions are limited by turbulent mixing.
- **Finite rate chemistry models** where the chemistry rates are calculated and compared to the turbulence time scale to determine if the chemical reaction speed or turbulence mixing are limiting factors.

Fuel and oxidizer can be introduced into the combustion chamber in several ways, determining the type of flame:

- **Premixed flames** where the fuel and oxidizer are mixed on a molecular level prior to ignition.
- **Diffusion flames** where the fuel and oxidizer enter the combustion chamber separately and are mixed as combustion occurs.

Combustion releases a large amount of heat, increasing the temperature and causing local expansion and changes in material properties of the gas. As a result, turbulence is increased, which promotes species mixing and increases combustion. The coupling between chemistry

and turbulence can be described using several models:

- **Statistical methods** use probability density functions and determine the reaction rate by integrating them,
- **Flamelet methods** assume the flame is composed of small surfaces that are treated as laminar flames. Species concentration is determined by solving the flamelet surface and looking up the distribution in a library of experimental data,
- **Eddy dissipation models** assume the cascade model, where energy is transported from larger to smaller eddies and combustion only occurs on the smallest scales.

1.3 Previous and Related Studies

Combustion CFD

Author	Name	Description	Cite
T Poinsot, D Veynante	Theoretical and Numerical Combustion	A great resource for a theoretical introduction of combustion and combustion CFD. Expansions to the derivations and equations used in this thesis can be found here.	[9]
Malalasekera, W Versteeg	An Introduction to Computational Fluid Dynamics: the Finite Volume Method	Presents the implementation of fluid dynamics in CFD. Combustion chapters contain the derivation of the PaSR model and extended Zeldovich mechanism.	[16]

Sandia Flame D

Author	Name	Description	Cite
R Barlow, J Frank	Piloted CH4/Air Flames C, D, E, and F-Release 2.1	Sandia Flame D experimental setup and data formats are explained.	[4]

Rolls-Royce Tay

Author	Name	Description	Cite
AF Bicen, DGN Tse, JH Whitelaw	The Influence of Air/Fuel Ratio and Swirl Number on the Combustion Characteristics of a Model Combustor	Experimental data from combustion experiments with the RR Tay geometry. Experimental data for temperature and species concentrations are provided.	[2]
DGN Tse	Flow and combustion characteristics of model annular and can-type combustors	Explains the methodology and exp. setup in a combusting case using the RR Tay geometry. Effects of air-to-fuel ratio, preheat and the influence of swirler vane angle are explored.	[17]
JJ Mcguirk, JMLM Palma	The flow inside a model gas turbine combustor: Calculations	Flow inside a RR Tay combustion chamber is computed using the k-ε turbulence model and compared to experimental data	[18]
JMLMD Palma	Mixing in non-reacting gas turbine combustor flows	Velocity experimental data using gathered using a water model. Different flow configurations are compared to experimental data to determine their influence	[1]
JJ McGuirk, JMLM Palma	The influence of numerical parameters in the calculation of gas turbine combustor flows	An overview of the influence of different boundary conditions and their influence on simulation results	[19]
P Koutmos	An isothermal study of gas turbine combustor flows	Experimental and theoretical investigation to determine the correct flow split and the influence of flow split and swirl geometry on results	[20]
H Nguyen, SJ Ying	Critical evaluation of Jet-A spray combustion using propane chemical kinetics in gas turbine combustion simulated by KIVA-II	Describes the two-equation propane reaction mechanism	[21]

1.4 Thesis Outline

The thesis begins with a brief overview of the governing equations of turbulent combustion. Assumptions and simplifications are introduced to reduce the equation set. After Favre averaging is completed, the resulting equations are presented and the terms that require modelling are listed. Modelling the Reynolds stresses is done using the k-ε turbulence model. The chemical reaction rate is modelled using the partially stirred reactor approach, based on the eddy break-up concept where combustion occurs in the turbulent fine structures.

The motivation behind pollutant modelling is given in Chapter 3, with an emphasis on NOx emissions. The production mechanisms for NOx are presented and it is concluded that the thermal NOx mechanism is responsible for the majority of NOx production. A mechanism that enables the prediction of NOx in post-processing, called the extended Zeldovich mechanism, is introduced. The potential modelling of additional chemical species is derived and the governing transport equation is presented.

A comprehensive overview of combustion modelling in OpenFOAM is given in Chapter 4. The structure of OpenFOAM is presented and numerical settings for simulating combustion are listed and explained. Additionally, the solution procedure is briefly presented.

Chapter 5 begins with the introduction of the Sandia Flame D, the test case used in this thesis for the validation of the partially stirred reactor model. The computational domain, boundary conditions, reaction mechanisms and simulation settings are explained. The impact of three-dimensional effects and reaction mechanisms on results is analysed. Several implementations of the Zeldovich mechanism are compared to experimental data to determine the most appropriate approach.

Numerical simulations of combustion in the Rolls-Royce Tay combustion chamber are presented in Chapter 6. Mesh generation, boundary conditions and simulation settings are detailed. Simulations were performed for two different flow configurations. The numerical results are compared to experimental data, and NOx emissions computed using the extended Zeldovich are compared to the ICAO emissions database. The work is completed with a summary of results.

1.5 Objectives

The objectives of this thesis are as follows:

- give a mathematical background of combustion modelling,
- describe the extended Zeldovich mechanisms and its implementation in CFD,
- describe the implementation of combustion models and reaction mechanisms in OpenFOAM,
- validate the partially stirred reactor model using the Sandia Flame D test case,
- implement the extended Zeldovich mechanism and validate it using the Sandia Flame D test case,
- simulate combustion in a realistic jet engine combustor and compare the results to experimental data,
- compare NOx emissions computed using the extended Zeldovich mechanism with ICAO emissions data.

Chapter 2

Combustion Modelling

In recent times, combustion modelling using computational fluid dynamics has become an irreplaceable tool in the engineering design process. Its ability to simulate complex processes instead of testing them experimentally has allowed engineers to significantly reduce the cost and time of research and development. Furthermore, fluid simulations allowed engineers to gain more insight into flows and processes that would be impossible to measure experimentally without affecting the process itself.

The fundamental understanding of turbulence has been a challenge for scientists for many years. Starting in the 15^{th} century, when Leonardo da Vinci coined the term turbulence (it. *turbolenza*) by saying: "... the smallest eddies are almost numberless, and large things are rotated only by large eddies and not by small ones, and small things are turned by small eddies and large". The work of Navier and Stokes in the early 19^{th} century is believed to fully mathematically describe the physics of turbulent flow but despite today's rapid advancements in CFD, turbulence has stayed one of the unresolved problems of classical physics.

Additionally, describing combustion in turbulent flow presents an ever larger issue because of the interaction between turbulent flow and the chemistry within it. As turbulence increases, it affects combustion, thus generating additional heat. The increase of temperature additionally increases turbulence through processes such as gas expansion and buoyancy. Coupling of turbulence and chemistry is the focus of current research in the science and engineering community.

In this chapter the governing equations of turbulent flow are presented, as well as the assump-

tions used to simplify the equations. Methods for solving the equations are discussed, and the derivation of Favre averaged equations is shown. Finally, the terms that require modelling are highlighted, with the modelling approaches presented and selected.

2.1 Governing Equations for Turbulent Combustion

In this section the governing equations for turbulent combustion are derived. To describe turbulent flow, the conservation of mass and conservation of momentum are required. In case of a non-adiabatic flow, conservation of energy also needs to be accounted for. If chemical reactions are present (in this case combustion), an equation for the conservation of species is needed. Assumptions used to simplify the governing equations and additional expressions needed to close the equation set are shown. The governing equations are:

Conservation of mass

The mass conservation equation is the same for reacting and non-reacting flows since combustion does not generate mass:

$$\frac{\partial \rho}{\partial t} + \frac{\partial (\rho u_i)}{\partial x_i} = 0, \qquad \text{for } i = 1,2,3 \tag{2.1.1}$$

where ρ is the density, u_i is the velocity component and t is time. At low velocities (Ma $<$ 0.3) the compressibility effects can be neglected and density can be assumed to be constant. However, combustion causes significant changes of temperature which consequently causes changes of density.

Conservation of species

The mass conservation equation of species is:

$$\frac{\partial (\rho Y_k)}{\partial t} + \frac{\partial}{\partial x_i}(\rho (u_i + V_{k,i}) Y_k) = \dot{\omega}_k, \qquad \text{for } k = 1,N \tag{2.1.2}$$

where Y_k is the mass fraction, $V_{k,i}$ is the i-th component of the diffusion velocity V_k of specie k and $\dot{\omega}_k$ is the reaction rate of specie k. In order to avoid the computationally expensive calculation of diffusion velocities, Fick's law [22] is often used in CFD codes to simplify the diffusion velocity:

$$V_{k,i}Y_k = -D_k \frac{\partial Y_k}{\partial x_i}, \tag{2.1.3}$$

where D_k is the diffusion coefficient of species k. A common practice is to assume the same diffusion D coefficient for all species [9].

Conservation of momentum

The conservation of momentum equation can be expressed as:

$$\frac{\partial}{\partial t}(\rho u_i) + \frac{\partial}{\partial x_i}(\rho u_i u_j) = -\frac{\partial p}{\partial x_i} + \frac{\partial \tau_{ij}}{\partial x_i} + \rho \sum_{k=1}^{N} Y_k f_{k,j}, \tag{2.1.4}$$

where p is the static pressure, $f_{k,j}$ is the volume force acting on species k in direction j and $\tau_{i,j}$ is the viscous tensor defined as:

$$\tau_{i,j} = -\frac{2}{3}\mu \frac{\partial u_k}{\partial x_k}\delta_{ij} + \mu\left(\frac{\partial u_i}{\partial x_j} + \frac{\partial u_j}{\partial x_i}\right) \tag{2.1.5}$$

where μ is the dynamic viscosity and δ_{ij} is the Kronecker symbol. In combustion codes, the dynamic viscosity is often calculated using Sutherland's formula [23]:

$$\mu = A_s \frac{\sqrt{T}}{1 + \frac{T}{T_s}} \tag{2.1.6}$$

where the constants are $A_s = 1.67212 \cdot 10^{-6}\, 1/s$ and $T_s = 170.672\, K$. In most flames, volume forces $f_{k,j}$ (such as gravity) are negligible and assumed to be zero.

Conservation of energy

The conversation of energy equation can be written using the energy form (sensible, chemical, total or total non-chemical) or enthalpy form (sensible, chemical, total or total non-chemical).

Enthalpy is defined as:

$$h = \sum_{k=1}^{N} \left(\int_{T_0}^{T} \underbrace{c_{pk} dT}_{\text{sensible}} + \underbrace{\Delta h^0_{f,k}}_{\text{chemical}} \right), \tag{2.1.7}$$

where h is the enthalpy, c_{pk} is the heat capacity at constant pressure of species k and $\Delta h^0_{f,k}$ is the enthalpy of formation of species k at temperature T_0. A formulation using the sensible enthalpy does not have chemical terms or the heat flux q, and as such is preferred in CFD codes [9]. The conservation of sensible enthalpy equation is:

$$\rho \frac{Dh_s}{Dt} = \frac{Dp}{Dt} + \frac{\partial}{\partial x_i}\left(\lambda \frac{\partial T}{\partial x_i}\right) - \frac{\partial}{\partial x_i}\left(\mu \left(\frac{1}{Sc_k} - \frac{1}{\mathrm{Pr}_k}\right) \sum_{k=1}^{N} h_{s,k} Y_k V_{k,i}\right) + \frac{\partial u_i}{\partial x_j}\tau_{ij} + \dot{\omega}_T + \dot{Q} + \rho Y_k f_{k,i} V_{k,i}, \tag{2.1.8}$$

where h_s is the sensible enthalpy, $\frac{Dp}{Dt}$ is the pressure work term, $\dot{\omega}_T$ is the heat release due to combustion, λ is the heat diffusion coefficient, $h_{s,k}$ is the sensible enthalpy of species k and $\dot{Q}$ is the heat source/sink term.

Before proceeding further, we shall define the non dimensional numbers:

- The Schmidt number Sc is the ratio between the rate of momentum transport and mass transport, defined as:

$$Sc = \frac{\lambda}{\rho D_k}. \tag{2.1.9}$$

- The Prandtl number Pr is the ratio between the rate of momentum and the rate of energy transport, defined as:

$$Pr = \frac{c_p \mu}{\lambda}. \tag{2.1.10}$$

- The Lewis number Le compares diffusion speeds of heat and species:

$$Le = \frac{\lambda}{\rho c_p D_k} = \frac{Sc}{Pr}. \tag{2.1.11}$$

In many CFD codes, Lewis number is set to unity because it was observed that it is mostly constant in the domain and shows a small variation at the flame front [9]. Prandtl number is usually set between 0.7 and 1, and will also be set to unity in this thesis. By assuming the Lewis and Prandtl number are equal to one and assuming a single diffusion coefficient D, Equation (2.1.8) simplifies to:

$$\rho\frac{Dh_s}{Dt} = \frac{Dp}{Dt} + \frac{\partial}{\partial x_i}\left(\lambda\frac{\partial T}{\partial x_i}\right) + \frac{\partial u_i}{\partial x_j}\tau_{ij} + \dot{\omega}_T + \dot{Q} + \rho Y_k f_{k,i} V_{k,i}. \tag{2.1.12}$$

In order to simplify the transport equation, the following assumptions are made:

- The viscous heating source term $\tau_{ij}\frac{\partial u_i}{\partial x_j}$ is negligible in comparison to the heat release by combustion and is neglected [9],
- The transport of sensible enthalpies by the species diffusion velocities is neglected [24],
- Heat fluxes are expressed using the sensible enthalpy:

$$-\lambda\frac{\partial T}{\partial x_i} \approx -\frac{\lambda}{C_p}\frac{\partial h_s}{\partial x_i} = -\alpha\frac{\partial h_s}{\partial x_i}, \tag{2.1.13}$$

  where α is the thermal diffusivity,
- Volume forces $f_{k,j}$ are neglected,
- Heat sources (e.g. electrical sparks) or heat sinks (e.g. heat radiation) are neglected.

Thermal conductivity α is derived using the modified Eucken relation [25]:

$$\alpha = \frac{\lambda}{c_p} = \mu\frac{c_p}{c_p}(1.32 + 1.77\frac{\mathcal{R}}{c_v}), \tag{2.1.14}$$

where $\mathcal{R}$ is the universal gas constant ($R = 8.314$ J K^{-1} mole^{-1}), c_v and c_p are respectively the mass heat capacity at constant specific volume and the mass heat capacity at constant pressure. Finally, the simplified transport equation is:

$$\frac{\partial \rho h_s}{\partial t} + \frac{\partial \rho u_i h_s}{\partial x_i} = \frac{Dp}{Dt} + \frac{\partial}{\partial x_i}\left(\alpha\frac{\partial h_s}{\partial x_i}\right) + \dot{\omega}_T, \tag{2.1.15}$$

Thermodynamic Equations of State

The system of transport equations shown above has $5+n$ unknown variables: ρ, u_i, Y_k, p, h_s and T; where n is the number of specie conservation equations, as required by the combustion model. Since there are only $3+n$ transport equations defined above, additional equations are needed to close the system.

Using the ideal gas law, density ρ can be calculated as:

$$\rho = \frac{p\sum_{k=1}^{N} Y_k M_k}{\mathcal{R}T}. \tag{2.1.16}$$

The thermodynamic equation of state is used to establish the relation between the sensible enthalpy h_s and temperature T:

$$h_s = \int_{T_0}^{T} c_p dT. \tag{2.1.17}$$

Heat capacity c_p depends on temperature and it is calculated using polynomial approximations based on the JANAF thermochemical tables [26] for a high and low temperature range:

$$c_p(T) = \mathcal{R}\left(a_1 + a_2T + a_3T^2 + a_4T^3 + a_5T^4\right) \tag{2.1.18}$$

Sensible enthalpy is calculated as:

$$h_s(T) = h(T) - h(T_0), \tag{2.1.19}$$

where the total enthalpy h is calculated using JANAF tables [26]:

$$h(T) = \mathcal{R}\left(a_1T + a_2T^2 + a_3T^3 + a_4T^4 + a_5T^5 + a_6\right). \tag{2.1.20}$$

With these additional transport equations, the system is closed and can be solved iteratively.

2.2 Favre Averaged Equations for Turbulent Combustion

In the previous section governing equations describing turbulent combustion were presented. To fully resolve the instantaneous equations, they need to be solved for all time and length scales, which is impractical for high Reynolds flows. For most engineering design purposes, integral values such as mass flow, mean temperature or pressure are needed. Reynolds averaged equations can be written by decomposing any quantity f into a mean (time-averaged) $\overline{f}$ and fluctuating f' component:

$$f(x,t) = \overline{f}(x) + f'(x,t), \qquad \overline{f}(x) = \lim_{T\to\infty} \frac{1}{T} \int_0^T f(x,t)dt, \tag{2.2.1}$$

However, Reynolds averaging for compressible flows introduces many unclosed correlations between the quantity f and its density fluctuation $\overline{\rho' f'}$. An alternative to Reynolds averaging are mass-weighted averages called Favre averages. Similarly to Reynolds averaging, any quantity f can be split into a mean (time-averaged) component $\widetilde{f}$ and a fluctuating component f'' where the Favre averaged mean component is:

$$\tilde{f} = \frac{\overline{\rho f}}{\overline{\rho}}. \tag{2.2.2}$$

After applying Favre averaging to the instantaneous conservation equations in the previous section, a set of Favre averaged equations for combusting flows can be assembled.

Favre averaged conservation of mass:

$$\frac{\partial \overline{\rho}}{\partial t} + \frac{\partial \overline{\rho}\widetilde{u_i}}{\partial x_i} = 0 \tag{2.2.3}$$

Favre averaged conservation of species:

$$\frac{\partial \overline{\rho}\widetilde{Y_k}}{\partial t} + \frac{\partial}{\partial x_i}(\overline{\rho}\widetilde{u_i}\tilde{Y_k}) = \frac{\partial}{\partial x_i}(\overline{\rho}D_k \frac{\partial \widetilde{Y_k}}{\partial x_i} + \overline{\rho}\widetilde{u_i'' Y_k''}) + \widetilde{\dot{\omega}_k} \qquad \text{for k=1,N} \tag{2.2.4}$$

Equation (2.2.4) contains terms that need to be modelled in order to close the set of equations:

- Turbulent species flux $\widetilde{u_i''Y_k''}$ is closed using the classical gradient assumption [9]:

$$\overline{\rho}\widetilde{u_i''Y_k''} = -\frac{\mu_t}{Sc_{kt}}\frac{\partial \widetilde{Y}_k}{\partial x_i} \tag{2.2.5}$$

  where μ_t is the turbulent viscosity and Sc_{kt} is the turbulent Schmidt number for species k. Since the turbulent Prandtl number and Lewis number were set to unity, the turbulent Schmidt number is therefore also equal to one,

- Favre averaged chemical reaction rate $\widetilde{\dot{\omega}_k}$ is one of the main obstacles in combustion modelling. Different approaches used to model the chemical reaction rate will be further examined in Section 2.4.

Favre averaged conservation of momentum:

$$\frac{\partial \overline{\rho}\widetilde{u}_i}{\partial t} + \frac{\partial}{\partial x_i}(\overline{\rho}\widetilde{u}_i\widetilde{u}_j) + \frac{\partial \overline{p}}{\partial x_j} = \frac{\partial}{\partial x_i}(\overline{\tau_{ij}} - \overline{\rho}\widetilde{u_i''u_j''}) \tag{2.2.6}$$

The only term that requires modelling are the Reynolds stresses $\widetilde{u_i''u_j''}$. This is done by the turbulence model as described in Section 2.3.

Favre averaged conservation of enthalpy:

$$\frac{\partial \overline{\rho}\widetilde{h}_s}{\partial t} + \frac{\partial}{\partial x_i}(\overline{\rho}\widetilde{u}_i\widetilde{h}_s) = \frac{\partial}{\partial x_i}\left(\alpha\frac{\partial \widetilde{h}_s}{\partial x_i} - \overline{\rho u_i'' h_s''}\right) + \widetilde{\omega_T} \tag{2.2.7}$$

The following terms need to be modelled:

- Turbulent enthalpy flux $\widetilde{u_i''h_s''}$ is closed using the classical gradient assumption:

$$\overline{\rho}\widetilde{u_i''h_s''} = -\frac{\mu_t}{Pr_{kt}}\frac{\partial \widetilde{h}_s}{\partial x_i}, \tag{2.2.8}$$

  where Pr_{kt} is the turbulent Prandtl number for species k. The turbulent Prandtl number is set to unity.

- Heat release due to combustion $\widetilde{\dot{\omega}_T}$ is expressed as:

$$\widetilde{\dot{\omega}_T} = \sum_{k=1}^{N} \Delta h^0_{f,k} \widetilde{\dot{\omega}_k}, \tag{2.2.9}$$

where the enthalpy of formation $\Delta h^0_{f,k}$ is calculated using JANAF coefficients [26].

2.2.1 Favre averaged set of equations

After Favre averaging, simplifying and applying assumptions to the governing equations, the final set of Favre averaged equations is derived:

Conservation of mass:

$$\boxed{\frac{\partial \overline{\rho}}{\partial t} + \frac{\partial \overline{\rho}\widetilde{u_i}}{\partial x_i} = 0} \tag{2.2.10}$$

Conservation of species:

$$\boxed{\frac{\partial \overline{\rho}\widetilde{Y_k}}{\partial t} + \frac{\partial}{\partial x_i}(\overline{\rho}\widetilde{u_i}\widetilde{Y_k}) + \frac{\partial}{\partial x_i}(\overline{\rho}(\mu + \mu_t)\frac{\partial \widetilde{Y_k}}{\partial x_i} = \widetilde{\dot{\omega}_k}} \tag{2.2.11}$$

Conservation of momentum:

$$\boxed{\frac{\partial \overline{\rho}\widetilde{u_i}}{\partial t} + \frac{\partial}{\partial x_i}(\overline{\rho}\widetilde{u_i}\widetilde{u_j}) + \frac{\partial \overline{p}}{\partial x_j} = \frac{\partial}{\partial x_i}(\overline{\tau_{ij}} - \overline{\rho}\widetilde{u_i'' u_j''})} \tag{2.2.12}$$

Conservation of enthalpy:

$$\boxed{\frac{\partial \overline{\rho}\widetilde{h_s}}{\partial t} + \frac{\partial}{\partial x_i}(\overline{\rho}\widetilde{u_i}\widetilde{h_s}) + \frac{\partial}{\partial x_i}\left((\mu + \mu_t)\frac{\partial \widetilde{h_s}}{\partial x_i}\right) = \widetilde{\dot{\omega}_T}} \tag{2.2.13}$$

2.3 Modelling the Reynolds stresses

Reynolds stresses $\widetilde{u_i'' u_j''}$ in the Favre averaged conservation of momentum equation (Equation (2.2.12)) are the result of averaging and can not be solved directly. They are modelled using a turbulence model. Most turbulence models are based on the Boussinesq assumption:

$$\overline{\rho}\widetilde{u_i'' u_j''} = -\mu_t \left(\frac{\partial \widetilde{u}_i}{\partial x_j} + \frac{\partial \widetilde{u}_j}{\partial x_i} - \frac{2}{3}\delta_{ij}\frac{\partial \widetilde{u}_k}{\partial x_k} \right) + \frac{2}{3}\overline{\rho}k, \tag{2.3.1}$$

where the turbulent kinetic energy k is:

$$k = \frac{1}{2}\sum_{k=1}^{3} \widetilde{u_k'' u_k''}. \tag{2.3.2}$$

The Boussinesq assumption is a useful simplification to reduce the number of unknowns in the Reynolds stress tensor from six to only one: the turbulent viscosity μ_t. This is done by assuming that the anisotropy of turbulence is identical to the anisotropy of the symmetric velocity gradient, which is not valid in flows with a high strain rate. However, for simple geometries with high turbulence the Boussinesq assumption is generally valid [27]. Using dimensional analysis it can be seen that correctly calculating the turbulent viscosity requires at least two scales of flow: a velocity scale and a length or time scale.
Three main approaches of determining the scales have been proposed:

- **Zero equation models** such as the Prandtl mixing length model do not have any additional transport equations to properly determine the length scales. Instead, the scales need to be determined empirically from local equilibrium assumptions. The Prandtl mixing length model was one of the first turbulence models developed, but the need to determine the mixing length on a case by case basis has proved impractical for commercial use.

- **One equation models** such as the Prandtl-Kolmogorov model use a transport equation to determine the velocity scale, most commonly in the form of the turbulent kinetic energy k. Once again, the length scale is determined as a characteristic length of the flow. One equation models provide a transport equation which gives them more flexibility for different flow configurations but they suffer the same drawback as zero equation models.

- **Two equation models** such as the $k-\varepsilon$ model have two additional transport equations, one for the velocity scale in the form of the kinetic energy k, and, in the case of the $k-\varepsilon$ model, another one for the time scale in the form of the dissipation rate ε.

For this thesis, the $k-\varepsilon$ model [28] will be used. The motivation behind this choice, as well as the description of the model are given in the following section.

2.3.1 The k-ε Turbulence Model

Two equation models are the simplest closed models, meaning they can predict the properties of a turbulent flow without any prior knowledge of the turbulent structure [27]. This is possible because of two additional transport equations that give the appropriate velocity and length/time scales. The most commonly used two equation model is the k-ε model. Since the publishing of the central paper by Jones and Launder [10] in 1972, it has been used in many scientific and industrial turbulent flows. As such, it is well documented and its advantages and disadvantages are known. Its main advantages are its ease of use, low computational cost and its documented application in a number of different flows.

Algebraic laws are used to treat the flow around walls since the flow around the wall is not the main interest and has little effect on the main area of combustion. The model was chosen because of its well documented properties and its simple integration with the partially stirred reactor model used to model the chemical reaction rate (Section 2.4.3). The additional transport equations for turbulent kinetic energy k and turbulent dissipation rate ε are:

$$\frac{\partial}{\partial t}(\overline{\rho}\widetilde{k}) + \frac{\partial}{\partial x_i}(\overline{\rho}\widetilde{u_i}\widetilde{k}) \left[\left(\mu + \frac{\mu_t}{\sigma_k} \right) \frac{\partial k}{\partial x_i} \right] + P_k - \overline{\rho}\widetilde{\varepsilon}, \tag{2.3.3}$$

$$\frac{\partial}{\partial t}(\overline{\rho}\widetilde{\varepsilon}) + \frac{\partial}{\partial x_i}(\overline{\rho}\widetilde{u_i}\widetilde{\varepsilon}) \left[\left(\mu + \frac{\mu_t}{\sigma_\varepsilon} \right) \frac{\partial \widetilde{\varepsilon}}{\partial x_i} \right] + C_{\varepsilon 1} \frac{\widetilde{\varepsilon}}{\widetilde{k}} P_k - C_{\varepsilon 2} \overline{\rho} \frac{\widetilde{\varepsilon}^2}{\widetilde{k}}, \tag{2.3.4}$$

where P_k is the source term calculated as:

$$P_k = -\overline{\rho u_i'' u_j''} \frac{\partial u_i}{\partial x_j}. \tag{2.3.5}$$

and the Reynolds stresses are calculated using the Boussinesq Equation (2.3.1). Turbulent viscosity μ_t is expressed as:

$$\mu_t = \overline{\rho} C_\mu \frac{\widetilde{k}^2}{\widetilde{\varepsilon}} \tag{2.3.6}$$

Model constants are set to:

$$C_\mu = 0.09; \quad \sigma_k = 1.0; \quad \sigma_\varepsilon = 1.0; \quad C_{\varepsilon 1} = 1.44; \quad C_{\varepsilon 2} = 1.92; \tag{2.3.7}$$

2.4 Modelling the Chemical Reaction Rate

Modelling the chemical reaction rate is one of the main difficulties in reacting flows and, even more so, in combusting flows. To properly define the reaction rate in a turbulent combusting flow, first the reaction rate of a laminar flame will be explained. A chemical system of N species reacting through M reactions can be written as:

$$\sum_{k=1}^{N} \nu'_{kj} \mathcal{M}_k \rightleftharpoons \sum_{k=1}^{N} \nu''_{kj} \mathcal{M}_k, \qquad \text{for} j = 1, M, \tag{2.4.1}$$

where $\mathcal{M}_k$ is the symbol for species k, ν'_{kj} and ν''_{kj} are molar stoichiometric coefficients of species k in reaction j. The laminar mass reaction rate $\dot{\omega}_{k,arr}$ is the sum of individual rates $\dot{\omega}_{kj,arr}$ for all reactions M:

$$\dot{\omega}_{k,arr} = \sum_{j=1}^{M} \dot{\omega}_{kj,arr} = W_k \sum_{j=1}^{M} \nu_{kj} Q_j, \tag{2.4.2}$$

where Q_j is the rate of progress of reaction j:

$$Q_j = \frac{\dot{\omega}_{kj,arr}}{M_k \nu_{kj}}, \tag{2.4.3}$$

and M_k is the atomic weight of species k and ν_{kj}, defined as:

$$\nu_{kj} = \nu''_{kj} - \nu'_{kj}. \tag{2.4.4}$$

Additionally, Q_j can be expressed as:

$$Q_j = K_{fj}\Pi_{k=1}^{N}\left(\frac{\rho Y_k}{W_k}\right)^{\nu'_{kj}} - K_{rj}\Pi_{k=1}^{N}\left(\frac{\rho Y_k}{W_k}\right)^{\nu''_{kj}}, \tag{2.4.5}$$

where K_{fj} and K_{rj} are the forward rate of reaction j and reverse rate of reaction j, respectively. The expression in the brackets represents the molar concentration of species k. Reaction rates are independent of concentration and are usually modelled using the empirical Arrhenius equation [29]:

$$K_{fj} = A_{fj}T^{\beta_j}\exp\left(-\frac{E_j}{RT}\right). \tag{2.4.6}$$

Three new terms are introduced: the preexponential constant A_{fj}, the temperature exponent β_j and the activation energy E_j. To clarify the Arrhenius law, the expression can be split into two terms: the preexponential factor and the exponential term. The preexponential constant A_{fj} includes factors like the frequency of collisions and their orientation. In order to model the change of A_{fj} with temperature, the temperature exponent β_j is added.

The exponential term contains the activation energy E_j which is the minimum energy required for the reaction to start. Equivalently, the activation energy can be expressed using the activation temperature $E_j/R = T_{aj}$. The exponential term can be understood as the fraction of the molecules present in the gas which have the energy equal to, or in excess of, the activation energy at a particular temperature.

Reaction rates are often written in the CHEMKIN format [30] using the preexponential constant A_{fj}, the temperature exponent β_j and the activation energy E_j. More information about the CHEMKIN format and its implementation can be found in Section 4.1.3.

With the reaction rates calculated from empirical data, a set of ordinary differential equations (ODEs) is assembled. The set of ODEs is characterised by its stiffness, meaning small step sizes and stiff ODE solvers are required to obtain results. Because of this, calculation of chemical reaction rate is often the most computationally expensive part of a CFD combustion simulation, especially in reactions involving a large number of species [31]. This presents another major challenge for researches, because finding a chemical scheme simple enough not to be computationally expensive but also complex enough to properly describe the chemical process is not always apparent.

With the temperature being in the exponent of the reaction rate expression, the term is highly non-linear. The mean reaction rate $\widetilde{\dot{\omega}_k}$ can not be easily expressed using the Arrhenius law. One option is to obtain the mean reaction rate using a Taylor expansion for the exponential term. However, this introduces numerous terms that would need to be modelled [16]. For this reason, a new approach is needed to properly model the mean reaction rate $\widetilde{\dot{\omega}_k}$.

As stated in the Chapter 1, flames can be classified as premixed flames (where there is sufficient time for the fuel and air to completely mix before combustion) or diffusion flames (where the mixing of the reactants is done at the same time as the combustion). The focus of this thesis will be diffusion flames as they are the main combustion mechanism in jet engine combustion chambers.

2.4.1 Eddy Break Up (EBU) Model

The eddy breakup model is based on the assumption that the reaction rate is controlled by turbulent motions (and not explicitly by chemistry). Proposed by Spalding [32], it is one of the most commonly used models in commercial codes and generally gives better results than the simple Arrhenius model [9]. A single step global infinitely fast chemical reaction is assumed. By avoiding the computationally expensive Arrhenius chemical kinetics, the EBU model can be significantly faster in reactions with a high number of species.

The mean reaction rate can be calculated using the following equation:

$$\widetilde{\dot{\omega}_k} = C_{EBU}\overline{\rho}\,\tau_{mix}\widetilde{\Theta}(1-\widetilde{\Theta}), \tag{2.4.7}$$

where C_{EBU} is the model constant and τ_{mix} is the turbulence mixing time defined as:

$$\tau_{mix} = \frac{\widetilde{\varepsilon}}{\widetilde{k}}. \tag{2.4.8}$$

Reduced temperature $\widetilde{\Theta}$ can have one of two values: $\widetilde{\Theta} = 0$ in unburned gasses or $\widetilde{\Theta} = 1$ in burnt gasses. Due to the formulation of Equation (2.4.7) this model is often used with the $k-\varepsilon$ turbulence model.

The equilibrium (or infinitely fast) chemistry approach, where the chemical reaction rate is

assumed to be faster than the mixing rate, is generally true for high Re flows. But the EBU model has its limitations. In flows with high turbulence, the EBU model often overestimates the reaction rate, even more so in regions with high strain (large ε/k). In low strain areas (small ε/k) local flame extinction can occur, something that is accounted for in detailed chemistry models. Finally, by relying solely on k and ε to define the combustion rate, the model relies heavily on correctly calculating the turbulence to achieve realistic combustion. Therefore, it is not advisable to use the EBU model on diffusion flames.

2.4.2 Eddy Dissipation Concept (EDC)

Building on the EBU model, the eddy dissipation concept (EDC) was proposed by Ertesvag and Magnussen [33]. EDC is a detailed chemistry model, meaning it is applicable to flows where chemical kinetics are not negligible to turbulent mixing. It was one of the first models capable of treating turbulent diffusive flames, making it widespred and used in many CFD codes [34]. The EDC is based on the energy cascade assumption, where energy is transferred from large to small eddies and, on the smallest scales, to heat [35]. Chemical reactions are assumed to occur only in turbulent fine structures if the conditions are favourable.
The fine structures are characterized by their mass fraction in the computational cell:

$$\gamma^* = 4.6 \left(\frac{\nu \widetilde{\varepsilon}}{\widetilde{k}^2} \right)^{1/2}. \tag{2.4.9}$$

where ν is the kinematic viscosity. The mass transfer between the fine structures and the surrounding turbulent eddies $\dot{m^*}$ is calculated as:

$$\dot{m^*} = 11.2 \frac{\widetilde{\varepsilon}}{\widetilde{k}}. \tag{2.4.10}$$

The reaction rate $\widetilde{\dot{\omega}_s}$ is expressed as:

$$\widetilde{\dot{\omega}_k} = \frac{\overline{\rho} \dot{m^*} \chi}{1 - \gamma^* \chi} \left(\widetilde{Y_s} - \widetilde{Y_s^*} \right) \tag{2.4.11}$$

where $\widetilde{Y_k}$ and $\widetilde{Y_k^*}$ are respectively the mean mass fraction and the fine structure mass fraction of specie k. Probability of ignition χ is the fraction of fine structures that may react. The mean mass fraction $\widetilde{Y_s}$ is obtained by solving the conservation of specie equation (eq. (2.2.11)). Three approaches are available to model $\widetilde{Y_s^*}$ and χ [36]:

- **The fast chemistry approach** where the turbulent mixing is presumed to be much slower than the chemical reaction so infinitely fast chemistry is assumed. In the most basic form, χ only accounts for the probability of coexistence of reactants:

$$\chi = \frac{\widetilde{Y_{pr}}/(1+s)}{\widetilde{Y_{min}} + \widetilde{Y_{pr}}/(1+s)}. \tag{2.4.12}$$

  where Y_{pr} is the product mass fraction, s is the mass stoichiometric ratio and Y_{min} is used to describe the limiting reactant in the reaction (either the fuel or the oxidizer). It is possible to account for more factors by expanding χ to include the degree of heating and the limitation of reaction due to a lack of reactants. The procedure to calculate Y_s^* is available in [36]. However, all factors include the fraction of combustion products $\widetilde{Y_{pr}}$. If there are no combustion products present, the probability of ignition is zero, meaning the flame needs to be initialized using a pilot flame or numerically. Because of this and the limitations of the fast chemistry approach, it is not advised to use this approach to simulate combustion in combustion chambers,

- **The local extinction approach** is based on the fast chemistry approach but expands on it by including a time scale of chemical reactions. It suffers the same drawbacks as other models that assume fast chemistry.

- **The detailed chemistry approach** where fine structures are assumed to be perfectly stirred reactors. These reactors are assumed to perfectly mixed, at constant pressure and adiabatic. The state of the reactor is determined by solving a set of ODEs [36]. By assuming the entire cell is a reactor, the flame thickness is equal to the size of the cell. Therefore, the model is only suitable for use on adequately fine numerical grids, making it impractical for industrial use on large coarse meshes. This issue can be resolved by dividing the computational cells into reacting and non reacting parts, as done in the partially stirred reactor model.

2.4.3 Partially Stirred Reactor (PaSR) Model

The Partially Stirred Reactor (PsSR) model [11][37] is an expansion of the eddy dissipation concept that employs a detailed chemistry assumption, where the finite reaction rate is based both on chemistry and turbulence time scales. The computational domain is divided into a finite number of cells, with each one being divided into a reacting and non reacting part. The reacting part is assumed to be a perfectly stirred reactor where the reactions take place immediatelly. After the reactions take place, the mixing process begins for a mixing time of τ_{mix}. "When the mixing time τ_{mix} is smaller than the chemical characteristic time of the system τ_c ($\tau_{mix} < \tau_c$, κ is close to unity, meaning that mixing is efficient, and the final composition is mainly determined by chemistry. Contrarily, when $\tau_{mix} > \tau_c$) , κ is close to zero and mixing controls the system." [38] The turbulent mixing time is defined as:

$$\tau_{mix} = C_{mix}\sqrt{\frac{\mu_{eff}}{\overline{\rho}\widetilde{\varepsilon}}}, \tag{2.4.13}$$

where effective dynamic viscosity μ_{eff} is the sum of laminar and turbulent dynamic viscosity and C_{mix} is a model parameter usually set between 0.10 and 0.15. The reaction rate is calculated as:

$$\widetilde{\dot{\omega}_k} = \kappa\dot{\omega}_{k,arr}, \tag{2.4.14}$$

The mixed fraction that reacts κ is defined as:

$$\kappa = \frac{\tau_c}{\tau_c + \tau_{mix}}, \tag{2.4.15}$$

where τ_c is the minimum residence time which sustains combustion and is calculated by solving the equation:

$$\frac{1}{\tau_c} = -\frac{\partial\dot{\omega}_k}{\rho\partial Y}. \tag{2.4.16}$$

The partially stirred reactor has the advantages of the EDC with the addition of being able to split a computational cell into a reacting and non reacting part. This is especially important for use in industrial simulations where mesh size is often a limiting factor. By taking into account both the mixing and the chemical time scale, PaSR model can be used on a wide range of reacting flows without "a priori" knowledge of the flow type.

2.5 Conclusion

The mathematical foundation required to properly model turbulent combustion is presented presented in this chapter. The instantaneous governing equations are listed, along with common approaches on simplifying the equations to make them less computationally expensive. Additional expressions needed to close the set of equations are derived. The derivation of Favre averaged equations is shown, as well as the terms that require modelling as a result of the averaging. The final set of equations that need to be solved is listed.

Section 2.3 begins with a brief overview of the methods of modelling the Reynolds stresses. The $k-\varepsilon$ turbulence model is selected for this thesis because of its known properties and simple integration with chemistry models.

Approaches used to model the chemical reaction rate are analysed in Section 2.4. Basic chemistry kinetics is showcased and the reaction rate in laminar flames is computed using the Arrhenius equation. The eddy break up model is presented with its advantages and disadvantages, and found not suitable for this application. A derived model called the eddy dissipation concept is shown, and a variation of the model called the partially stirred reactor model is described and selected as the chemistry model to be used in this thesis.

Chapter 3

Pollutant Modelling

Following worldwide regulations, manufacturers are forced to reduce emissions from aircraft engines. Great strides have been made in reducing the emissions of regulated substances such as CO_2, CO,NOx, UHC, CH_4, CO, SO_x and particle matter (e.g. soot). As Figure 3.0.1 shows, the reduction in NOx emissions has been challenging and difficult to achieve. The umbrella term "NOx" is used for nitrogen compounds that are products of combustion, primarily nitrous oxide (NO) and nitrogen dioxide (NO_2). The term NOx is often used because NO and NO_2 exist in a quasi-equilibrium state. Nitrous oxide (NO) is mostly produced by combustion processes at high temperatures and it is the dominant NOx species in the combustion chamber, while NO_2 concentration is significantly higher in exhaust gasses [39]. After exiting the oxygen-deprived conditions in the combustion chamber, NO reacts with the surrounding air to create NO_2. After exposure to UV light, NO_2 is decomposed into NO and an O atom which reacts with oxygen to form ozone O_3. Ozone acts as a greenhouse gas, absorbing infrared energy emitted by the Earth. Furthermore, ozone is a strong oxidizer that has a negative effect on the respiratory system and rubber and plastic materials [40]. Eventually, NO_2 is oxidized to form nitric acid (HNO_3) that in contact with water forms clouds and produces acid rain.
Nitric oxide (NO) is formed in combustion by three mechanisms [41]:

- **Thermal NOx** formation is the largest contributor to the total NO formulation. Due to the high activation energy required to decompose the strong N_2 triple bond, thermal NO is formed at high temperatures [42](> 1600 K). The formation of thermal NO is de-

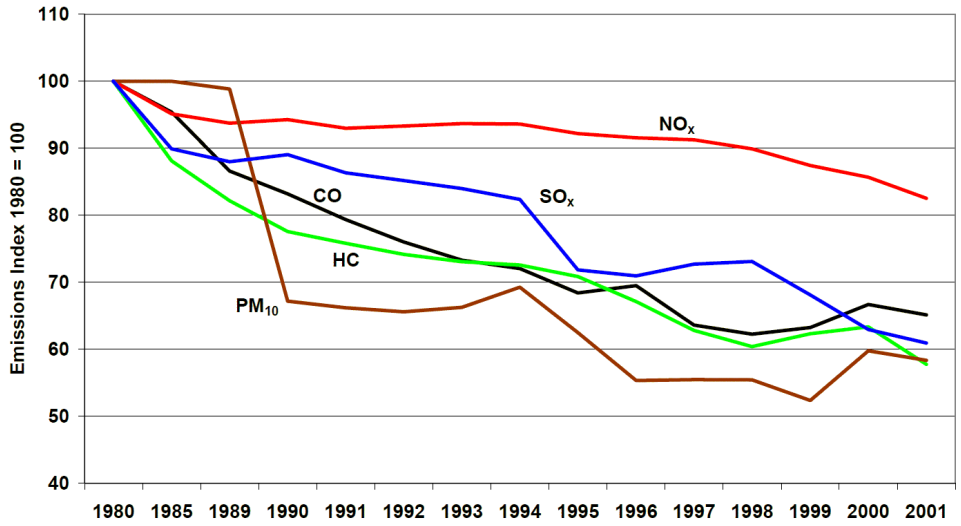

Figure 3.0.1: Emissions index of common pollutants. [3]

scribed by a set of highly temperature-dependant equations called the extended Zeldovich mechanism [12].

- **Prompt NOx** is formed by oxidizing the nitrogen at the flame front in oxygen-deficient regions of the flame. It is characterized by its fast formation (much faster than thermal NO), hence giving the name of the reaction. The total contribution of prompt NO is usually small, except in low temperature, fuel rich conditions with small resident times. Flames in combustion chambers are characterized by high temperatures and a lean mixture, so prompt NOx will not be considered in this thesis. If needed, prompt NOx can be modelled using the Fenimore mechanism [16].

- **Fuel NOx** is formed due to the presence of nitrogen in the fuel. This is especially prevalent in fuel with a high nitrogen concentration, such as heavy oil and coal. Because of this, Fuel NOx formation will not be considered in this thesis.

The largest contributor of NOx in combustion chambers is the thermal NOx mechanism. As mentioned above, the formation of thermal NOx is a relatively slow process and cannot be computed using equilibrium chemistry models. Zeldovich suggested that the thermal NOx mechanism can be decoupled from the primary combustion process if the equilibrium of temperature and species is assumed. Therefore, the extended Zeldovich mechanism is a powerful post-processing tool that can be applied on any data set without requiring the recalculation of the primary combustion process.

3.1 The Extended Zeldovich Mechanism

The extended Zeldovich mechanism [12] states that thermal NOx formation is described by the following set of equations:

$$O + N_2 \underset{K_{r1}}{\overset{K_{f1}}{\rightleftharpoons}} NO + N, \tag{3.1.1}$$

$$N + O_2 \underset{K_{r2}}{\overset{K_{f2}}{\rightleftharpoons}} NO + O, \tag{3.1.2}$$

$$N + OH \underset{K_{r3}}{\overset{K_{f3}}{\rightleftharpoons}} NO + H, \tag{3.1.3}$$

where the reaction rates are given in Table 3.1.1 [7]. The net rate of formation of NO described with Equations (3.1.1) to (3.1.3) is:

$$\frac{d[NO]}{dt} = 2K_{f1}[O][N_2]\frac{\left(1 - \frac{K_{r1}K_{r2}[NO]^2}{K_{f1}[N_2]K_{f2}[O_2]}\right)}{\left(1 + \frac{K_{r1}[NO]}{K_{f2}[O_2]+K_{f3}[OH]}\right)}, \tag{3.1.4}$$

where the square brackets denote the molar concentration of the species. Using Equation (3.1.4) the rate of formation can be determined using six scalar fields: temperature T and concentrations of NO, O, N_2, O_2 and OH. Almost all combustion equations include O_2 and N_2 because the oxidizer is usually air. The temperature field is constructed by solving the enthalpy equation. If the chemistry model does not account for species O, OH and NO, they have to be modelled.

Concentration of O

The impact of the concentration of radical O in the formation of NOx does not have a definite conclusion. Several approaches can be used to determine the concentration of O:

- The predicted concentration approach where the concentration is calculated by the de-

Forward reaction rate $[m^3/(kmol\,s)]$	Backward reaction rate $[m^3/(kmol\,s)]$
$K_{f1} = 1.8 \cdot 10^{11}\, exp\,(-38370/T)$	$K_{r1} = 3.8 \cdot 10^{10}\, exp\,(-425/T)$
$K_{f2} = 1.8 \cdot 10^{7}\, exp\,(-4680/T)$	$K_{r2} = 3.8 \cdot 10^{6}\, exp\,(-20820/T)$
$K_{f3} = 7.1 \cdot 10^{10}\, exp\,(-450/T)$	$K_{r3} = 1.7 \cdot 10^{11}\, exp\,(-24560/T)$

Table 3.1.1: Extended Zeldovich mechanism reaction rates [7].

tailed chemistry during the combustion process. This approach is only applicable if the concentration of O was calculated by the chemistry model,

- The equilibrium approach where species equilibrium is assumed. In some cases, the equailibrium approach has been shown to underpredict the concentration of O by a factor of 10 [42].
- The partial equilibrium approach that introduces the dissociation-recombination process:

$$O_2 + C \rightleftharpoons C + O + O, \tag{3.1.5}$$

where C is the third body.

Assuming that the partial equilibrium approach is used, the concentration of O is calculated using the following equation:

$$[O] = 36.64\,T^{0.5}[O_2]^{0.5}\,exp\,(-27123/T). \tag{3.1.6}$$

Concentration of OH

Several approaches are available when modelling the concentration of OH:

- The predicted OH approach where the concentration is calculated by the detailed chemistry during the combustion process. This is only applicable if the available chemistry model calculated the OH concentration,
- The exclusion of OH approach where the last equation in the extended Zeldovich mechanism (Equation (3.1.3)) is considered to be negligible because $K_{f2}[O_2] \gg K_{f3}[OH]$.
- The partial equilibrium approach where the concentration of OH is derived using the expression:

$$[OH] = 2.129 \cdot 10^2 T^{-0.57}\,exp\,(-4595/T)[O]^{0.5}[H_2O]^{0.5}\,, \tag{3.1.7}$$

which assumes that the concentration of H_2O is known from the initial combustion process. This is a valid assumption because H_2O is a common product in hydrocarbon

combustion mechanisms.

With the expressions for the concentration of O and OH derived, all the terms from Equation (3.1.4) are known, with the exception of the concentration of NO. Because the concentration of NO depends on itself, a transport equation will need to be assembled to properly calculate the concentration of NO.

3.2 NO Transport Equation

Due to its similarity to the conservation of species equation (Equation (2.2.11)), the transport equation will be constructed in a similar manner:

$$\frac{\partial \rho Y_{NO}}{\partial t} + \frac{\partial \rho u_i Y_{NO}}{\partial x_i} = \frac{\partial}{\partial x_i}\left(\rho D_{eff} \frac{\partial Y_{NO}}{\partial x_i}\right) + S_{NO}\,, \tag{3.2.1}$$

where the effective diffusivity D_{eff} can be approximated in the same way as in the specie conservation equation (Equation (2.2.11)). The source term S_{NO} is calculated using Equation (3.1.4) and expression:

$$S_{NO} = M_{NO} \frac{d[NO]}{dt}. \tag{3.2.2}$$

Special care needs to be taken to ensure the values are correctly expressed, either in molar or mass fractions. Equation (3.2.1) needs to be solved iteratively until convergence is achieved.

3.3 Conclusion

This chapter presents the reasoning and motivation behind pollutant modelling, highlighting NOx pollution as an area that requires more attention and further research. Common mechanisms of NOx formation are listed and briefly described. Thermal NOx is identified as the leading cause of NOx emissions in jet engine combustion chambers.

The extended Zeldovich mechanism is presented as a method of calculating NOx emissions in a post-processing mode, based on the specie concentration and temperature distribution of the combustion simulation. Reactions describing the mechanism and reaction rates are given. Different approaches of calculating the concentration of O and OH are presented, and the partial equilibrium approach is selected to be used in this thesis.

Finally, the NO transport equation is assembled from the general conservation equation and the unknown terms are derived.

Chapter 4

Numerical Simulations

In the previous chapters, the governing equations of turbulent combustion and pollutant formation have been derived. The partial differential equation can not be analitically solved and thus a numerical technique is needed to transform the equations into discrete algebraic equations. Several approaches can be used for this purpose, including the finite difference and finite element methods. For fluid flows and mass and heat transfer, the finite volume method (FVM) is preferred. The main advantage of the FVM is its strict conservation, which makes the implementation of conservation laws easier.
To numerically solve the set of continuous partial differential equations, several steps need to be taken [43]:

- **Physical modelling** is the process of describing a process or phenomenon using mathematical expressions. An equally important part is simplifying the equations as much as possible to still truthfully describe the process but reduce the computation time. The final result is a set of partial differential equations which is assembled from the governing equations and additional equations (if needed to close the set of equations),
- **Domain discretization** is the process of dividing the physical domain into smaller, non-overlapping elements called finite volumes. The volumes are defined by vertices, surrounded by faces and each volume has a cell centre. The final result is often called a ”mesh” and can be classified by its structure, cell shape, cell size and many other aspects. The resulting mesh and its quality determine the importance of equation discretization,

- **Equation discretization** is the process of transforming the set of partial differential equations into a set of algebraic equations that will be solved for each cell. This is done by integrating the partial equations over each cell volume and using theorems to transform them into a semi-discretized form. A final disretized form is obtained by approximating the variation between cell centres using discretization stencils,
- **Solving the discretized equations** where the coefficients can be linear, or even non-linear which makes the solution strategy more difficult. The set of equations can be solved directly (i.e. by finding the inverse of a coefficient matrix) or, more often, by using iterative methods where the solution is estimated until convergence is achieved.

More details on the finite volume method and its application in CFD can be found in [44],[43], [16]. The software package used to carry out the numerical simulations is foam-extend [8].

4.1 OpenFOAM

OpenFOAM [45] is "an Open Source object-oriented library for numerical simulations in continuum mechanics written in the C++ programming language. OpenFOAM is gaining considerable popularity in academic research and among industrial users, both as a research platform and a black-box CFD and structural analysis solver. Main ingredients of its design are:

- Expressive and versatile syntax, allowing easy implementation of complex physical model;
- Extensive capabilities, including wealth of physical modelling, accurate and robust discretisation and complex geometry handling, to the level present in commercial CFD;
- Open architecture and open source development, where complete source code is available to all users for customisation and extension at no cost." [46]

A fork of the OpenFOAM called foam-extend [8] is used for the numerical calculations in this thesis. Visualisation of results is done in ParaView [47], an open-source data analysis and visualisation tool. The structure of OpenFOAM in combustion cases consists of four directories: time directories, constant, chemistry and system. The following section will describe the structure of OpenFOAM in more detail and give the basic setup for a combustion case.

4.1.1 Time Directories

The time directories are used to store the results of a simulation in a certain time instance (transient case) or a certain iteration (steady state case). The boundary conditions are also defined for the boundary patches. In the most rudimentary case these include the velocity field U and pressure field p. If the flow is turbulent, additional fields are required, in this case the turbulence kinetic energy k, the rate of dissipation of turbulence energy ε and the resulting turbulent kinematic viscosity ν_t (in case of a incompressible flow) or the turbulent dynamic viscosity μ_t (in case of an compressible flow). To solve the energy equation, the temperature field T and turbulent thermal diffusivity coefficient α_t is needed. In combusting flows, the individual species fields are also required (e.g. CH_4, CO_2, H_2O, N_2, O_2,...). An additional file called *Ydefault* is also often included that defines the boundary conditions for all the species that have not been explicitly set. The boundary conditions differ depending on the flow configuration so they will be explained in detail for the cases in this thesis. The OpenFOAM input/output files follow the C++ syntax as shown below. The example shown is part of the velocity file in time 0 with a no slip boundary condition applied to a wall type patch. The header of the file that includes the version and copyright information is excluded. The first entry determines the dimension of the field using seven SI units. The initial value for the internal cells is given with the keyword *internalField*. Dictionary *boundaryField* contains the boundary patches as defined in the *polyMesh* folder. The velocity on patch *wallTube* is set to a fixed value with all the velocity components set to zero.

```
// * * * * * * * * * * * * * * * * * * * * * * * * * * * * * * * * * * * * * * * * * * * * //
dimensions      [0 1 -1 0 0 0 0];
internalField   uniform (0 0 0);
boundaryField
{
    wallTube
    {
        type            fixedValue;
        value           uniform (0 0 0);
    }
    ...
}
// ************************************************************************* //
```

4.1.2 Constant Directory

The mesh and all the physical and thermal properties are defined in the constant directory. The contents of the directory depend on the case. For example, if gravity or radiation were accounted for, their properties would be defined in the constant directory. In the scope of this thesis, the following files are included:

polyMesh

The numerical grid or mesh are defined in the folder *polyMesh*. The folder contains multiple files containing mesh information such as the boundary, faces, points,... . The details of the used meshes will be shown for each case.

turbulenceProperties

File *turbulenceProperties* defines the type of turbulence modelling used, for example laminar, RANS or LES. In this thesis Reynolds (Favre) turbulence modelling is used (as described in Section 2.3), so the simulation type is set to *RASModel*.

RASProperties

File *RASProperties* includes detailed information about the turbulence model. *RASModel kEpsilon* sets the used model to the k-ε turbulence model. Optional entries include the *kEpsilonCoeffs* where the coefficients of the model are entered (see Equation (2.3.7)) and *wallFunctionCoeffs* where wall function coefficients can be altered.

thermophysicalProperties

File *thermophysicalProperties* is used to construct a thermophysical model class. In this thesis the *hsPsiMixtureThermo<reactingMixture<gasThermoPhysics>>* model is used. The arguments have the following meaning:

- *hs* denotes the use of the sensible enthalpy equation for the conservation of energy equation,
- *Psi* denotes the use of compressibility $\psi = (RT)^{-1}$ [48]. *PsiThermo* model treats the pressure implicitly to deal with compressibility. This makes them more suitable for flows with larger pressure jumps (e.g. combusting flows),
- *reactingMixture* is used in cases where there are chemical reactions and thus the gas composition is variable. If there are no chemical reactions *pureMixture* can be used to specify the mixture composition,
- *gasThermoPhysics* specifies the use of Sutherlands Law (Equation (2.1.6)) and the ideal gas assumption (Equation (2.1.16)).

The keyword *chemistryReader* is used to set the format of the *foamChemistryFile* file. It can be in the CHEMKIN or OpenFOAM format. In this thesis the OpenFOAM format is used. The *foamChemistryFile* and *foamChemistryThermoFile* are the locations of the chemistry/species file and the thermal properties file respectively.
In some codes the species conservation equation (eq. (2.2.11)) is solved only for N-1 species. The remaining specie N is assumed to be chemically inert and its concentration is obtained using the following equation:

$$Y_N = 1 - \sum_{k=1}^{N-1} Y_k. \tag{4.1.1}$$

The inert species is often assumed to be N_2. Using Equation (4.1.1) increases numerical stability by absorbing all the inconsistencies introduced by using Fick's law (Equation (2.1.3)). The syntax is as follows:

```
// * * * * * * * * * * * * * * * * * * * * * * * * * * * * * * * * * * * * * * * * * * * * //
// thermophysicalProperties
thermoType      hsPsiMixtureThermo<reactingMixture<gasThermoPhysics>>;
chemistryReader                 foamChemistryReader;
foamChemistryFile               "$FOAM_CASE/chemistry/ch4oneStep";
foamChemistryThermoFile         "$FOAM_CASE/chemistry/thermo.OF";
inertSpecie                     N2;
// ************************************************************************* //
```

chemistryProperties

Additional chemistry options are defined in *chemistryProperties*. Keyword *chemistry* determines whether the simulation will account for the chemistry, including the transport of species, chemical reactions and heat released due to combustion. If *turbulentReaction* is set to *no*, the solver assumes the flame to be laminar and the PaSR parameter C_{mix} (Equation (2.4.13)) is set to zero. If set to *yes*, C_{mix} is set to the value defined next to the matching keyword. C_{mix} is usually set between 0.001 and 0.3 [49].

The *psiChemistryModel* expands the base chemistry model by adding a thermodynamic package and ODE functions. It introduces the chemistry equation system and evaluation of chemical source terms. The *chemistrySolver* keyword is used to define the chemistry solver type, in this case an ordinary differential equation (ODE) solver. In the first solver iteration the chemical time step can not be properly defined so it needs to be set using the *initialChemicalTimeStep* keyword. Finally, *odeCoeffs* is used to define the ODE solver and its parameters. In the example below, the semi-implicit Burlish-Stoer (SIBS) solver [50] is used.

```
// * * * * * * * * * * * * * * * * * * * * * * * * * * * * * * * * * * * * * * * * * * * * * * * * * * * * //
// chemistryProperties
chemistry           on;
turbulentReaction   on;
psiChemistryModel   ODEChemistryModel<gasThermoPhysics>;
chemistrySolver     ode;
Cmix                Cmix [ 0 0 0 0 0 0 0 ] 0.15 ;
initialChemicalTimeStep     1.0e-5;
odeCoeffs
{
    ODESolver       SIBS;
    eps             5.0e-4;
    scale           1.0;
}
// ********************************************************************************************* //
```

4.1.3 Chemistry Directory

The chemistry directory is created to access the relevant chemistry files more easily. The directory consists of the chemistry file and the chemistry thermodynamic file.

Chemistry file

The chemistry file lists the species and reaction mechanisms used to model the chemical reaction rate. It is structured in two main blocks: the species block and the reactions block. The chemistry file in OpenFOAM format has the following syntax:

```
// * * * * * * * * * * * * * * * * * * * * * * * * * * * * * * * * * * * * * * * * * * * * //
// ch4oneStep
species
5
(
CH4
O2
N2
CO2
H2O
);
reactions
1
(
    irreversibleArrheniusReaction
    CH4^0.7 + 2O2^0.8 = CO2 + 2H2O
    (9.48683e+11 0 23650)
);
// ************************************************************************* //
```

The first entry in the species block is the number of species in the reaction, followed by listing the relevant species. It is important to note that the species need to be written in the same format as listed in the time directories and as in the chemistry thermodynamic file. By the same logic, the reactions block starts with an integer that denotes the number of reactions. The keyword *irreversibleArrheniusReaction* states that the reaction is irreversible and that the reaction rates are calculated using the Arrhenius law (Equation (2.4.6)). Arrhenius law is often modified to model the global reaction more realistically by adding a dependency on the fuel and oxidizer

concentration in the form of reaction coefficients a and b:

$$K_{fj} = A_{fj} T^{\beta_j} \exp\left(-\frac{E_j}{RT}\right) [Fuel]^a [O_2]^b \tag{4.1.2}$$

The reaction coefficients are written behind the species, e.g 0.7 for CH_4. The numbers below the reaction are the reaction rate constants (starting from the left):

- the preexponential constant $A_{fj} = 9.48683e11\,[(m^3/kmol)^{r-1}s^{-1}]$,
- the temperature exponent $\beta_j = 0\,[-]$,
- the activation temperature $T_j = E_j/R = 23650\,[K]$.

where r is the sum of the reaction coefficients a and b.

The standard format for most CFD codes is the CHEMKIN format [51]. The CHEMKIN format is similar to the OpenFOAM format with the addition of the block *Elements* where all the elements are numbered. The reaction coefficients are defined using the keyword FORD. The same one-step combustion reaction in CHEMKIN format has the following syntax:

```
// * * * * * * * * * * * * * * * * * * * * * * * * * * * * * * * * * * * * * * * * * * * * * //
// ch4oneStepChemkin
ELEMENTS
C H O N
END
SPECIE
CH4 O2 N2 CO2 H2O
END
REACTIONS
    CH4 + 2O2 => CO2 + 2H2O        3e13  0.0  47e3
    FORD / CH4 0.7 /
    FORD / O2 0.8 /
//  ********************************************************************** //
```

where the numbers following the chemical equation denote (from left):

- the preexponential constant $A_{fj} = 3e13\,[(cm^3/mol)^{r-1}s^{-1}]$,
- the temperature exponent $\beta_j = 0\,[-]$,
- the activation temperature $T_j = E_j/R = 47e3\,[cal/mol]$.

As seen above, the units of the reaction rates differ depending on the format. Special care

is needed when writing the reaction rates as there is no standard unit set. As many combustion mechanisms are available in the CHEMKIN format, conversion to OpenFOAM format is possible using the *chemkinToFoam* utility.

Thermodynamic file

The thermodynamic file is a list of NASA polynomial coefficients used to calculate specie thermodynamic properties. The file is constructed out of specie blocks where the properties of each specie are defined. The specie block (in this case for O_2) has the following syntax:

```
// * * * * * * * * * * * * * * * * * * * * * * * * * * * * * * * * //
// thermo.OF
O2 O2    1    31.9988
200  5000      1000
3.69758 0.00061352 −1.25884e−07 1.77528e−11 −1.13644e−15 −1233.93 3.18917
3.21294 0.00112749 −5.75615e−07 1.31388e−09 −8.76855e−13 −1005.25 6.03474
1.67212e−06 170.672
// ************************************************************** //
```

The first line contains the specie name and the specie molar mass (in this case 31.9988). The second line denotes the temperature ranges, the low temperature range (200 – 1000 K) and the high temperature range (1000 – 5000 K). The third line defines the polynomial coefficients a_1 to a_7 that are used to calculate the heat capacity c_p (Equation (2.1.18)), enthalpy h (Equation (2.1.20)) and formation enthalpy $\Delta h^0_{f,k}$ for the high temperature range. The following seven numbers do the same for the low temperature range. The final two numbers are constants A_s and T_s used in Sunderland's formula (Equation (2.1.6)). The GRI-Mech 3.0 [52] thermodynamical file is used for all the test cases in this thesis. For more information on the JANAF coefficients and the derivation of the equations, the reader is referred to [53] and [52].

4.1.4 System Directory

The system directory contains the user specified parameters that are used in the solution procedure, as well as files required to decompose the domain so it can be run in parallel. It consists of the following four files:

- *decomposePar* is used to set how the domain will be decomposed in case of a parallel run. This is usually done automatically, however in combustion cases it is good practice to decompose the domain manually if possible. Since solving the mechanisms is more computationally expensive than solving the transport equations, it is recommended to decompose the domain so that the flame is equally distributed on each processor.

- *fvSchemes* is used to set the discretization schemes. The derivation of the discretization schemes is outside the scope of this thesis but more information can be found in [44] and [43]. The schemes used in this thesis are:

```
// * * * * * * * * * * * * * * * * * * * * * * * * * * * * * * * * * * * * * * * * * * * * //
// fvSchemes
ddtSchemes \\ time derivatives
{    default          Euler;}
gradSchemes \\ gradient
{    default          Gauss linear;}
divSchemes \\ divergence
{
    default      Gauss upwind;;
    div(phi,Yi_h) Gauss multivariateSelection
    {
        hs  vanLeer;
        CH4 vanLeer01;
        ... \\ same for all species
    };
    div((muEff*dev2(T(grad(U))))) Gauss linear;
}
laplacianSchemes \\ laplacian
{    default          Gauss linear corrected;}
interpolationSchemes \\interpolation  between points
{    default          linear;}
snGradSchemes \\ gradient normal cell face component
{    default          corrected;}
// ************************************************************************* //
```

- *fvSolution* is where the linear equation solvers, tolerances and other algorithm controls are set. The number of outer and inner loops in the PIMPLE algorithm is prescribed here.

- *controlDict* is used to control the simulation run parameters such as the simulation duration, time step and write controls and formats. It is possible to automatically calculate

the time step size to obey the maximal Courant number *Co*:

$$Co = \Delta t \sum_{i=1^3} \frac{u_i}{\Delta x_i}. \tag{4.1.3}$$

The time step Δt is determined by setting the maximum Courant value, usually between 0.1 and 0.3.

4.2 The Solution Procedure

Simulating combustion presents a problem from a numerical perspective, because of the large gradients of temperature, and consequently pressure. Therefore, cases are usually initialized by calculating a quasi-steady non-combusting state that is set as an initial value for the combusting case. The solver *reactingFoam* is used, an compressible solver able to simulate chemical reactions, based on the PIMPLE algorithm. PIMPLE combines the PISO and SIMPLE algorithms, so the pressure-velocity coupling is solved for each time step. The main difference between the PISO and PIMPLE algorithm is the inclusion of outer correction loops used to converge the explicit parts of the equation. By setting the outer loops to 1 (using the keyword nOuterCorrectors), the PIMPLE algorithm operates in PISO mode. The use of outer loops allows the PIMPLE algorithm to operate in larger time steps (Co $>$ 1).

4.3 Conclusion

This chapter starts with a brief presentation of the steps required to model combustion using CFD. A finite volume based, open-source software called foam-extend (a fork of OpenFOAM) is used for numerical simulations in this thesis. The required structure of the cases is explained in detail, presenting the capabilities of combustion simulations in foam-extend. Special attention is given to present the numerical implementation of chemistry and thermophysical properties. Finally, the numerical settings and the solution procedure are explained.

Chapter 5

Sandia Flame D Validation Case

In this chapter, the solver *reactingFoam* using the k-ε turbulence model and the PaSR chemistry model are validated using Sandia Flame D, a piloted diffusion flame. Section 5.1 examines the experimental setup, specified boundary conditions and the experimental data format. The combustor model geometry and the computational domain discretisation is shown in Section 5.2, including the resulting two-dimensional and three-dimensional computational meshes.
Section 5.3 deals with the initial and boundary conditions, which are explained, derived and presented in tabular form. Three reaction mechanisms of different complexity (1, 4 and 325 reactions) are presented in Section 5.4, along with their respective chemical reactions and reaction rates.
The results of the simulations are presented in Section 5.6. The results of the two-dimensional and three-dimensional case are compared with experimental results to observe if three-dimensional effects have a significant impact on numerical results. The influence of chemistry reaction mechanisms on temperature and species concentration is examined in Section 5.6.3. The extended Zeldovich mechanism is implemented on the produced results of the lower complexity reaction mechanisms and compared to experimental NOx concentrations. Additionally, the NOx results produced directly by the complex model are compared to the results of the extended Zeldovich mechanism constructed from the results of the complex chemistry case, with and without modelling the O and OH concentrations.

5.1 Sandia Flame D Experimental Setup

As part of the 1999 *International Workshop on Measurement and Computation of Turbulent Nonpremixed Flames*, extensive measurements were made by Sandia National Laboratories on a series of flames to provide researchers with well documented validation cases. Often referred to simply as Sandia Flames, these experimental flames have become a staple within the combustion comunity, frequently used as validation cases for various combustion models because of the large data set and detailed documentation [4]. Sandia Flames D, E and F are piloted CH_4/air turbulent diffusion flames with increasing jet velocities and local extinction. For the purposes of the validation of the PaSR combustion model and the extended Zeldovich mechanism, Sandia Flame D (Figure 5.1.1) will be used as a validation case in this thesis.

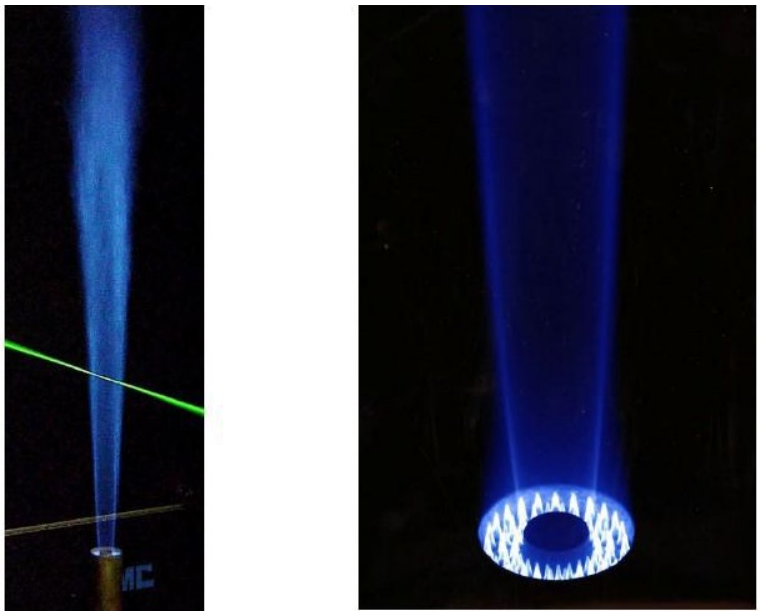

Figure 5.1.1: Sandia Flame D (left) and close-up of the pilot flame (right). [4]

Several scalars were measured using Raman/Rayleigh and Laser-Induced Fluorescence (LIF), including temperature and mixture fractions of N_2, O_2, H_2O, H_2, CH_4, CO, CO_2, OH and NO. Laser Doppler velocimetry (LDV) measurements were carried out at the Technical University of Darmstadt. The data set includes single measurements (6000 measurements for Flame D) as well as Reynolds and Favre averaged mass fractions and root mean square fluctuations for radial and axial profiles. The experimental setup is presented in detail in [4].

5.2 Computational Domain

Sandia Flame experiments used the same burner geometry [4] as in previous investigations of piloted flames at Sydney University and Sandia Laboratories. The burner geometry is shown in Figure 5.2.1, where the main jet (d= 7.2 mm), pilot jet (d_p = 18.2 mm) and coflow air are coloured in green, magenta and blue, respectively. The burner consists of a main jet with a

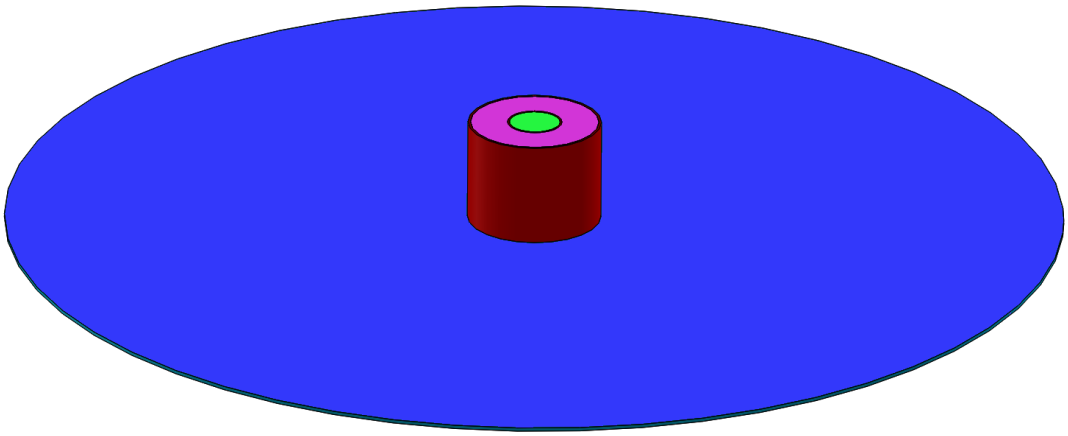

Figure 5.2.1: Sandia Flame D geometry.

chemical composition of 25 % methane / 75 % air by volume, a pilot jet in which the conditions simulate burnt gas, and a coflow jet of air in normal conditions. The boundary conditions of the jet are given in Table 5.2.1.

The domain discretisation was done using Pointwise [54], a powerful commercial tool used for grid generation and preprocessing of computational grids used for computational fluid dynamics. Two computational grids were created, one for the two-dimensional case and one for the three-dimensional case, in order to compare the results.

	Velocity [m/s]	Temperature [K]	CH_4 [1]	O_2 [1]	H_2O [1]	CO_2 [1]	N_2 [1]
Main jet	(49.6, 0, 0)	294	0.1561	0.1966	0	0	0.6473
Pilot jet	(11.4, 0, 0)	1880	0	0.054	0.0942	0.1098	0.742
Coflow jet	(0.9, 0, 0)	291	0	0.23	0	0	0.77

[1] Specie mass fraction

Table 5.2.1: Sandia D experimental boundary conditions.

Two-Dimensional Computational Mesh

OpenFOAM is a three-dimensional solver that requires the computational mesh to have three dimensions. The case is reduced to two dimensions using specific boundary conditions (such as *empty* or *wedge*). The created structured two-dimensional computational mesh can be seen in Figure 5.2.2. Mesh size is approximately 4500 cells, all hexahedra except for the prismatic cells around the x-axis. Figure 5.2.3 shows the inlets of the main jet (coloured in green) and pilot jet (coloured in magenta) with a small gap in between (coloured in red). The coflow jet is coloured blue and extends further up. The inlets have been extended so that the pipe flow is fully developed before entering the main domain. The mesh represents a five degree portion of the domain and assumes symmetry about the x-axis.

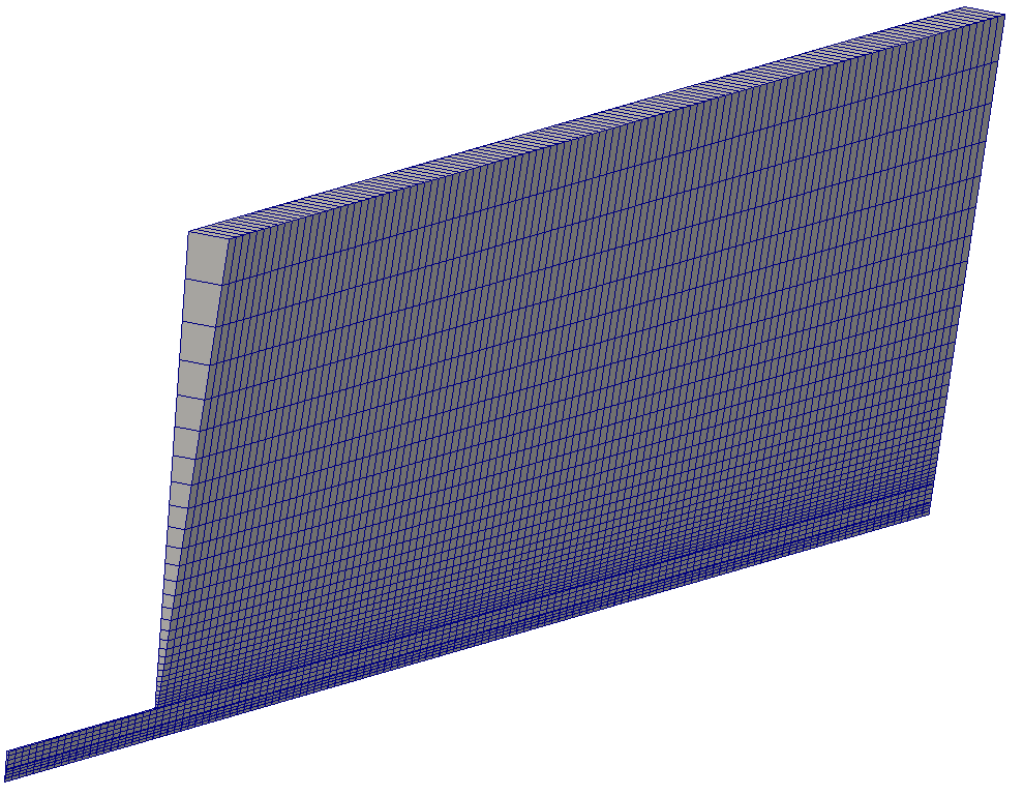

Figure 5.2.2: Sandia Flame D two-dimensional domain.

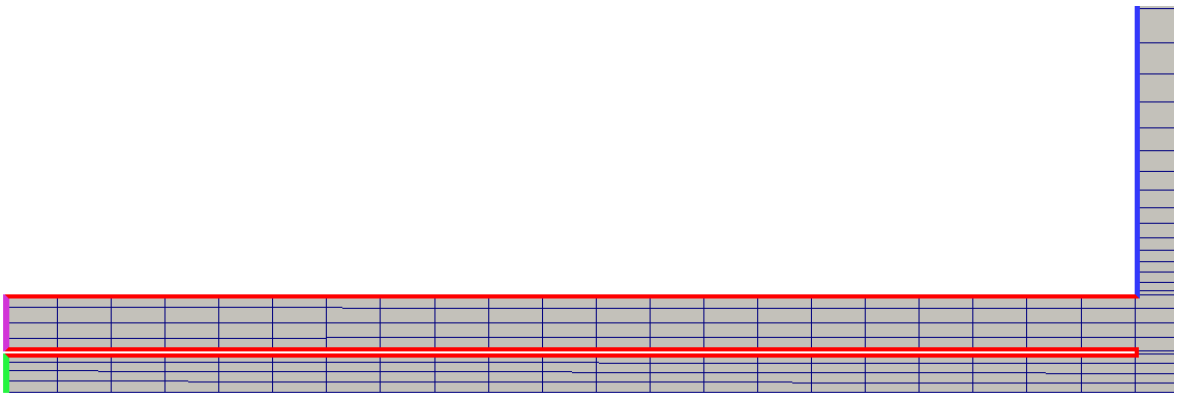

Figure 5.2.3: Sandia Flame D two-dimensional domain - detailed.

3D Computational Mesh

A three-dimensional mesh was created to explore the influence of three-dimensional effects on the flow structure and flame front. The mesh represents a quarter of the physical domain. The resulting structured computational mesh (Figure 5.2.4) is composed of approximately $500,000$ cells, all hexahedra. To avoid prismic cells along the x-axis, the cells were created using the

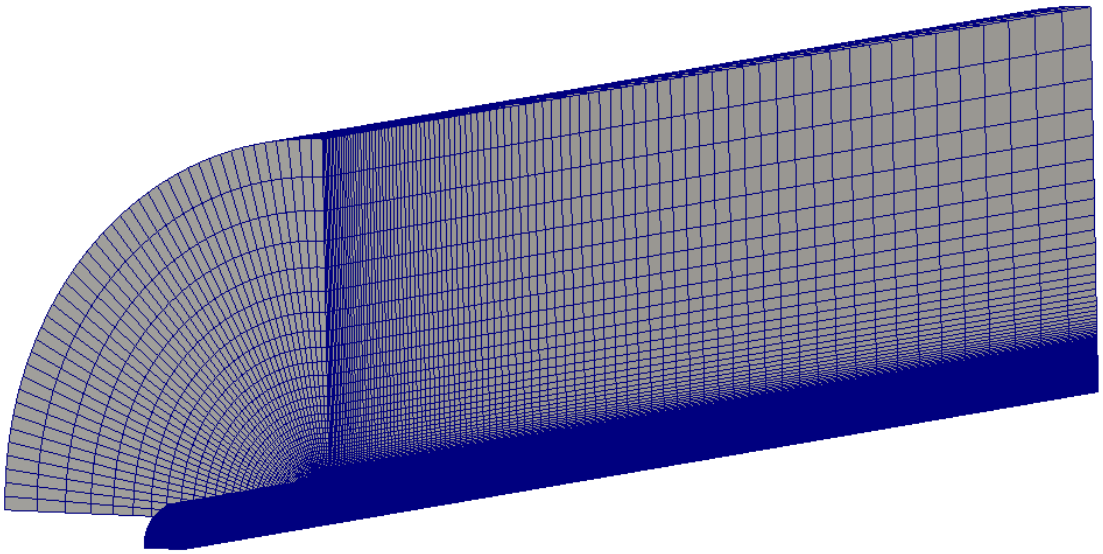

Figure 5.2.4: Sandia Flame D three-dimensional domain.

O-H grid method to create a structured circular grid (Figure 5.2.5). Boundary patches are the same as with the two-dimensional mesh.

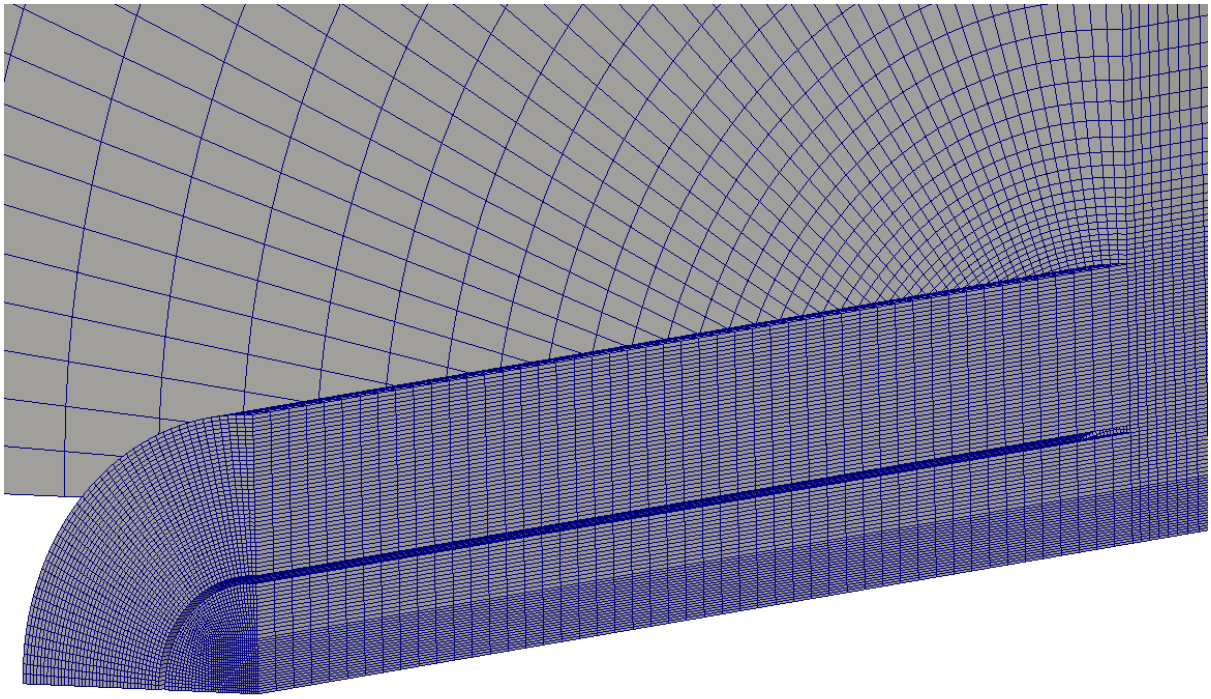

Figure 5.2.5: Sandia Flame D three-dimensional domain - detailed.

5.3 Boundary Conditions

The boundary conditions (BCs) for the Sandia Flame D can be derived from Table 5.2.1. The velocities, temperatures and mass fractions for the jets (inlets) are prescribed using the Dirichlet boundary condition with the keyword *fixedValue*. On all other patches, a Neumann boundary condition (keyword: *zeroGradient*) is set for these variables. The remaining boundary conditions are shown in Table 5.3.1. Pressure is set to a Neumann BC at the inlet and a Dirichlet BC at the outlet. Velocity and pressure boundary conditions are often set this way to increase numerical stability. Turbulent kinetic energy is set using the *turbulentIntensityKineticEnergyInlet* boundary condition where k is calculated by specifying the turbulent intensity I using the following formula:

$$k = \frac{3}{2}(I|u|)^2, \tag{5.3.1}$$

where $|u|$ is the absolute value of the velocity vector defined as:

$$|u| = \sqrt{u_1^2 + u_2^2 + u_3^2}. \tag{5.3.2}$$

The turbulent dissipation rate ε is set using the *turbulentMixingLengthDissipationRateInlet* boundary condition where ε is calculated as:

$$\varepsilon = \frac{C_{mu}^{0.75} k^{1.5}}{L} \tag{5.3.3}$$

where C_{mu} is a constant usually set to 0.09, and the length scale L is defined by the user. Turbulent thermal diffusivity α_t is set to *calculated*, meaning it is derived from the turbulent dynamic viscosity, calculated from Equation (2.3.6). For wall patches, the turbulent kinetic energy, dissipation rate, thermal diffusivity and dynamic viscosity are prescribed using their respective wall functions. All fields were initialized to match the conditions on the *inletAir* patch. The only difference in boundary conditions between the two-dimensional and three-dimensional cases is in the treatment of the patches that indicate symmetry. In the two-dimensional case, the side patches are set to the *wedge* boundary condition, used exclusively for axi-symmetric cases where the mesh is one cell thick. In contrast, the symmetry patches in the three-dimensional case are set to cyclic, a patch type used for repeating geometries. Figure 5.3.1 shows the face connectivity of select faces on the symmetry patches after running *createPatch*. Table 5.3.1 shows the prescribed boundary conditions for the two-dimensional case. In the two-dimensional case all the boundary conditions on the side patches are set to *wedge*, and in the three-dimensional case they are set to *cyclic*.

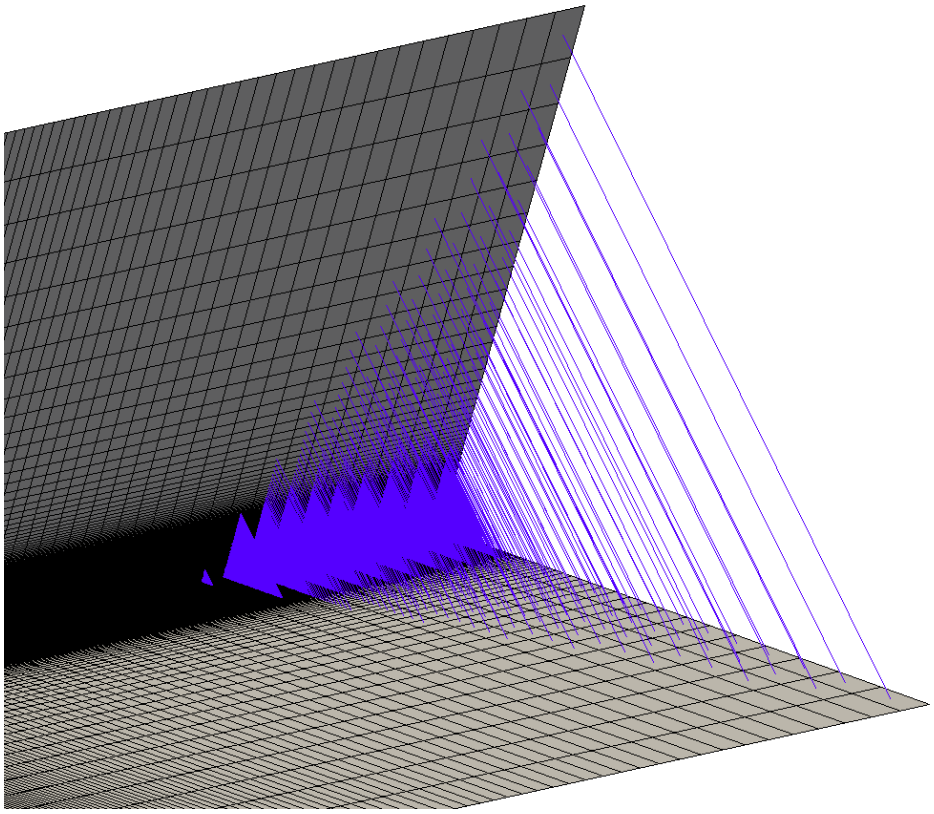

Figure 5.3.1: Sandia Flame D face connectivity.

	Pressure [Pa]	k	ε	μ_t	α_t
inletCH4	*zeroGradient*	$I = 0.0458$	$L = 0.000504$	*calculated*	*calculated*
inletPilot	*zeroGradient*	$I = 0.0628$	$L = 0.000735$	*calculated*	*calculated*
inletAir	*zeroGradient*	$I = 0.0471$	$L = 0.019677$	*calculated*	*calculated*
wallTube	*zeroGradient*	*kqRWF*	*epsilonWF*	*mutWF*	*alphatWF*
wallOutside	*zeroGradient*	*kqRWF*	*epsilonWF*	*mutWF*	*alphatWF*
outlet	$10 \cdot 10^5$	*zeroGradient*	*zeroGradient*	*calculated*	*calculated*

kqRWF - kqRWallFunction *epsilonWF - epsilonWallFunction*

mutWF - mutWallFunction *alphatWF - alphatWallFunction*

Table 5.3.1: Sandia D experimental boundary conditions.

5.4 Reaction Mechanisms

Three reaction mechanisms are used in this thesis, each with a different level of complexity, to explore the effect of the chemistry complexity on the results. Thermochemistry (i.e. formation enthalpy, heat capacities and species mass fractions) controls the maximum flame temperature and are constant for all cases. On the other hand, chemical parameters (i.e. preexponential constant, temperature exponent and activation temperature) are derived from the reaction mechanism and control the combustion rate [9]. While the reduced mechanisms only compute the concentrations of main reaction products, the complex chemistry mechanism computes the O and OH fields required for the extended Zeldovich mechanism, thus removing the need to model the respective fields. The reaction mechanisms are as follows:

One-step mechanism

The one-step mechanism reported by Christ [49] consists of five species and one reaction:

$$CH_4 + 2O_2 \rightarrow CO_2 + 2H_2O\,. \tag{5.4.1}$$

The reaction mechanism is written using the global reaction formulation (Equation (4.1.2)) with the reaction coefficients listed in Table 5.4.1.

Reaction	a	b	r	$A_f\,[(m^3/kmol)^{r-1}s^{-1}]$	$\beta_j\,[-]$	$T_j\,[K]$
reaction 5.4.1	0.7	0.8	1.5	$9.48683 \cdot 10^{11}$	0	23650

Table 5.4.1: One-step methane combustion reaction coefficients.

Four-step mechanism

The four-step mechanism described by Jones and Lindstedt [55] consists of seven species and four reactions:

$$2CH_4 + O_2 \rightarrow 2CO + 4H_2\,, \tag{5.4.2}$$

$$CH_4 + H_2O \rightarrow CO + 3H_2\,, \tag{5.4.3}$$

$$CO + H_2O \underset{b}{\overset{f}{\rightleftharpoons}} CO_2 + H_2\,, \tag{5.4.4}$$

$$2H_2 + O_2 \underset{b}{\overset{f}{\rightleftharpoons}} 2H_2O. \tag{5.4.5}$$

The reaction coefficients are specified in Table 5.4.2. Even though the reaction mechanism consists of only four reactions, it takes into account CO, a common combustion product and major pollutant.

Reaction	a	b	r	$A_f\,[(m^3/kmol)^{r-1}s^{-1}]$	$\beta_j\,[-]$	$T_j\,[K]$
reaction 5.4.2	0.5	1.25	1.75	$4.4 \cdot 10^{11}$	0	15095
reaction 5.4.3	1	1	2	$3 \cdot 10^{8}$	0	15095
reaction 5.4.4 f	1	1	2	$2.75 \cdot 10^{9}$	0	10065
reaction 5.4.4 b	1	1	2	$6.71 \cdot 10^{10}$	0	13688
reaction 5.4.5 f	1	0.5	1.5	$7.91 \cdot 10^{10}$	0	17609
reaction 5.4.5 b	1	–	1	$3.48 \cdot 10^{13}$	0	47907

Table 5.4.2: Four-step methane combustion reaction coefficients.

Complex chemistry

The complex chemistry model is derived from the GRI-Mech 3.0 reaction mechanism [15]. It is composed of 53 species and 325 chemical reactions. The mechanism accounts for species O and OH directly, allowing the application of the extended Zeldovich mechanism without modelling the fields.

5.5 Simulation Settings

After creating the computational grids in Pointwise, mesh renumbering is executed using the command *renumberMesh* to reduce matrix bandwidth and speed up computation. Solver *reactingFoam* is used with the numerical and chemistry settings listed in Table 5.5.1. When using the reduced chemistry mechanisms, the inert species is set to N_2 because there are no chemical reactions where nitrogen is a reactant or product. If the complex chemistry mechanism is used in which nitrogen participates in chemical reactions, argon (Ar) is specified as a chemically inert specie. Argon is chosen as the inert specie because it is highly chemically inert and present in the atmosphere in small concentrations. The computational domain is deconstructed along the x-axis into four subdomains and the simulations are run in parallel.

PIMPLE	nOuterCorrectors nCorrectors	2 2
solvers	p|rho hs|k|epsilon|Yi	CG BiCGStab
schemes	ddtSchemes gradSchemes divSchemes laplacianSchemes interpolationSchemes snGradSchemes	Euler Gauss linear Gauss upwind Gauss linear corrected linear corrected
chemistry	inertSpecie	N2 or AR
chemistrySolver	SIBS Cmix initialChemicalTimestep	eps = 5e-4 0.15 1e-5

Table 5.5.1: Numerical settings for the Sandia Flame D test case.

5.6 Results

The Sandia Flame D dataset consists of specie concentration, temperature, velocity and turbulent kinetic energy measurements. Measurements are taken at different axial positions expressed using the main jet diameter d, starting from the burner exit at x/d= 1 to the flame tip x/d= 75. At each axial position, the radial profile is gathered and scaled, once again, using the main jet diameter d. After simulation convergence is achieved (at $t = 0.2s$), results are extracted using a line sample with 100 points at each axial position. When available, root mean square fluctuations are added to the discrete experimental data points. The flame shape is shown in Figure 5.6.1 using the temperature field.

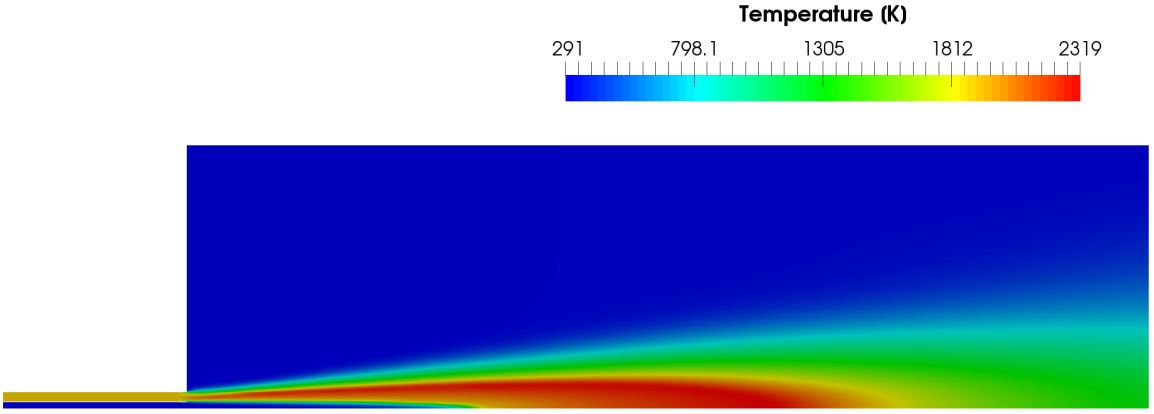

Figure 5.6.1: Sandia Flame D flame shape.

5.6.1 Impact of Three-Dimensional Effects on Simulation Results

In order to reduce computation time, three-dimensional cases can be simplified and assumed to be two-dimensional. In the case of the Sandia Flame D experiment where the geometry and boundary conditions are axi-symmetric, the computational geometry can be reduced to a smaller section. This simplification ignores the three dimensional effects that can have a significant influence of flames. For comparison, using the same one-step chemistry (5.4.1), time step based on the maximum Courant number ($Co_{max} = 0.25$) and with three inner correctors, the simulation execution times for the two-dimensional and three-dimensional simulations are 29 minutes and 700 hours, respectively. The execution time is reduced by a factor of 1450

when using the two-dimensional mesh, mainly due to the fact that the computational mesh is smaller by a factor of a thousand. The results from the five degree wedge case and the results from the one quarter geometry case will be compared to experimental results to confirm that the axi-symmetric assumption is valid.

CH_4 mass fraction

The mass fraction of CH_4, calculated using the two-dimensional and three-dimensional mesh, is compared to experimental results in Figure 5.6.2. The results of the three-dimensional simulation give slightly higher concentrations of CH_4, especially in the regions further from the flame (5.6.2.d).

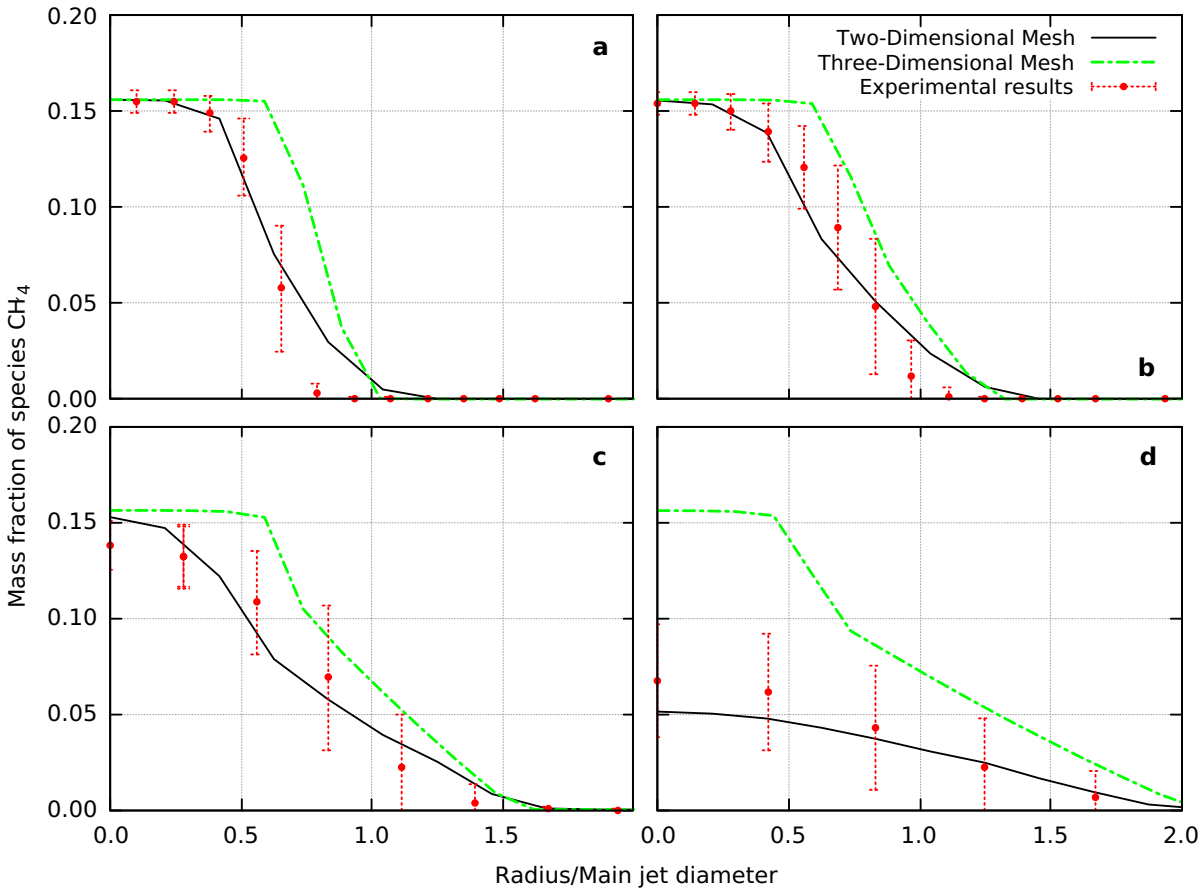

Figure 5.6.2: Mass fraction of specie CH_4 at axial distances: a) x/d= 3, b) x/d= 7.5, c) x/d= 15, d) x/d= 30.

O_2 mass fraction

As shown in Figure 5.6.3, the two-dimensional and three-dimensional simulations results predict similar concentrations of O_2. The disagreement between the two-dimensional and three-dimensional results at $x/d = 3$ (Figure 5.6.3.a) is the results of the domain discretisation. Due to the higher cell count, the three-dimensional mesh is able to capture high concentration gradients more accurately (Figure 5.6.3.d).

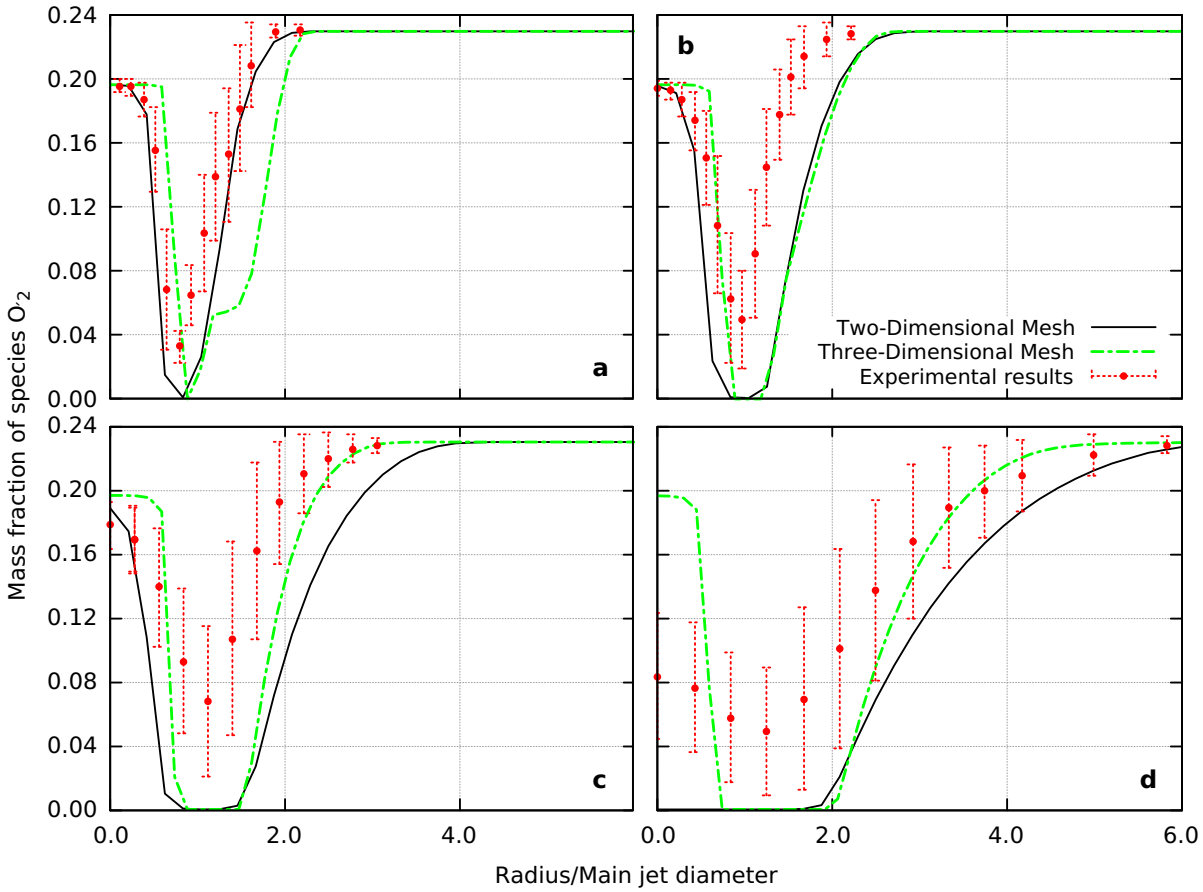

Figure 5.6.3: Mass fraction of specie O_2 at axial distances: a) x/d= 3, b) x/d= 7.5, c) x/d= 15, d) x/d= 30.

CO_2 mass fraction

Concentration of CO_2 is calculated in Figure 5.6.4. Higher concentration of CO_2 is expected because a one-step reaction mechanism is used. The largest error is visible in Figure 5.6.4.d, where the two-dimensional simulation largely overpredicts the concentration, while the three-dimensional simulation calculates a significantly lower concentration near the x-axis.

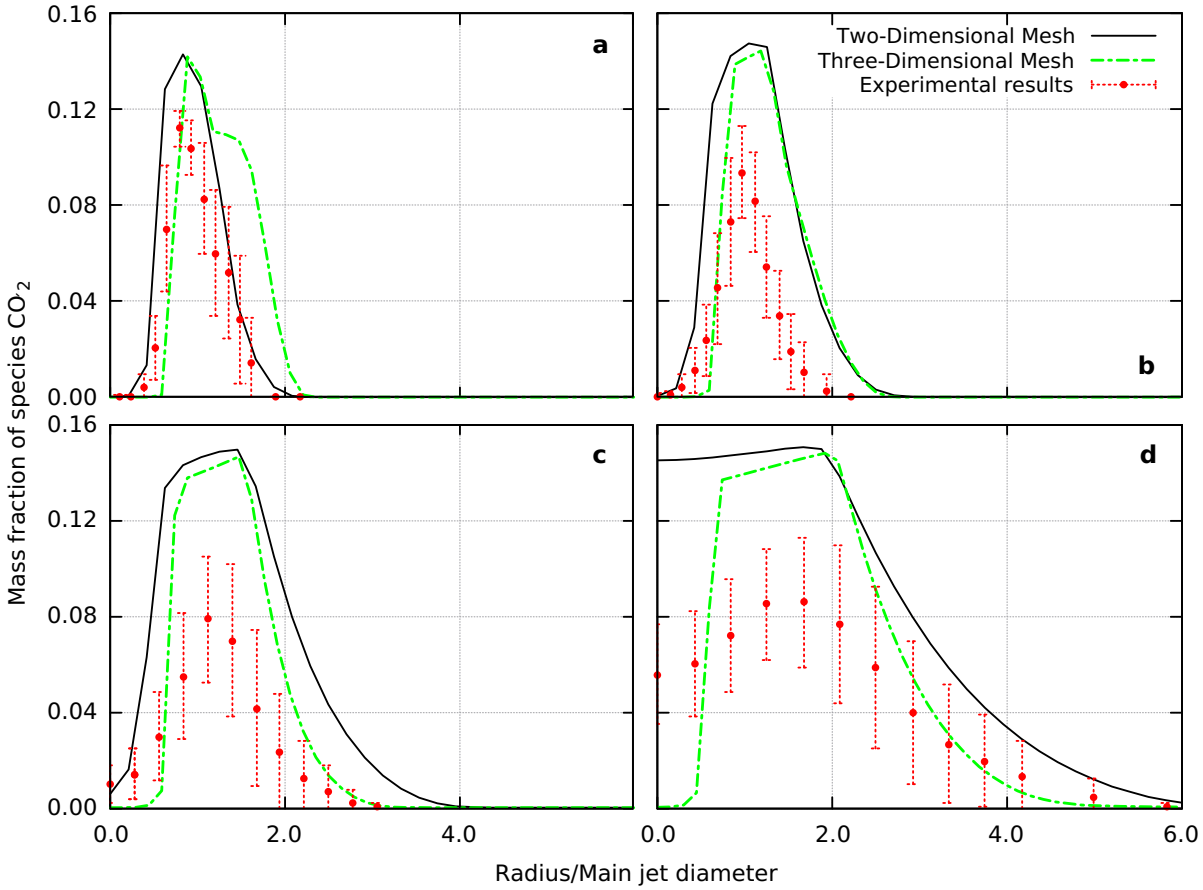

Figure 5.6.4: Mass fraction of specie CO_2 at axial distances: a) x/d= 3, b) x/d= 7.5, c) x/d= 15, d) x/d= 30.

H_2O mass fraction

The concentration of H_2O is overpredicted by the single-step chemistry mechanism in all parts of the flame. The three-dimensional mesh results better match the experimental results in the middle of the flame (Figure 5.6.5.b and 5.6.5.c). Once again, it can be seen that the numerical results are unable to correctly predict the flame shape at the symmetry axis (Figure 5.6.5.d).

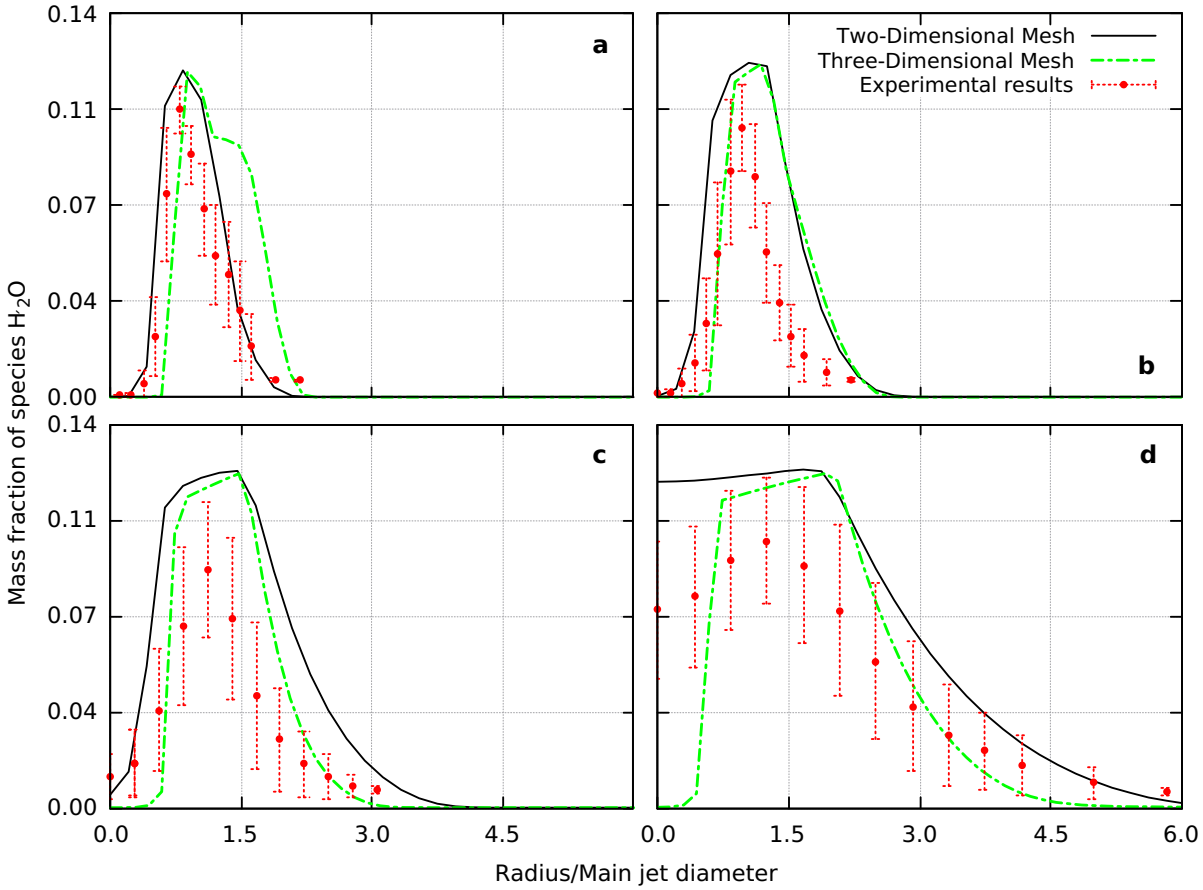

Figure 5.6.5: Mass fraction of specie H_2O at axial distances: a) x/d= 3, b) x/d= 7.5, c) x/d= 15, d) x/d= 30.

Temperature

The temperature comparison is shown in Figure 5.6.6. The temperature and reaction product concentration graphs are very much alike, as expected. The computation results match the experimental fairly well in the entire domain, except at the flame front near the axis of symmetry. The two-dimensional grid results indicate that the interior flame front tip (as seen on Figure 5.6.1) is upstream of x/d= 30, while the three-dimensional grid results indicate it is downstream. Overall, the simulation results are a good match to experimental data.

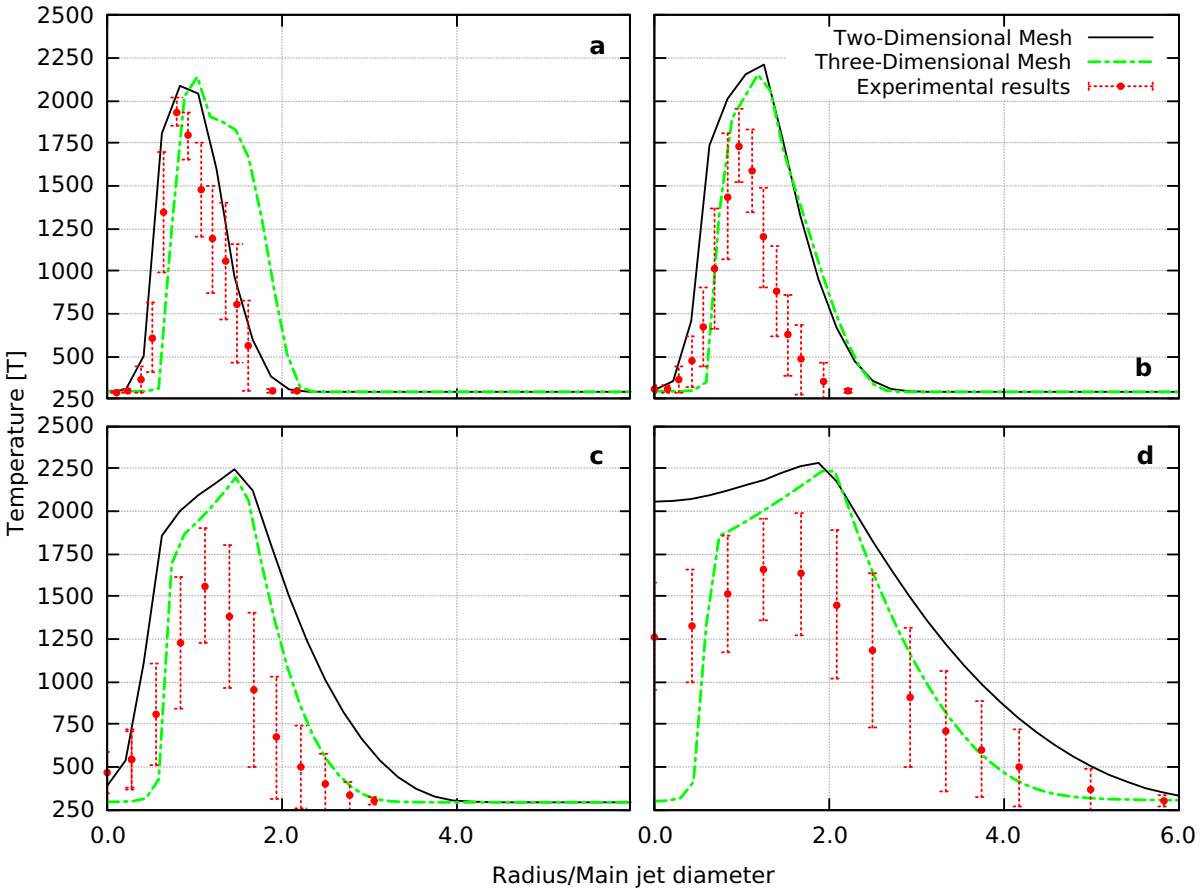

Figure 5.6.6: Temperature at axial distances: a) x/d= 3, b) x/d= 7.5, c) x/d= 15, d) x/d= 30.

5.6.2 The Impact of Reaction Mechanisms on Simulation Results

The use of different reaction mechanisms can have several effects on simulation results. Simpler chemistry mechanisms often exclude the complex pollution forming mechanisms that usually have a slower reaction times than combustion. Additionally, pollutant forming reactions are often endothermic, lowering the overall temperature of the mixture. The difference in temperature causes a difference in pressure, subsequently changing the velocity field. Moreover, a lower temperature may cause some of the fuel to stay unburned, thus increasing the concentration of unburned hydrocarbons (UHC). Due to the interaction between chemistry and turbulence, special care needs to be taken when using reduced chemistry mechanisms. In this section, the results of simulations using reaction mechanisms of different complexity (presented in Section 5.4) are compared with experimental data. The results are presented for individual species and temperature for easier review.

CH_4 mass fraction

In the near flame region, all three chemistry mechanisms show good agreement with the experimental data. In areas where large gradients of CH_4 concentration are present, as seen in Figure 5.6.7.a, the mechanisms fail to model it accurately. This is an inherent flaw of all CFD simulations, caused by a finite number of cells in the computational domain, causing so called numerical diffusion. In the middle part of the flame, all combustion mechanisms show a good match to experimental data with minor differences (Figure 5.6.7.b). Near the flame tip, the one-step combustion mechanism matches the experimental data most accurately (Figure 5.6.7.c). A larger concentration of fuel in the flame tip indicates that the one-step model has a lower combustion rate than the more complex models. This is also apparent in Figure 5.6.7.d, where the single-step mechanism is the only mechanism that shows any remaining CH_4 in the domain. The y-axis in Figure 5.6.7.d is rescaled accordingly to present the differences better.

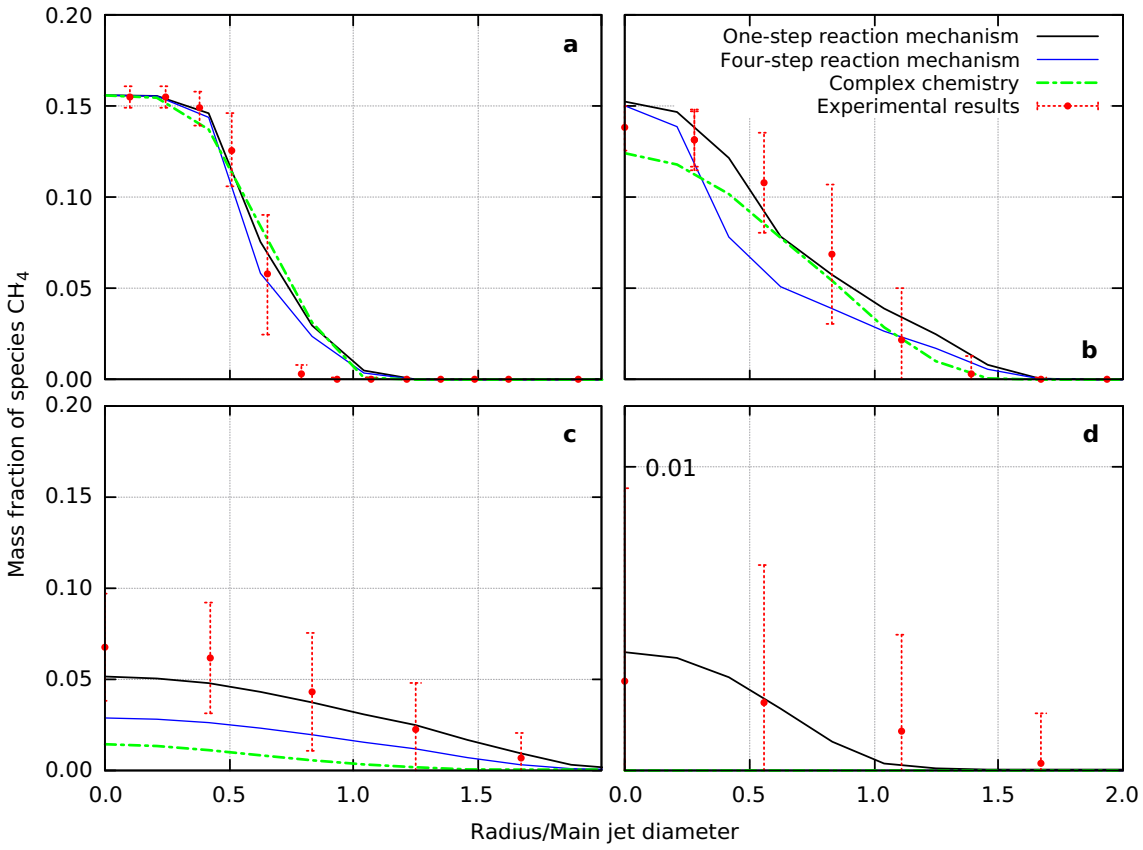

Figure 5.6.7: Mass fraction of specie CH_4 at axial distances: a) x/d= 1, b) x/d= 15, c) x/d= 30, d) x/d= 45.

O_2 mass fraction

At the burner base, both the one-step and four-step mechanisms show the concentration of O_2 to be zero, indicating that O_2 is a limiting specie in the near flame region. However, experimental data shows this is not true, and the complex chemistry mechanism is capable of modelling this region realistically (Figure 5.6.8.a). The same is true further downstream from the flame (Figure 5.6.8.b). At x/d= 30 (Figure 5.6.8.c), all mechanisms show a significantly lower O_2 concentration than experimental data. Approaching the flame tip (Figure 5.6.8.d), the four-step chemistry model shows a lower O_2 concentration that other models and experimental data.

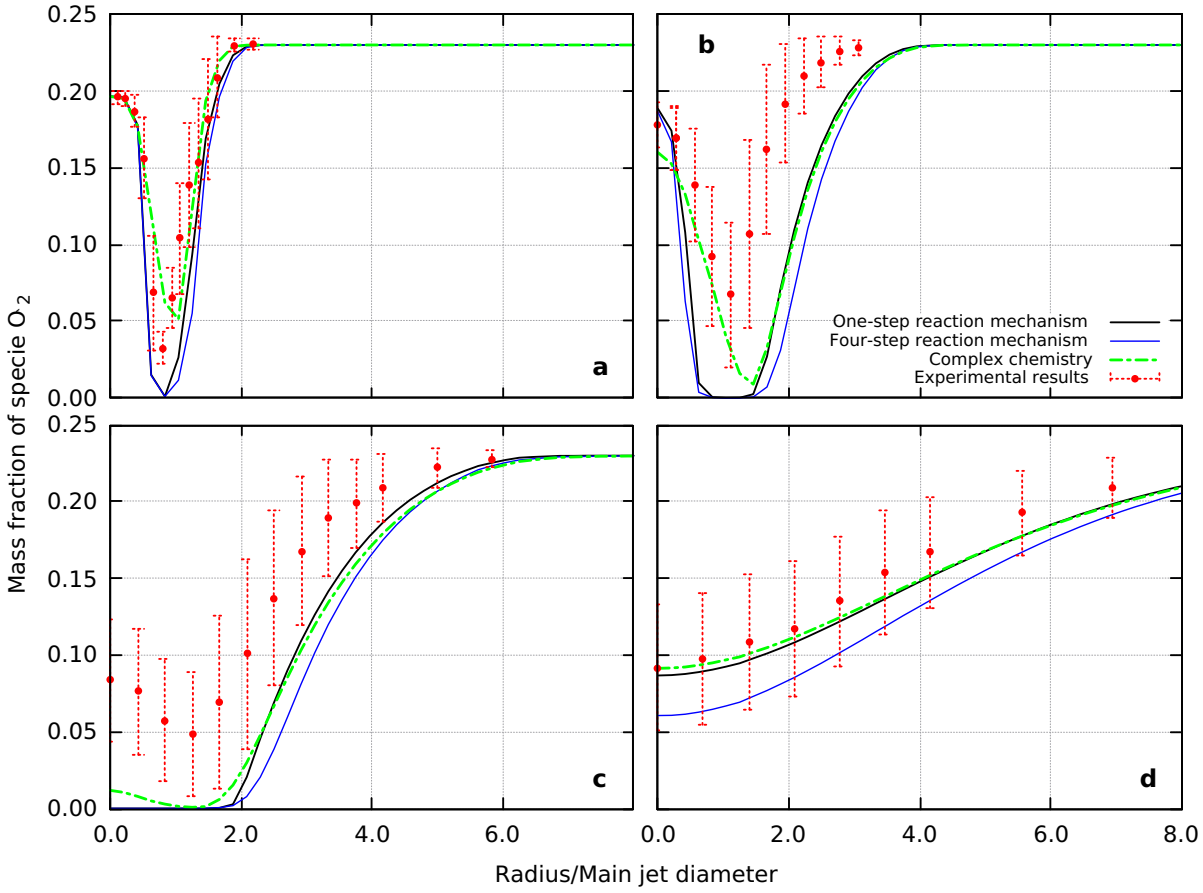

Figure 5.6.8: Mass fraction of specie O_2 at axial distances: a) x/d= 3, b) x/d= 15, c) x/d= 30, d) x/d= 60.

CO_2 mass fraction

The one-step reaction mechanism simplifies the combustion of CH_4 to one chemical reaction, with the only products being CO_2 and H_2O. Other products are excluded, most notably CO. Therefore, the one-step mechanism shows higher concentrations of CO_2 in combustion regions. The error is small near the burner (Figure 5.6.9.a), grows higher as the flame advances (Figure 5.6.9.b), and shows a large error at the part of the flame with the highest reaction rate (Figure 5.6.9.c). At the flame tip, the results show a better match to experimental data (Figure 5.6.9.d). The four-step mechanism and the complex chemistry mechanism show better agreement with experimental data, but consistently overpredict the CO_2 concentration in the entire domain.

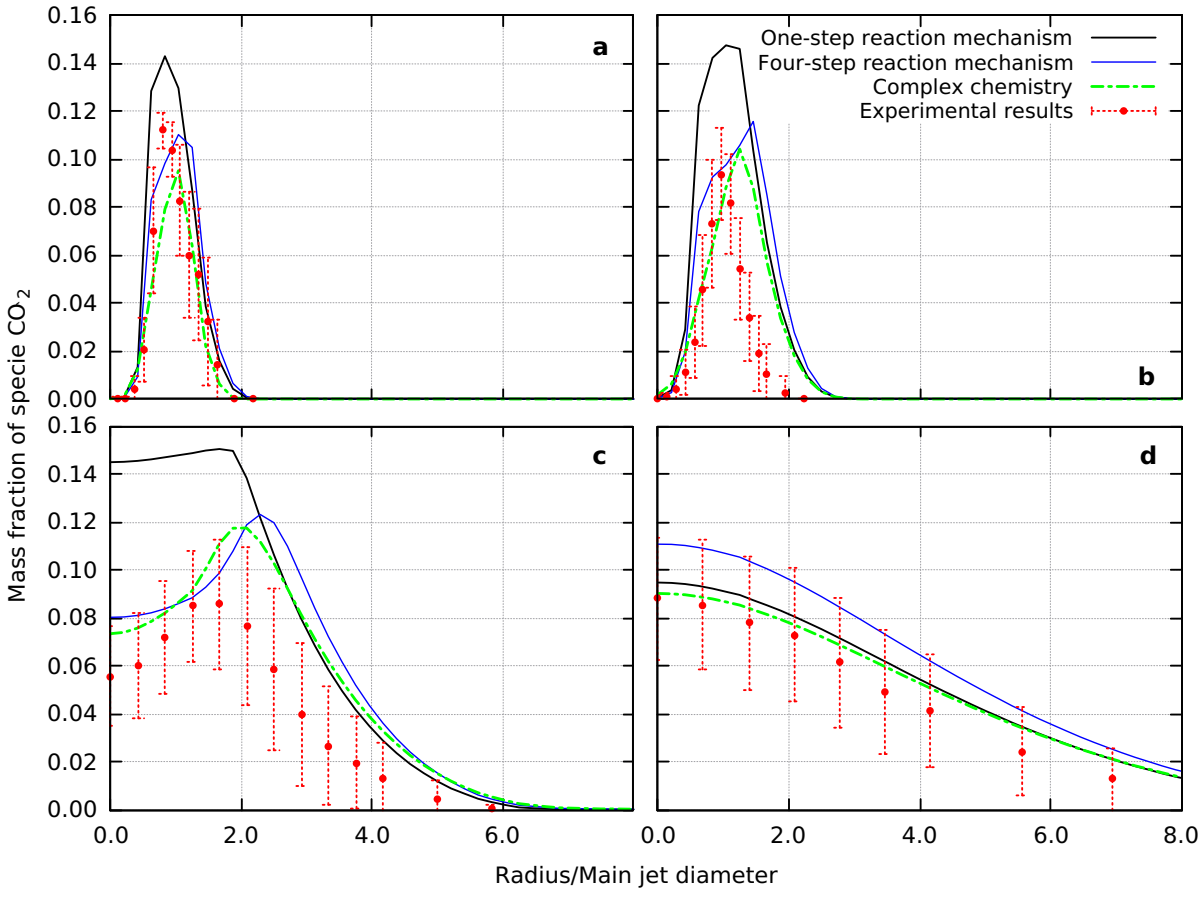

Figure 5.6.9: Mass fraction of specie CO_2 at axial distances: a) x/d= 3, b) x/d= 7.5, c) x/d= 30, d) x/d= 60.

H_2O mass fraction

All the reaction mechanisms predict H_2O concentration accurately near the burner exit (Figure 5.6.10.a), with the complex chemistry model calculating a lower concentration than experimental results suggest. Larger difference between the simulations and experimental data can be seen in Figure 5.6.10.b. Over-estimation of H_2O is expected for reduced mechanisms, however, complex chemistry shows similar results. All reaction mechanisms perform better downstream (Figure 5.6.10.c), with the four-step mechanism performing the worst but still remaining within the result spread (Figure 5.6.10.d).

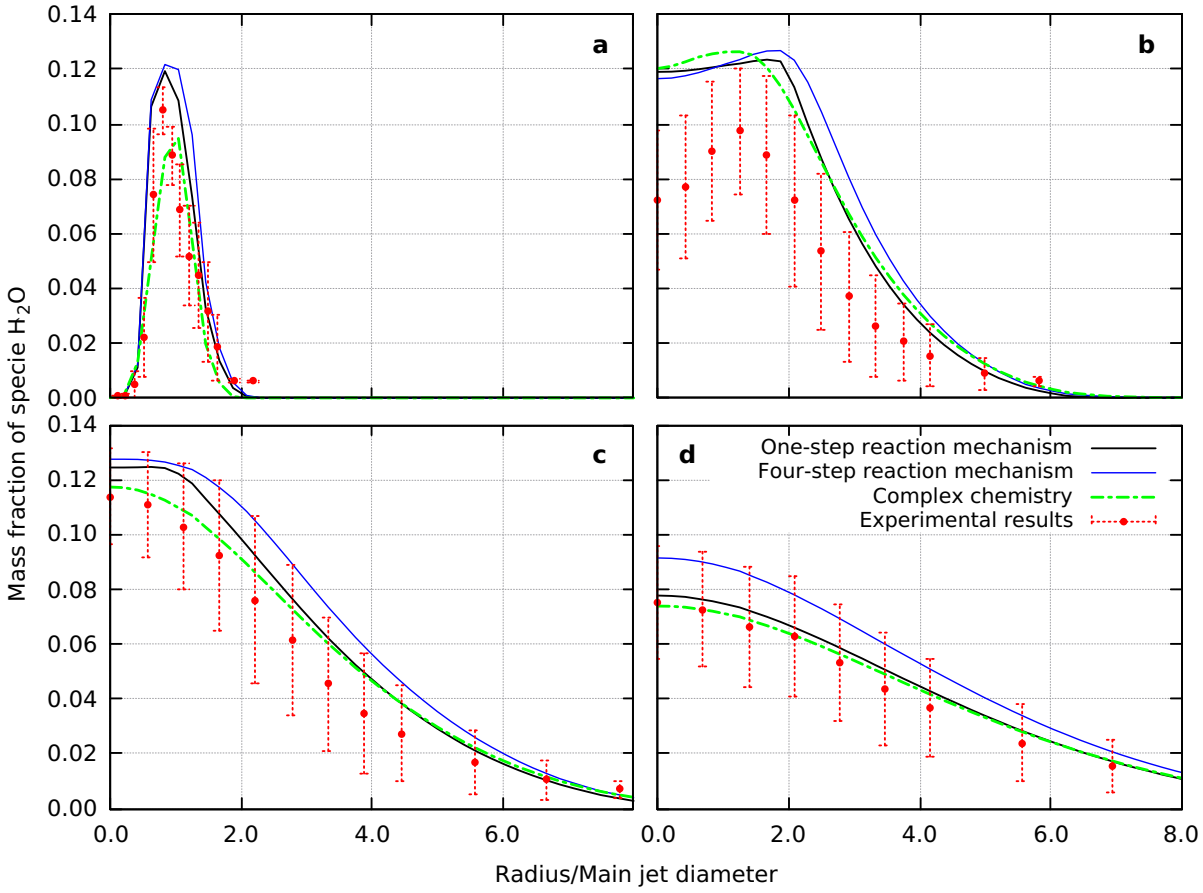

Figure 5.6.10: Mass fraction of specie H_2O at axial distances: a) x/d= 3, b) x/d= 30, c) x/d= 45, d) x/d= 60.

N_2 mass fraction

Figure 5.6.11.a shows the N_2 concentration near the burner exit. Results from all three reaction mechanisms match the experimental results fairly well (Figure 5.6.11.b). Proceeding downwind, simulation results exhibit lower concentrations than the experimental data. The complex chemistry mechanism gives a slightly higher concentration of N_2 which is rather counter-intuitive since it is the only mechanism able to simulate thermal NOx production. However, the lower concentration of N_2 near the burner axis (Figure 5.6.11.c) is a consequence of the composition of the main jet, where 25% of the jet (by volume) is methane. The higher concentration of N_2 when using the complex chemistry model is likely a result of differences in the flow field, allowing for better penetration of atmospheric N_2 into the flame structure. The concentrations of N_2 near the flame tip are similar for all mechanisms and are in accordance with experimental data (5.6.11.d).

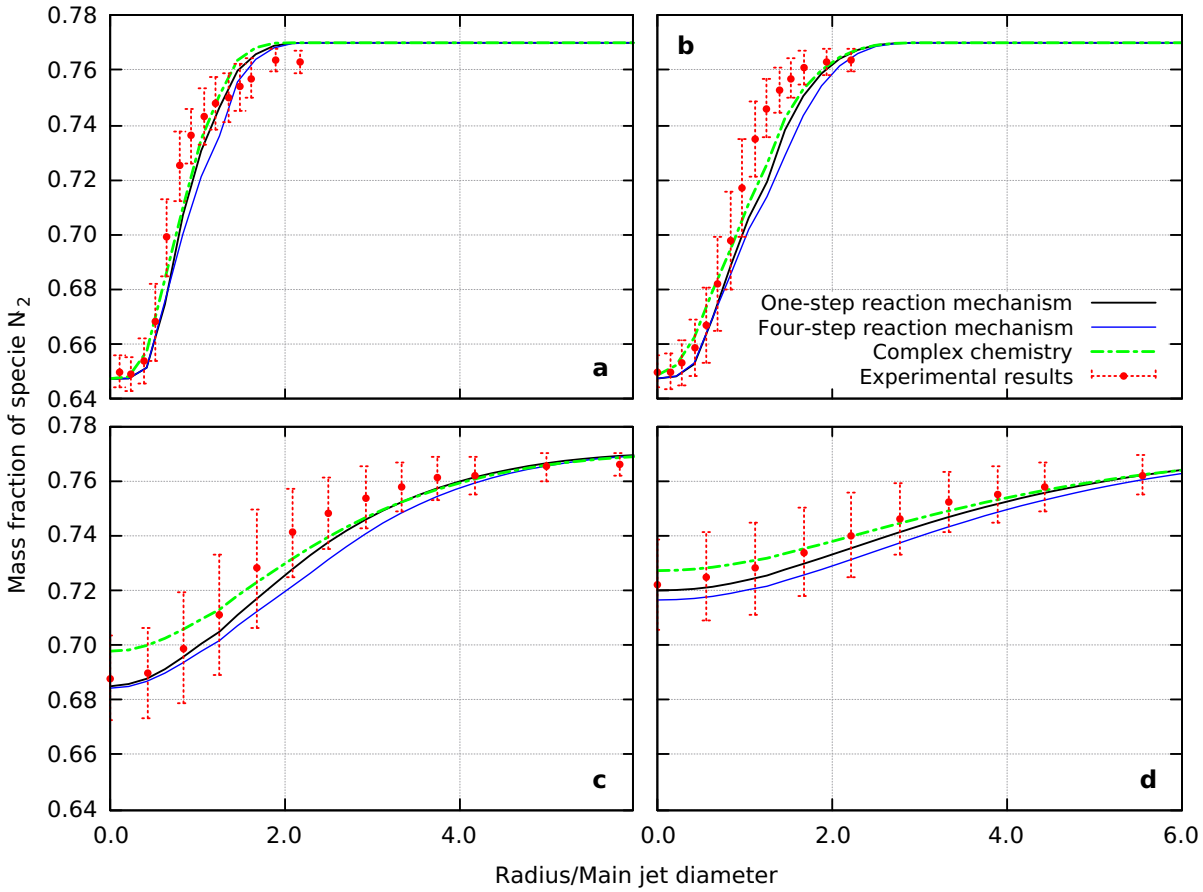

Figure 5.6.11: Mass fraction of specie N_2 at axial distances: a) x/d= 3, b) x/d= 7.5, c) x/d= 30, d) x/d= 45.

Temperature

As mentioned in Chapter 3, NOx production is strongly dependant on the temperature field. Therefore, accurately predicting the temperature is very important. At the burner exit (Figure 5.6.12.a), one-step and four-step reaction mechanisms show higher temperatures than experimental results (by approximately 150 K). This is to be expected, as endothermic pollutant forming reactions are excluded in reduced mechanisms. Further away from the burner (Figure 5.6.12.b), all chemistry mechanisms seem to underpredict the temperature by a large margin, 400 K for the complex chemistry mechanism and approximately 650 K for the reduced mechanisms. There are a few things to note, starting with the simplifications made to the heat transfer. No radiative or wall transfer heat was modelled. This can have a influence on the results, but since this is an open flame with no nearby walls, the heat transfer should be minimal. Another factor are the inherent instabilities in the flame front which can be seen by the large error bars (Figure 5.6.12.c). By taking these factors into account, the simulation results seem more reasonable. Interestingly, one-step and complex chemistry mechanisms results near the flame tip (Figure 5.6.12.d) are within the root mean square error, with the four-step mechanism showing higher temperatures in the entire domain.

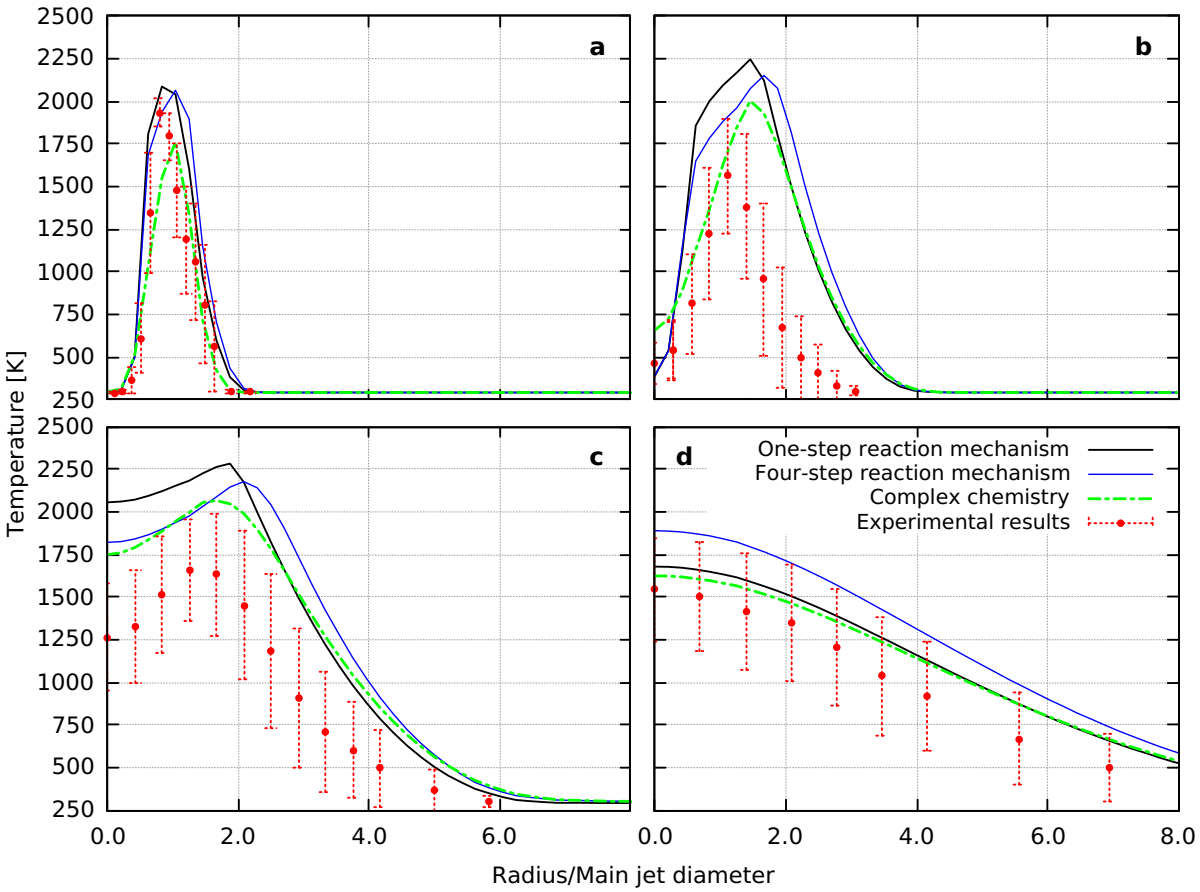

Figure 5.6.12: Temperature at axial distances: a) x/d= 3, b) x/d= 15, c) x/d= 45, d) x/d= 60.

5.6.3 The Impact of Reaction Mechanisms on NOx Formation

The extended Zeldovich mechanism uses Equation (3.1.4) to calculate the production of NO. The formation of NO depends on the temperature field as well as the concentration of NO, N_2, O_2, O and OH species. In the previous section, temperature and species concentration computed using different reaction mechanisms were compared with experimental results. Generally speaking, the simulations were able to accurately represent both temperatures and species concentration. In this section, the extended Zeldovich mechanism is applied to the results and the calculated NO formation is compared to experimental data. Equation (3.2.1) is solved using an iterative process. Figure 5.6.13 shows the concentration of NO after 1, 10, 100 and 1000 iterations.

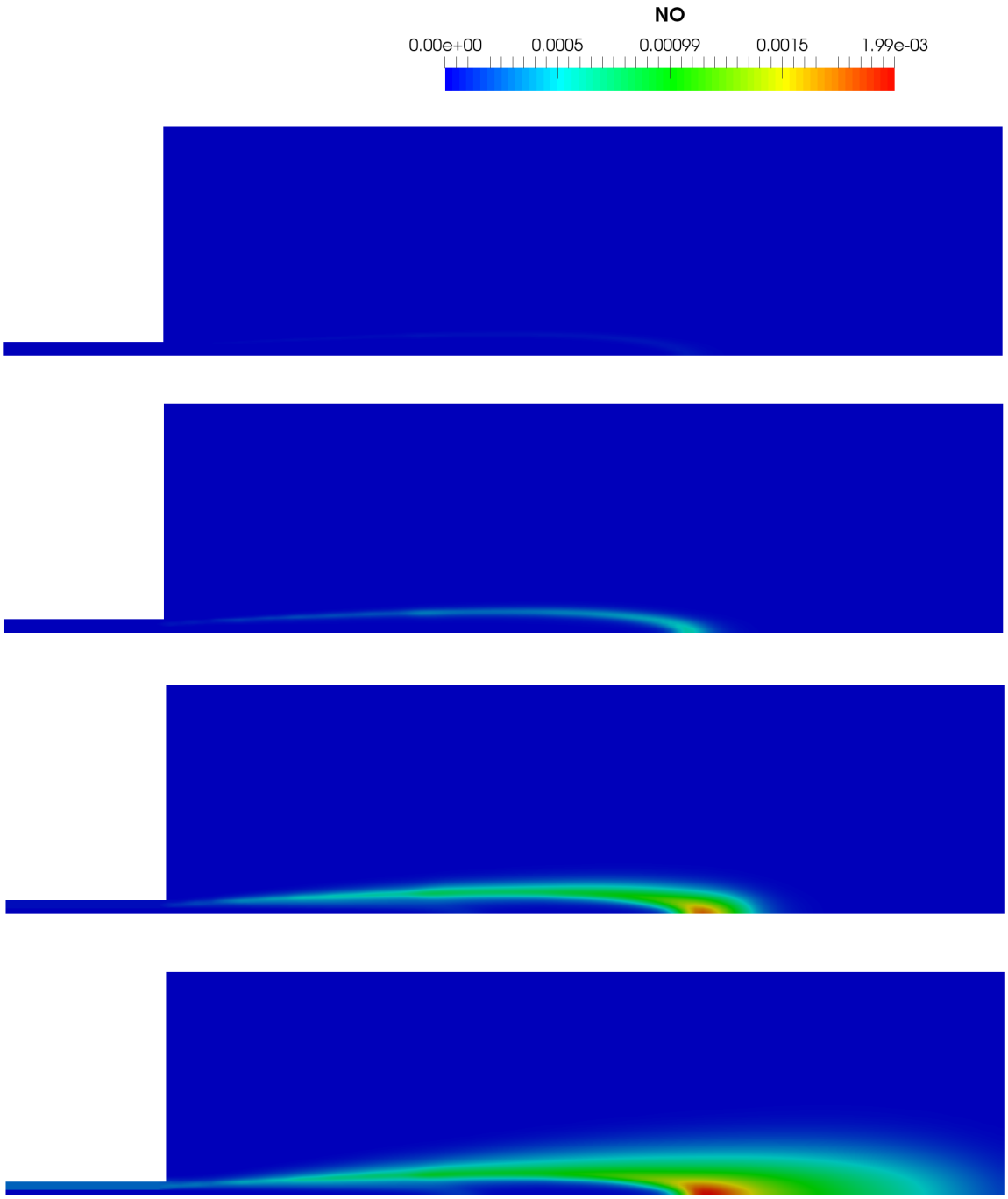

Figure 5.6.13: Mass fraction of species NO after (from top to bottom): 1, 10, 100 and 1000 iterations.

Several approaches are used to model NO emissions:

- **the one-step chemistry approach** uses the temperature field and species concentration fields for N_2 and O_2 calculated from the one-step reaction mechanism. Concentrations of O and OH are calculated using Equation (3.1.6) and 3.1.7 respectively. The extended Zeldovich mechanism is then applied to the respective fields.
- **the four-step chemistry approach** uses the same procedure as the one-step chemistry approach but with the N_2 and O_2 concentrations calculated using the four-step mechanism.
- **the complex chemistry approach** where the concentration of NO is calculated by the complex reaction mechanism.
- **the inherited complex chemistry approach** where the temperature field and species concentration fields for N_2, O_2, O and OH are calculated using the complex chemistry mechanism. The extended Zeldovich mechanism is then applied to the respective fields.
- **the new complex chemistry approach** where the temperature field and species concentration fields of N_2 and O_2 are calculated using the complex chemistry mechanism. The species concentrations of O and OH are calculated using Equation (3.1.6) and 3.1.7. The extended Zeldovich mechanism is then applied to the resulting fields.

The complex chemistry model calculates concentrations of NO_2 and N_2O. These species are similar to NO and considered to be NOx emissions. These species will be scaled by molar mass and added to the graphs to more accurately represent NOx emissions of the complex chemistry model. As NO_2 and N_2O emissions are produced at lower flame temperatures, they will only be included in regions where the flame has been developed. The NO concentration will be examined in three regions: near the burner exit, mid flame and developed flame.

NO concentration near the burner exit

The comparison between NO concentration calculated using different approaches and the experimental results is shown in Figure 5.6.14. In the near burner region, the flame has not fully developed and shows sharp gradients in concentration. Interestingly, the complex chemistry mechanism calculates a significantly lower concentration of NO than the experimental results. A part of NO production is instead produced into other species such as NO_2 and N_2O; however, the NOx concentration is practically identical to the NO concentration. From the complex chemistry data set, the new complex chemistry approach yields the best results, but still underestimates the concentration by about 50% at peak concentration. The one-step and four-step approaches match the experimental results fairly well.

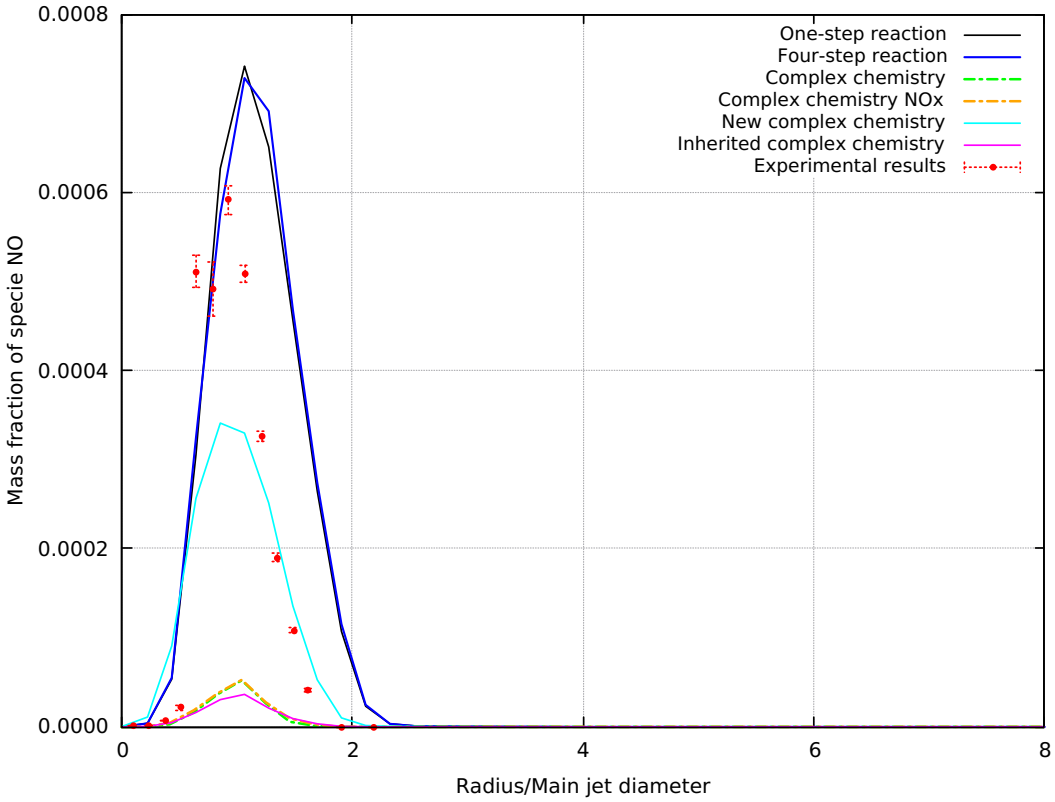

Figure 5.6.14: Mass fraction of specie NO at axial distance x/d= 3.

NO concentration mid flame

Figure 5.6.15 shows that none of the approaches are able to accurately predict the NO concentration. Complex chemistry approach performed the worst, with the new complex chemistry approach once again giving the best results. Both the one-step and four-step approaches provide a better match to the experimental results, but still underpredicted the peak NO concentration. However, the reduced mechanisms indicate a higher NO concentration further away from the flame, better matching the integral NO concentration in the domain.

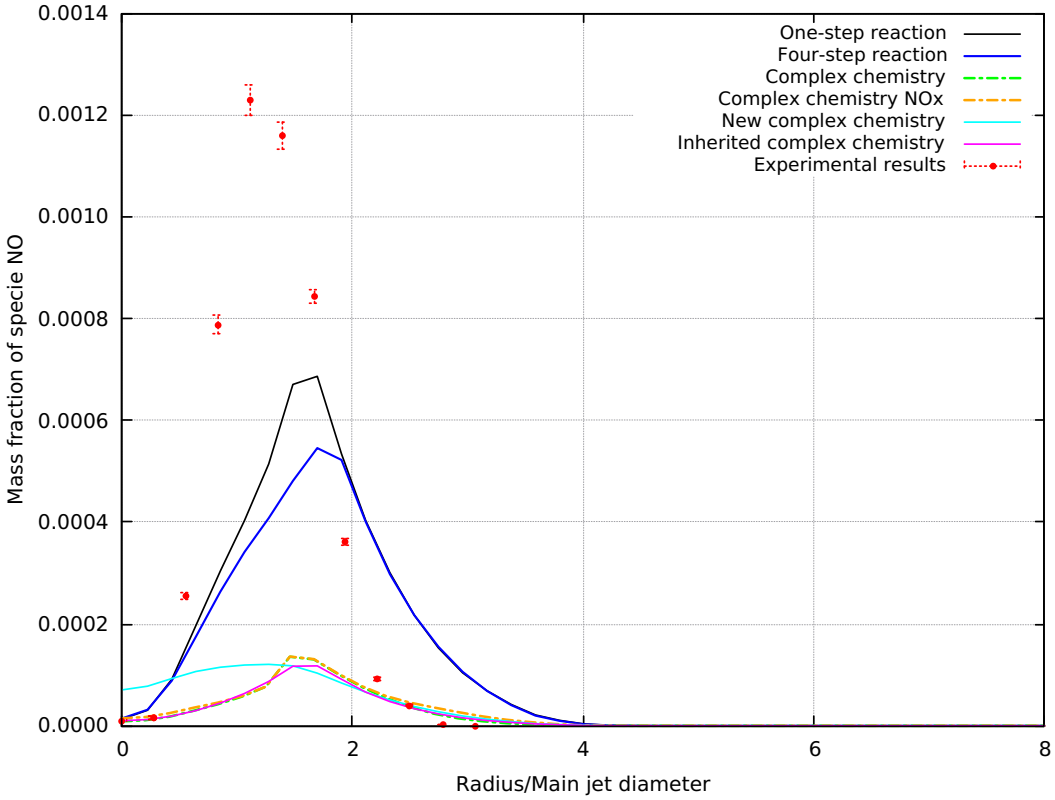

Figure 5.6.15: Mass fraction of specie NO at axial distance x/d= 15.

Figure 5.6.16 shows the NO concentration further downstream, at x/d= 30. The four-step chemistry approach is the only approach able to capture higher concentrations of NO near the axis of symmetry. In contrast to previous results, of all the complex chemistry approaches the inherited approach shows the most accurate results.

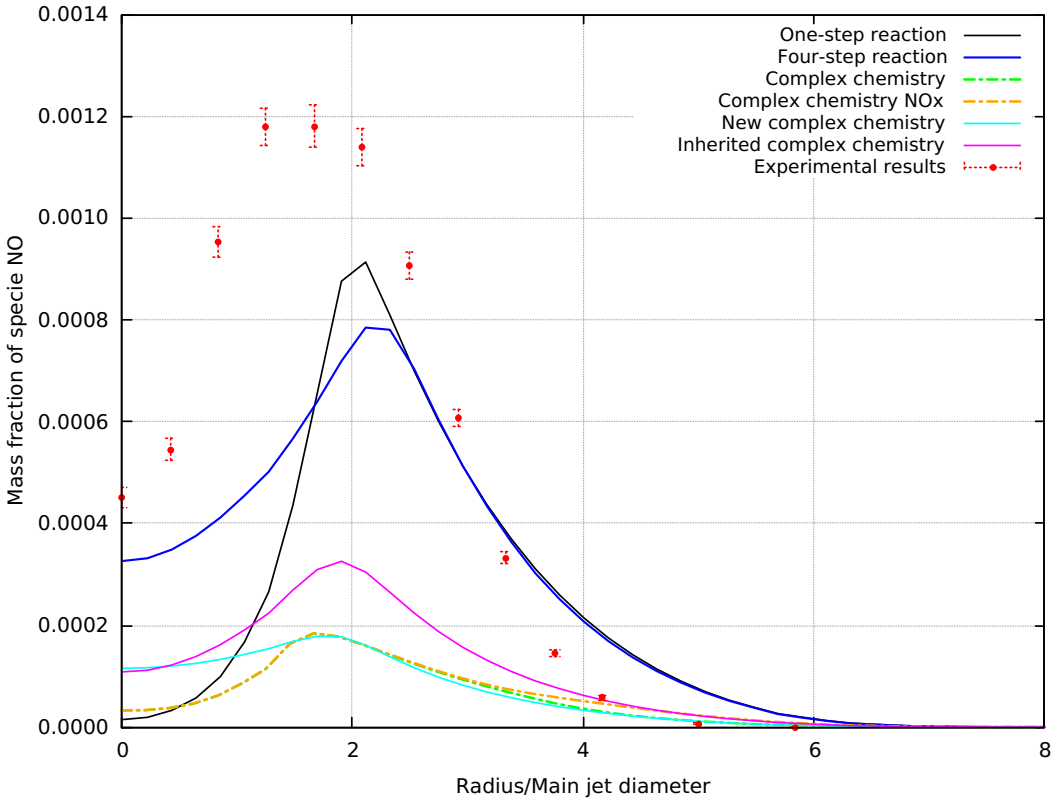

Figure 5.6.16: Mass fraction of specie NO at axial distance x/d= 30.

NO concentration in the developed flame

Figure 5.6.17 shows the comparison of the NO concentration in the developed flame (x/d=45). The complex chemistry approach severely under-predicted the concentration of NO. A small increase in NOx species concentrations can be seen in the region further away form the flame. Still, the complex chemistry is not able to accurately predict NO emissions. Both the inherited and new complex chemistry approach are able to better predict results. Once more, the one-step and four-step chemistry approaches are the best match, with the one-step chemistry approach unable to accurately predict the higher concentration near the axis of symmetry. None of the approaches were able to accurately predict NO concentration at x/d= 60, as seen in Figure 5.6.18. The reduced mechanisms indicated a higher concentration of NO, while the concentration calculated from the approaches derived from complex chemistry is too low.

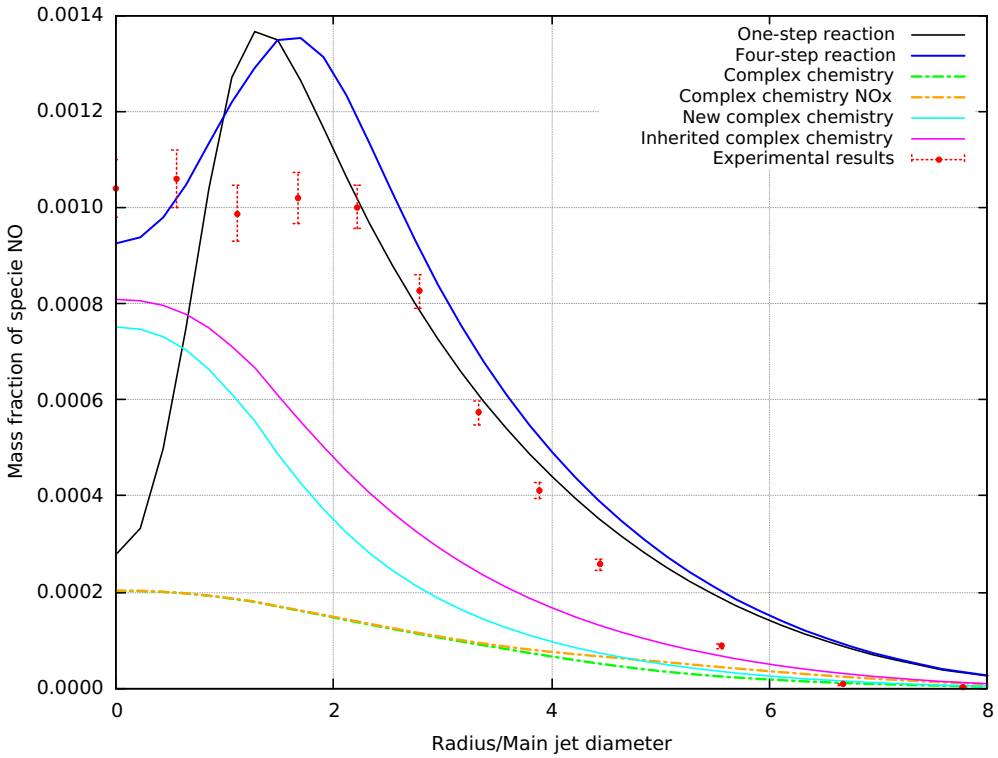

Figure 5.6.17: Mass fraction of specie NO at axial distance x/d= 45.

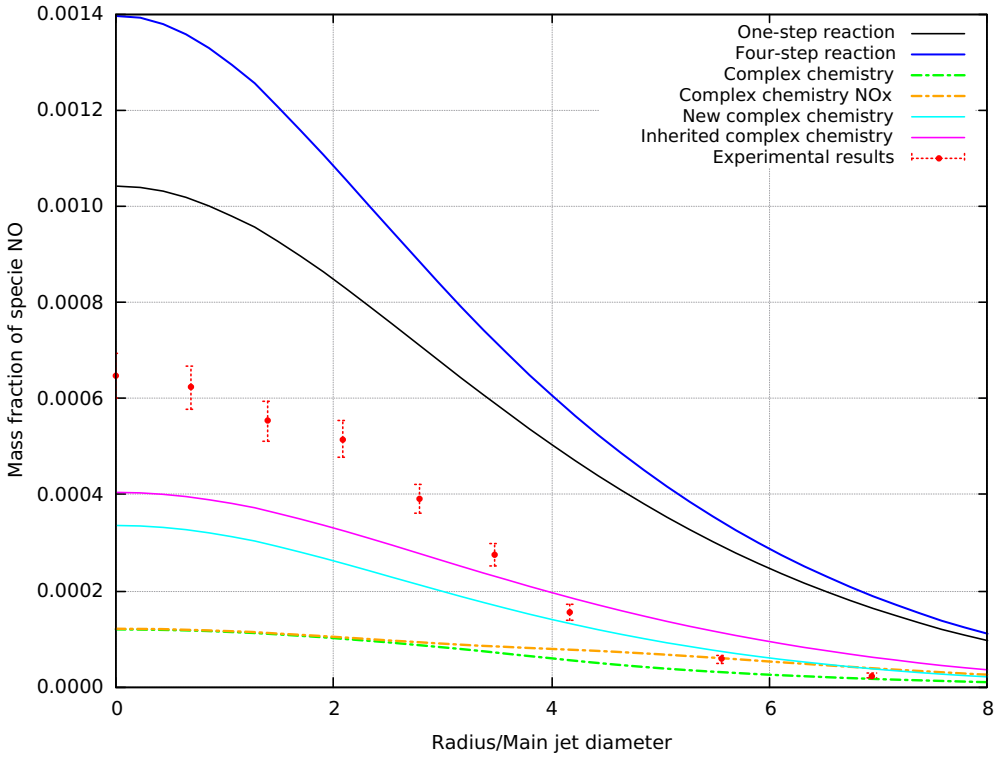

Figure 5.6.18: Mass fraction of specie NO at axial distance x/d= 60.

5.7 Conclusion

The Sandia Flame D test case is used to validate the PaSR model (Section 2.4.3) and the extended Zeldovich mechanism (Section 3.1). Simulations are performed using the PaSR combustion model and k-ε turbulence model on a three-dimensional and two-dimensional mesh. The results obtained using both computational are a good match to each other, indicating that three-dimensional effects have little effect on the results, assuming axi-symmetric boundary conditions are prescribed.

The results of numerical simulations using three different reaction mechanisms (of increasing complexity) are compared to experimental data. All reaction models are able to accurately model combustion, with minor differences in specie concentrations and temperatures. Generally speaking, the complex chemistry mechanism performed the best.

The extended Zeldovich mechanism is applied to numerical simulations with reaction mechanisms of varying complexity. Different implementations of the extended Zeldovich mechanism are compared to experimental data. The approaches based on the complex reaction mechanism are not able to correctly predict the NO concentration. This is most likely because the complex reaction mechanism includes endothermic pollutant forming reactions, which are not present in reduced mechanisms. The reduction in flame temperature has a negative impact on NOx formation. In conclusion, the extended Zeldovich mechanism performs best when paired with reduced reaction mechanisms.

Chapter 6

Rolls Royce Tay Combustion Chamber

In this chapter, the PaSR model validated in Chapter 5 is used to simulate combustion in the Rolls Royce Tay combustion chamber. The Rolls Royce Tay engine is introduced in Section 6.1, and previous experimental work is listed. In Section 6.2, the geometry of the combustion chamber is presented, as well as the unstructured three-dimensional mesh used in the numerical simulations.

Experimental boundary conditions are explained and discussed in Section 6.3, including two flow configurations used in this thesis. The numerical boundary conditions are derived and listed. The implementation of new boundary conditions in OpenFOAM is explained.

A two-step propane reaction mechanism is derived in Section 6.4, along with the reaction coefficients. Simulation settings and the solving procedure, which involves multiple steps, is presented in Section 6.5.

The results of the numerical simulations are presented in Section 6.6. A total four cases are presented, a non-combusting transient case, an ”ignition by fuel” combusting case, and two cases with different flow configurations. The results of the extended Zeldovich mechanism are presented and discussed.

6.1 Rolls Royce Tay Engine

The Rolls Royce (RR) Tay is a two-shaft medium-bypass ratio engine derived from the Trent large engine family. Since entering service in 1988, over 2000 Tay engines have been installed worldwide, logging over 11 million flight hours [5]. The Tay family of engines is used on large business jets and smaller airliners, including the Gulfstream IV, Fokker $70/100$ and Boeing $727-100$. As shown in Figure 6.1.1, the RR Tay elements are (starting from the left): the fan, a three-stage low pressure (LP) compressor, a 12-stage high pressure (HP) compressor, combustion system, two stage HP turbine, and a three-stage LP turbine.

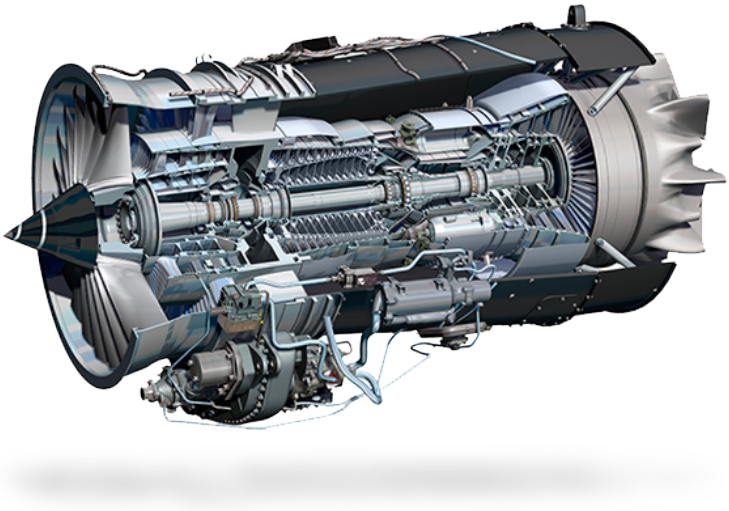

Figure 6.1.1: Rolls Royce Tay cutaway. [5]

The combustion system consists of 10 tubo-annular combustion chambers as shown in Figure 6.1.2. The combustion system was derived from the reliable RR Spray engine family. The distinct advantage of the tube annular design is the ability to more easily test and develop a combustion chamber. However, this comes with the cost of a high surface area to volume ratio, which requires more cooling. Increased cooling was achieved using a proprietary material called Transply. "Transply is produced by brazing together two laminates of a high temperature nickel alloy containing an interrelated pattern of holes and channels, produced by electrochemical machining. This provides an advanced cooling configuration in sheet form with an overall thickness typical of current combustor materials." [6]

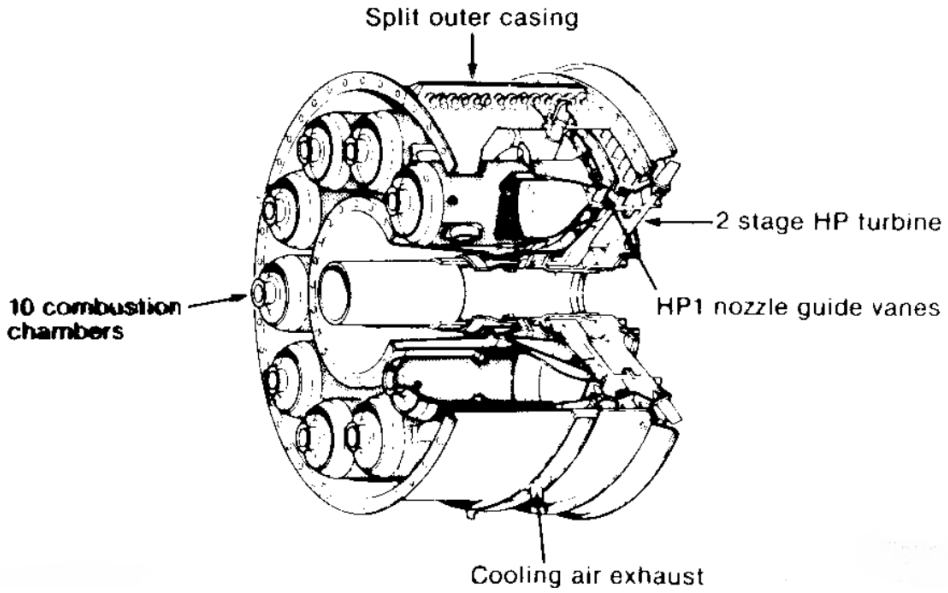

Figure 6.1.2: Rolls Royce Tay combustion system. [6]

Several numerical investigations were performed on a model RR Tay combustor at Imperial Collage. Water experiments were performed by Parma [1] and Parma and McGuirk [19] to determine the flow characteristics inside the combustor. The influence of the swirler on the flow was investigated by Koutmos [20]. Combustion experiments were conducted by Tse [17]. Temperatures were measured using bare-wire thermocouples and concentrations of unburnt hydrocarbons (UHC), CO_2, CO, O_2 and H_2 by sampling using water cooled probes and gas analyzers.

6.2 Computational Domain

Available experimental data for the RR Tay combustor is based on a model geometry. The model combustor consists of a hemispherical head containing the swirler and 10 injector holes of 1.7 mm diameter. The head is connected to a 75 mm diameter cylinder containing two sets of holes, six primary holes of 10 mm diameter and six dilution holes of 20 mm diameter. The dilution holes are rotated 30 degrees in respect to the primary holes. The circular-to-rectangular nozzle geometry was kindly provided by Dr. Kevin Menzies. Figure 6.2.1 shows the model RR Tay geometry with its respective dimensions.

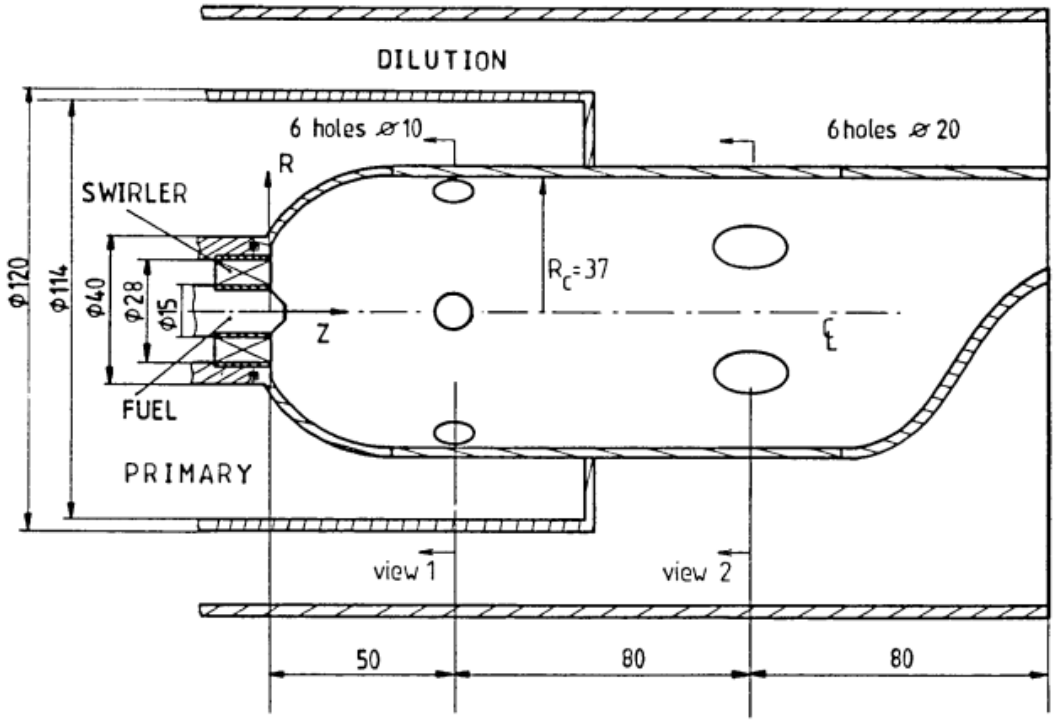

Figure 6.2.1: Rolls Royce Tay model combustion chamber geometry.

Generally speaking, structured meshes exhibit increased numerical stability and are advisable in complex flows. However, creating a structured mesh inside complex geometries can be a cumbersome task that requires a lot of time and effort. Significant time savings can be achieved by using an automated meshing procedure. Using T-Rex [54] (anisotropic tetrahedral extrusion), an automated hybrid mesh generation method, the computational mesh in Figure 6.2.2 was created.

A structured, one cell thick, cell set was extruded from the combustor geometry in order to correctly apply the required wall functions. The total size of the unstructured mesh is 1.15 million cells, of which 95% are tetrahedra and the remainder are prisms. Maximum mesh non-orthogonality is 64.3, with an average of 18.9. Figure 6.2.3 shows the cross section of the structured mesh. The edge color represents the edge length, with blue being the smallest and red the largest.

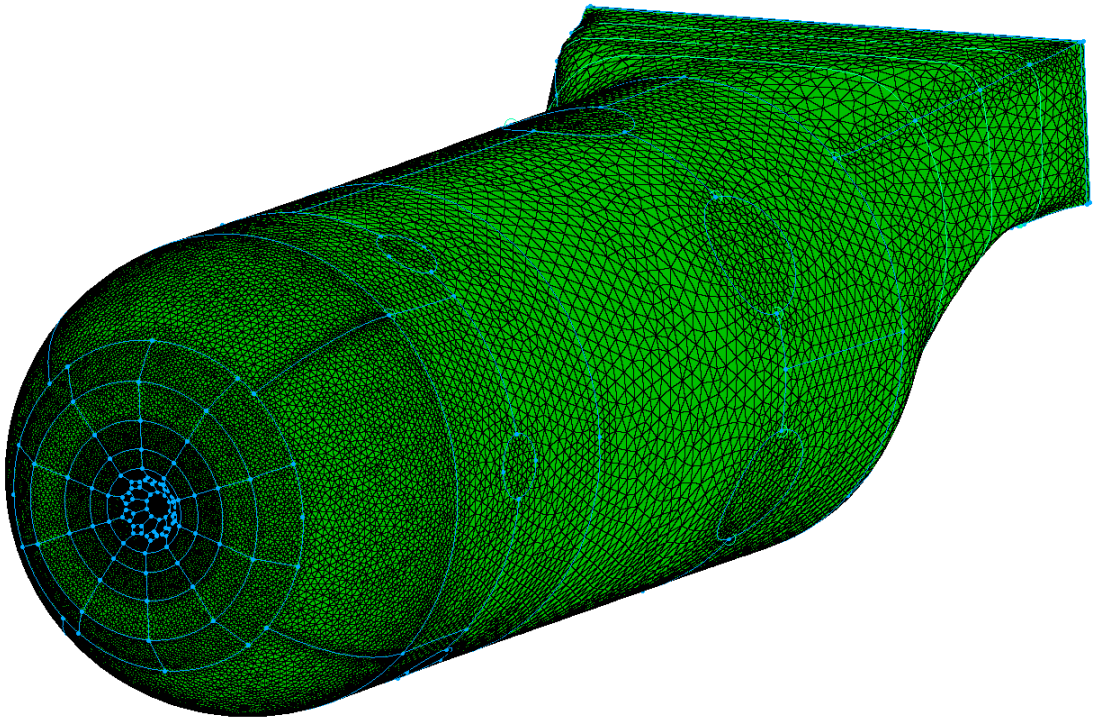

Figure 6.2.2: Rolls Royce Tay model combustion chamber surface mesh.

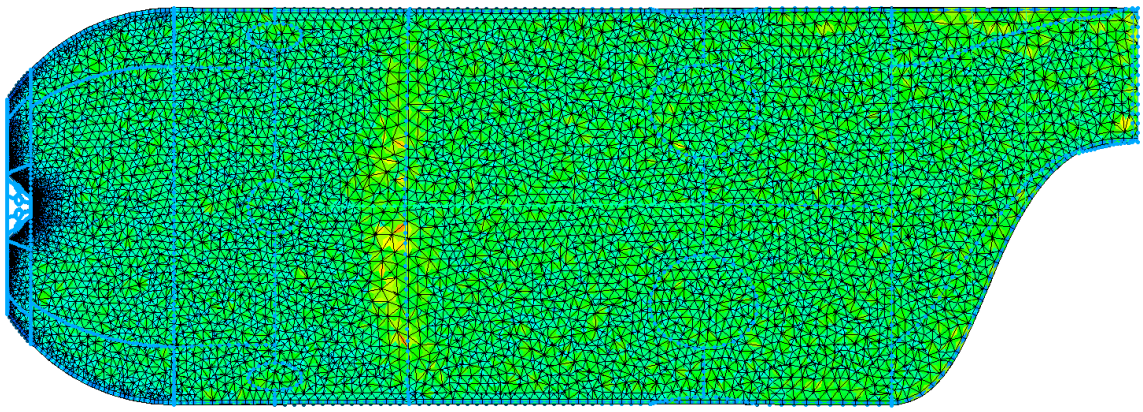

Figure 6.2.3: Cross section of the computational domain, coloured by edge length.

6.3 Boundary Conditions

As mentioned in Section 1.3, experimental data is available for two flight conditions. Experiments are conducted with conditions matching take off and ground-idle conditions [2]. In this thesis, a numerical investigation is conducted on the flow configuration matching take off conditions with an air/fuel ratio (AFR) of 57. In combusting experiments, the model RR Tay engine outer walls are made of Transply, a porous material. However, the water test are conducted using a solid plexiglass wall. To determine the flow with and without porous walls, several flow splits are available as seen in Figure 6.3.1.

The flow splits are expressed as a percentage of the total air mass flow $\dot{m}$. Figure 6.3.1.a represents the flow split in the real combustor. Combusting experiments by Tse [17] use the flow split as shown in Figure 6.3.1. The achieve these flow splits, modelling the Transply walls is required. The flow split in Figure 6.3.1.c was used by Koutmos [20] in water tests. Palma [1] suggest the used of the flow split in Figure 6.3.1.d to replicate the combustion flow with solid walls. The effect of Transply is neglected in this thesis, and solid walls are assumed. Therefore, the flow configurations suggested by Koutmos and Palma will be used in this thesis. The flow split information is shown in Table 6.3.1.

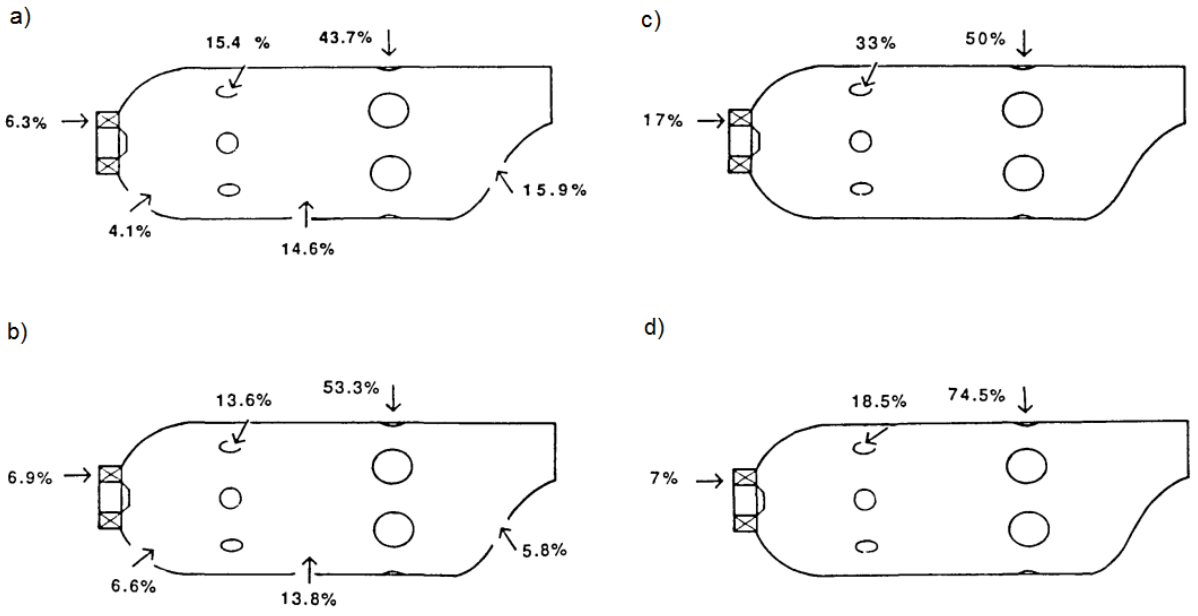

Figure 6.3.1: Suggested flow splits. [1]

Previous studies [19] [20] explored the influence of the swirler on the flow characteristics. As suggested in McGuirk and Palma [19], the swirler is assumed to be uniform but the swirl area is reduced by 41% (by increasing the cap area) to account for the area of the guide vanes. Additionally, previous papers suggest that a gaseous fuel consisting of 95% propane is injected into the combustor through 10 injector holes, with the remaining 5% unspecified. Since the chemical composition of the remaining 5% of mass flow is not known, it is assumed to be negligible and a flow of pure propane is assumed.

Flow conf.	Swirler VA	AFR	$\dot{m}$[1]	$\dot{m}_f$[1]	Swirler FS[2]	Primary FS[2]	Dilution FS[2]
1	45	57	0.1	$1.76 \cdot 10^{-3}$	17	33	50
2	45	57	0.1	$1.76 \cdot 10^{-3}$	7	18.5	74.5

VA - Vane angle [1] Mass flow expressed in grams per second

FS - Flow split [2] Flow split expressed as a percentage of total flow $\dot{m}$

Table 6.3.1: Rolls-Royce Tay flow configurations.

Inlet fuel temperature is stated to be 315 K. The velocity direction of the primary and dilution hole inlets is assumed to be normal to the hole surface. Air consisting of 79% nitrogen and 21% oxygen at 315 K enters the combustor through the swirler, primary and dilution holes. Figure 6.3.2 shows the boundary patches of the RR Tay combustor. Starting from the left, injector holes are coloured in red, inner swirler (with an area of 41% of the total swirler area) in yellow, outer swirler in blue, primary holes in orange and dilution holes in pink. The gray surfaces are the walls of the combustor, with the outlet not visible (rectangular area on the top right part of the combustor). The numerical boundary conditions for flow configuration 1 are specified in Table 6.3.2.

The velocity boundary conditions are set using *zeroGradient* at the inlet and *surfaceNormalFixedValue* at the injector, primary holes and dilution holes. *SurfaceNormalFixedValue* uses the face normal to determine the velocity vector direction, with the magnitude set by the user. The specified numbers are negative because the face normal points outwards. A new boundary con-

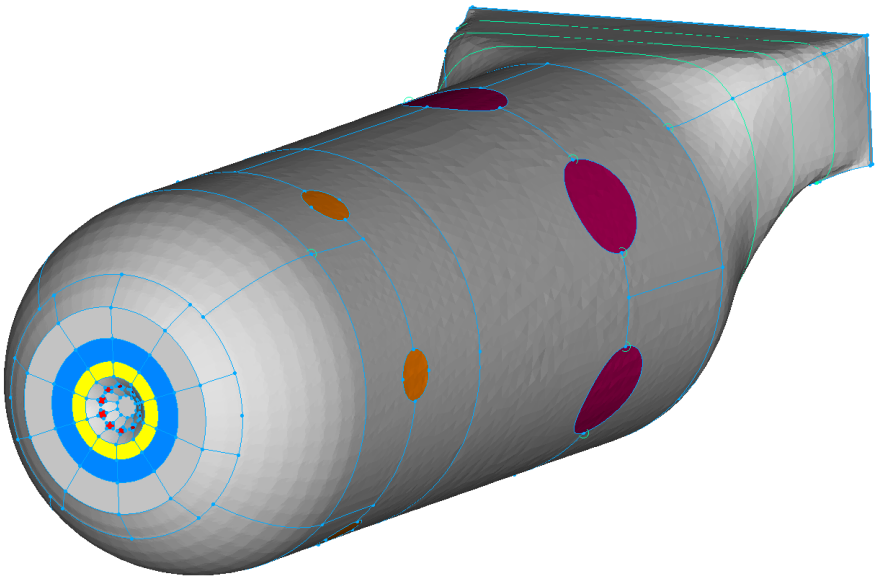

Figure 6.3.2: Rolls Royce Tay boundary conditions.

dition *swirlStatorFlowRateInletVelocitySetCenter* is specified based on the *swirlFlowRateInletVelocity* BC, allowing the user to set the axis of rotation manually, instead of calculating it using the patch face normals.

The pressure is set to a Neumann boundary condition at all patches, except the outlet. The boundary condition *totalPressureOutlet* is derived from the *totalPressure* boundary conditions, allowing it to be used on outlets. At each boundary cell, the pressure is calculated using the following formula:

$$p = p_0 - 0.5\rho|u|^2. \tag{6.3.1}$$

	Velocity	Pressure	k	ε	μ_t	α_t
swirler	SSFRIVSC (0.014873)	zG	TIKEI (0.064)	TMLDRI (0.0065)	*calc*	*calc*
injectorHoles	SNFV (-46.66)	zG	TIKEI (0.10)	TMLDRI (0.0017)	*calc*	*calc*
primaryHoles	SNFV (-60.93)	zG	TIKEI (0.176)	TMLDRI (0.01)	*calc*	*calc*
dilutionHoles	SNFV (-23.14)	zG	TIKEI (0.141)	TMLDRI (0.02)	*calc*	*calc*
walls	fV(0 0 0)	zG	*kqRWF*	*epsilonWF*	*mutWF*	*alphatWF*
outlet	zG	TPO	IO	IO	*calc*	*calc*

fV - fixedValue zG - zeroGradient SNFV - surfaceNormalFixedValue
TPO - totalPressureOutlet SSFRIVSC - swirlStatorFlowRateInletVelocitySetCenter
TIKEI - turbulentIntensityKineticEnergyInlet *kqRWF - kqRWallFunction* *epsilonWF - epsilonWallFunction* *mutWF - mutWallFunction* *alphatWF - alphatWallFunction*

Table 6.3.2: Rolls-Royce Tay boundary conditions.

Boundary conditions for turbulent kinetic energy k and turbulent dissipation rate ε are the same as in the Sandia Flame D (Section 5.3), with the exception of the outlet boundary condition. The *inletOutlet* boundary condition is used, prescribing a Neumann BC in case of outflow, or a Dirichlet BC (to a small value such as 0.001) in case of inflow. Turbulent thermal diffusivity α_t and turbulent dynamic viscosity μ_t are calculated using the procedure described in Section 5.3.

6.4 Reaction Mechanism

In Chapter 5, it was concluded that reduced mechanisms are able to predict main flow characteristics with a large reduction in computational time. There are limited reaction mechanisms for C3 hydrocarbons such as propane (C_3H_8). GRI-Mech 3.0 [15] has several reactions describing the combustion of propane; however, the mechanism is primarily intended to be used for methane combustion. The reaction mechanism selected for this thesis is a two reaction mechanism described by Nguyen and Ying [21]. The reaction mechanism calculates CO_2 and CO concentrations, so using it along with the extended Zeldovich mechanism allows us to calculate calculating the emissions of several major pollutants. The chemical reactions are:

$$C_3H_8 + 3.5\,O_2 \rightarrow 3\,CO + 4\,H_2O\,, \tag{6.4.1}$$

$$CO + 0.5\,O_2 + M_B \underset{b}{\overset{f}{\rightleftharpoons}} CO_2. \tag{6.4.2}$$

where M_B is the third body that does not participate in the reaction but has an influence on the reaction rate. In the case of the oxidation of carbon monoxide, the third body is water (H_2O). The reaction coefficients are listed in Table 6.4.1

Reaction	a	b	c	r	$A_f\,[(m^3/kmol)^{r-1}s^{-1}]$	$\beta_j\,[-]$	$T_j\,[K]$
reaction 6.4.1	0.1	1.65	0	1.75	$5.623 \cdot 10^{10}$	0	15095
reaction 6.4.2 f	1	0.25	0.5	1.25	$7.079 \cdot 10^{10}$	0	20128
reaction 6.4.2 b	1	0	0	1	$5 \cdot 10^{8}$	0	20128

Table 6.4.1: Two-step propane combustion reaction coefficients.

6.5 Simulation Settings

Before conducting numerical simulations, mesh renumbering is executed using the command *renumberMesh* to reduce matrix bandwidth and speed up computation. The computational domain is deconstructed along the x-axis into four subdomains and the simulations are run in parallel. The solution prodecure is as follows:

- compute the initial flow field using *simpleFoam*, a steady-state solver for incompressible flows,
- use the results of the steady-state simulation as initial values for the compressible reacting solver *reactingFoam* without chemical reactions or combustion,
- use the results of the transient simulation as initial results for a simulation where chemical reactions are enabled. Combustion is initialized by setting the inlet fuel temperature to 2000 K. The simulation is performed until combustion starts (indicated by an increase in temperature)
- the inlet fuel temperature is set back to 315 K and the simulation is run until $t = 0.02$ s, the fuel residence time.

The numerical and chemistry settings listed in Table 6.5.1 are used for the combusting simulations. Since an unstructured mesh was used, a non-orthogonal corrector is added. The ODE solver used is Runge Kutta (RK). Since N_2 does not participate in any chemical reactions, as per the reaction mechanism, it is set as the inert species.

PIMPLE	nOuterCorrectors	2
	nCorrectors	2
	nNonOrthogonalCorrectors	1
solvers	p	amgSolver
	hs|k|epsilon|Yi	BiCGStab
schemes	ddtSchemes	Euler
	gradSchemes	cellLimited leastSquares 1
	divSchemes	Gauss upwind
	laplacianSchemes	Gauss linear corrected
	interpolationSchemes	linear
	snGradSchemes	limited 0.5
chemistry	inertSpecie	N2
chemistrySolver	RK	eps = 5e-4
	Cmix	0.1 - 0.3
	initialChemicalTimestep	1e-6

Table 6.5.1: Numerical settings for the Rolls-Royce Tay test case.

6.6 Results

The results using different flow configurations and flow splits are presented in this section. These include the transient case without chemical reactions, the ignited case where the fuel temperature is left at 2000 K, and cases matching flow configurations 1 and 2 from Table 6.3.1.

6.6.1 Non-combusting Transient Case

The transient case is used to calculate the initial values for the combusting case. However, examining the results from this non-combusting case gives an insight into the flow in the combustion chamber. Figure 6.6.1 shows the flow inside the combustion chamber at the mid-vertical plane. Streamlines are used to visualize the flow field, with the color indicating the axial velocity. The flow field shows no significant difference from the experimental results, with two recirculation zones appearing. Recirculation zone A is the main recirculation zone where the

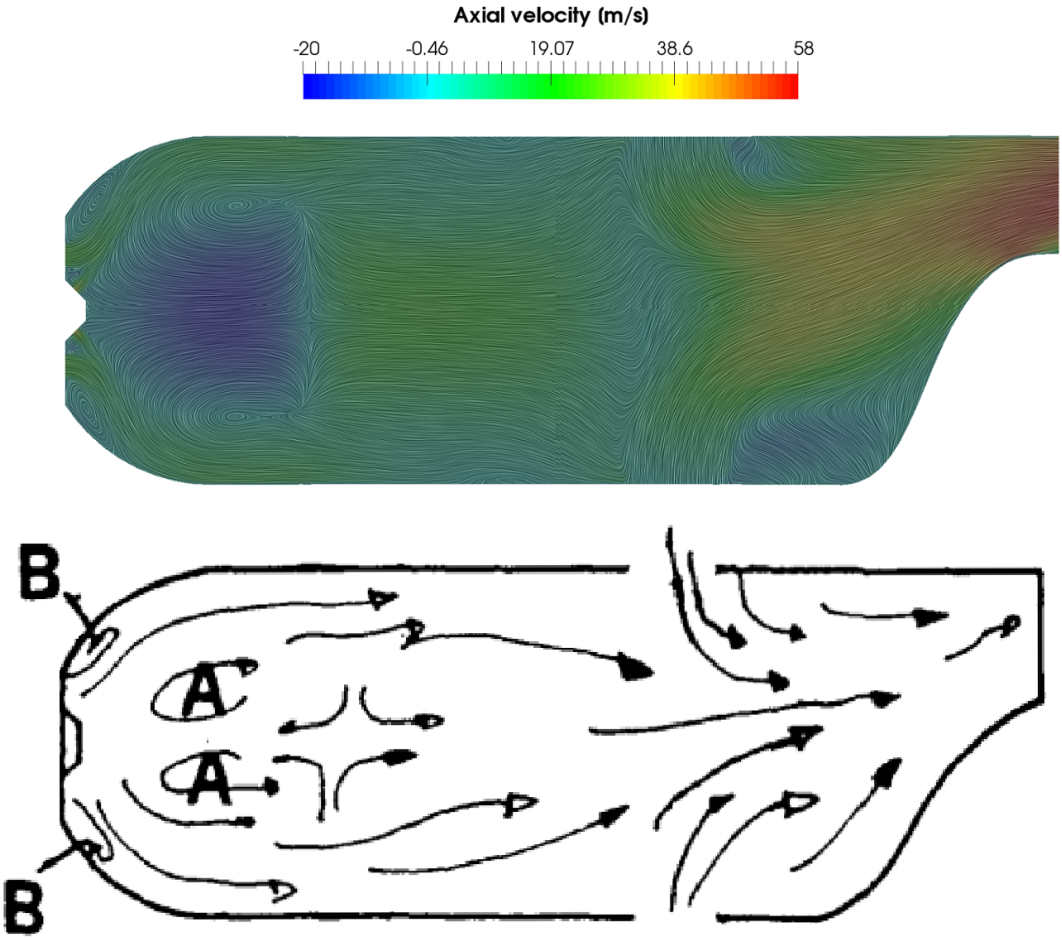

Figure 6.6.1: Recirculation zones inside the Rolls-Royce Tay combustor [1].

flame front is located in the combusting case. Also visible is the secondary, much smaller, recirculation zone B.

The shape and effect of the recirculation zone can be seen in Figure 6.6.2. The source of the the streamlines are the injector holes. The rotation of the streamlines upwind from the main recirculation zone is caused by the swirler. The streamlines are coloured by their axial velocity. By tracing streamlines directly from the injection holes, the primary task of the main recirculation zone becomes apparent. Its intended purpose is to provide additional mixing of fuel and air in an area with reduced velocity, thus providing good conditions for a stable flame front. The mixing of fuel can be better seen in Figure 6.6.3, where the streamlines are coloured according to the mass fraction of methane.

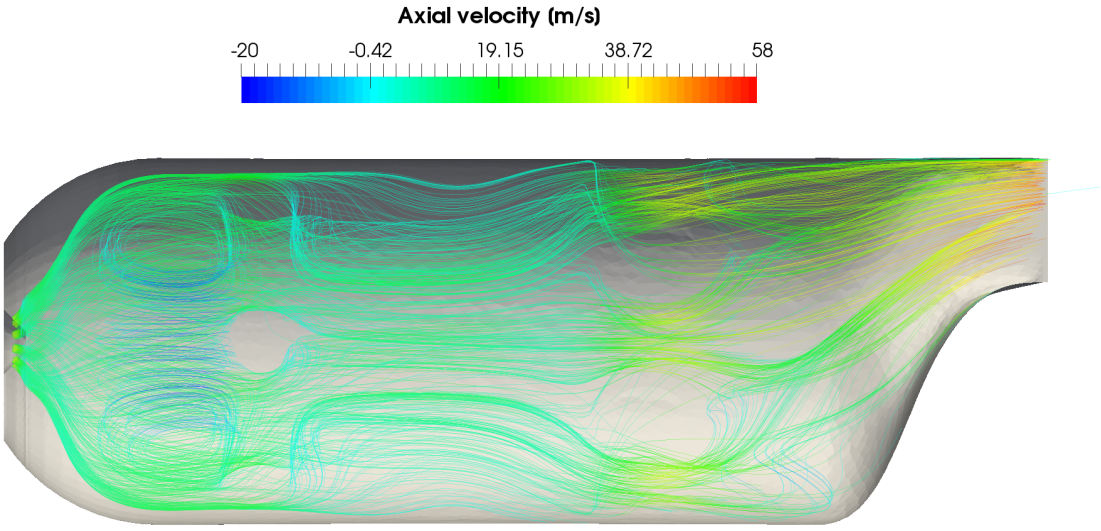

Figure 6.6.2: Visualization of the flow inside the Rolls-Royce Tay combustion chamber using streamlines.

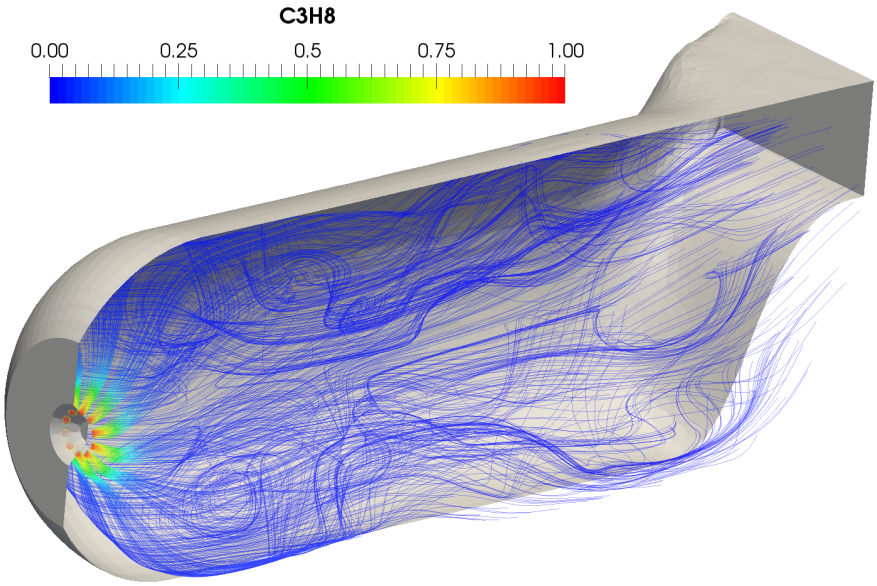

Figure 6.6.3: The effect of the main recirculation zone on fuel concentration.

6.6.2 Ignition by Fuel

After convergence was achieved in the transient case, ignition was initiated by increasing the fuel temperature to 2000 K. Fuel gasses had sufficient energy as soon as they entered the domain through the injector holes, and ignited after coming into contact with oxygen, resulting in a flame front as seen in Figure 6.6.4. The flame front is stable and remains at the same location for the entire simulation time. In Chapter 2, the effects of combustion on fuel flow were described.

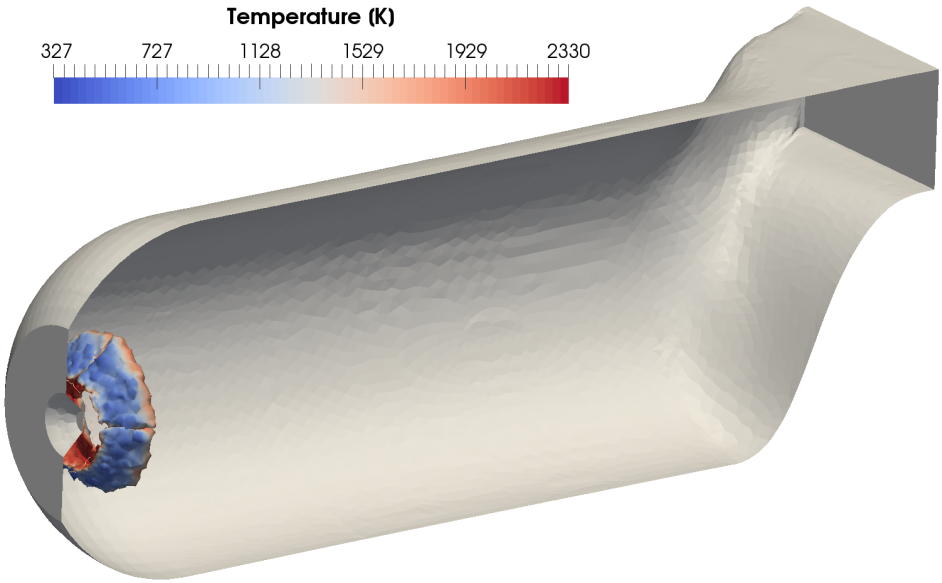

Figure 6.6.4: Flame front ignited by high temperature fuel.

One of these effects, a pressure wave, can be seen in Figure 6.6.5. The pressure wave caused by the sudden increase of temperature after the combustion starts. Each frame represents a time increment of 10^{-4} seconds. The pressure field after wave dissipation can be seen in Figure 6.6.6.

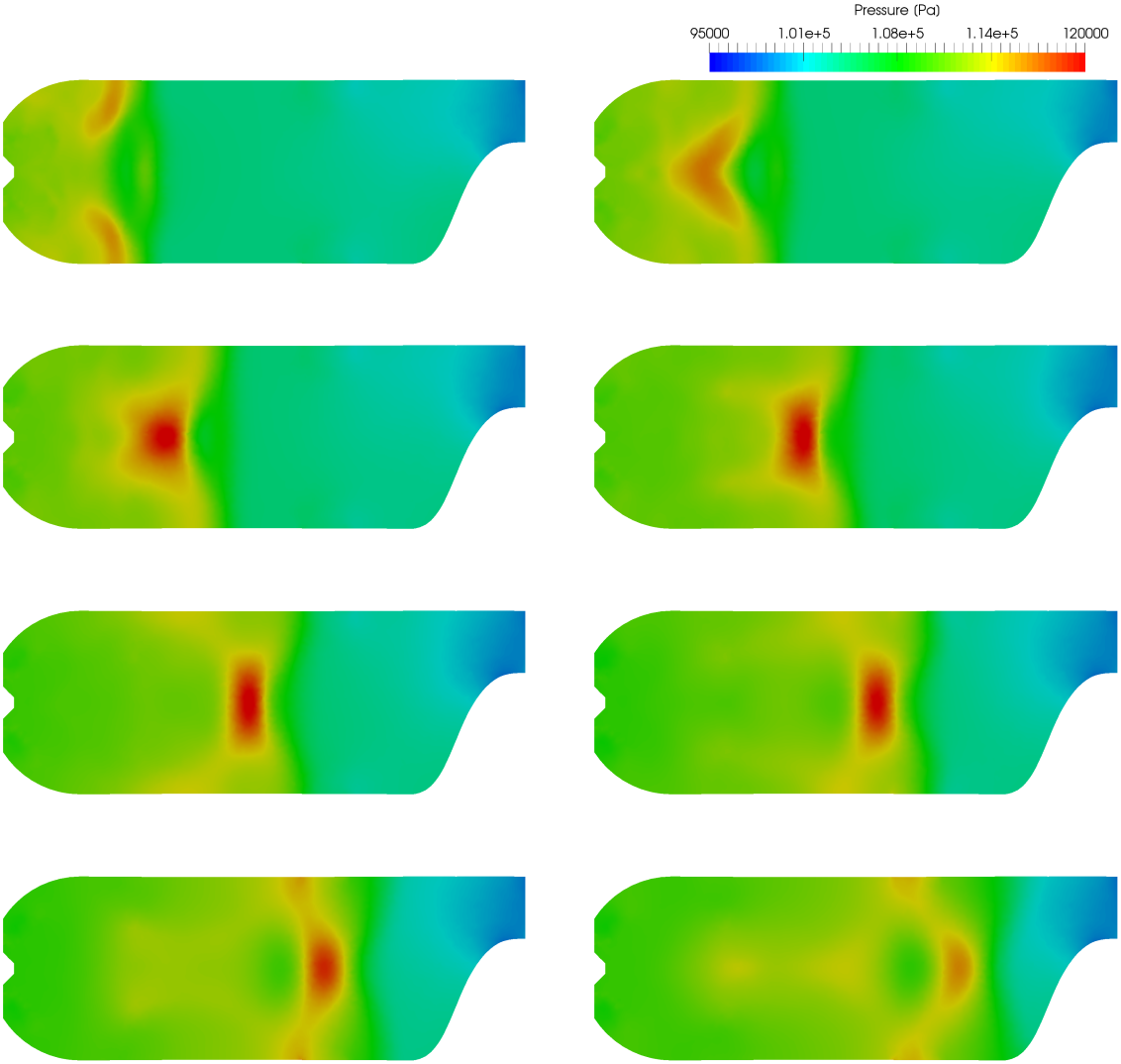

Figure 6.6.5: Expansion of the pressure wave caused by combustion.

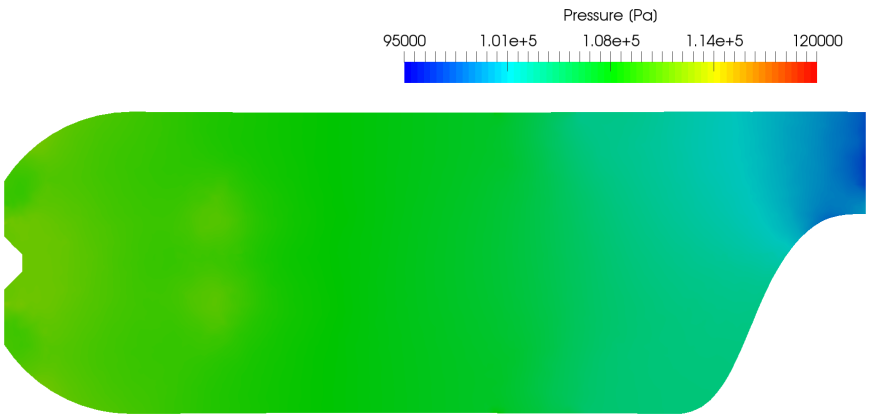

Figure 6.6.6: Pressure field after pressure wave dissipation.

6.6.3 Combustion Case Flow Configuration 1

Once the combustion is initiated, and results reached a quasi-steady state, the results from the case described in Section 6.6.2 are used for the initial values in this case. The only thing that was changed was the inlet fuel temperature, which was reduced to the value specified in the experiments (315 K). As listed in Table 6.3.1, flow configuration 1 was used in the model experiments to reproduce the combusting flow field in a model with solid walls. Compared to flow configuration 2, it has an increased flow through the swirler and primary holes. For reference, the combustor swirl split is 6.3% [1] in the actual Rolls Royce Tay engine. Figure 6.6.7 shows the flame development after fuel temperature was reduced to experimental values. Initially the flame front expands (b), however it soon starts to disperse (b, c). After the flame front is extinguished (d), ignition still occurs near the injector jets. Soon after, all sources of flame ignition are extinguished (e) and the flame front propagates downwind (f, g), until it is completely extinguished.

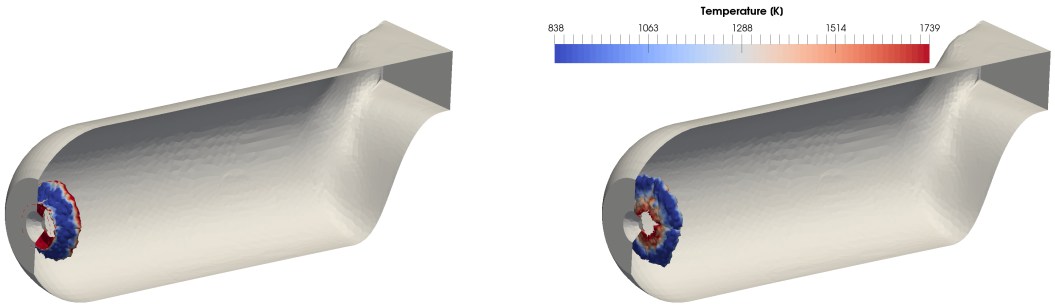

(a) $t = 2 \cdot 10^{-4}$ s

(b) $t = 6 \cdot 10^{-4}$ s

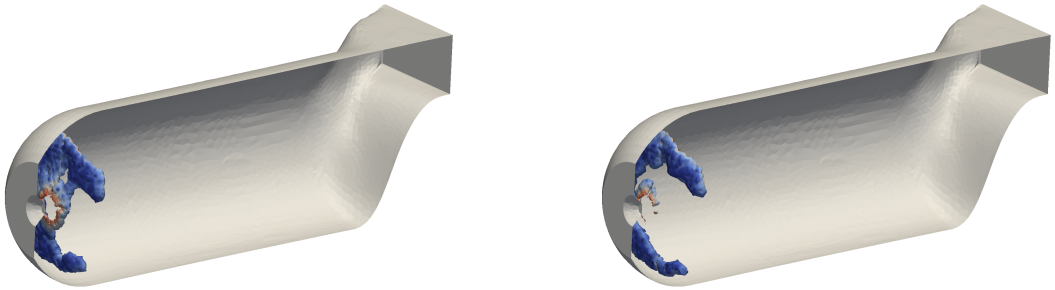

(c) $t = 8 \cdot 10^{-4}$ s

(d) $t = 9 \cdot 10^{-4}$ s

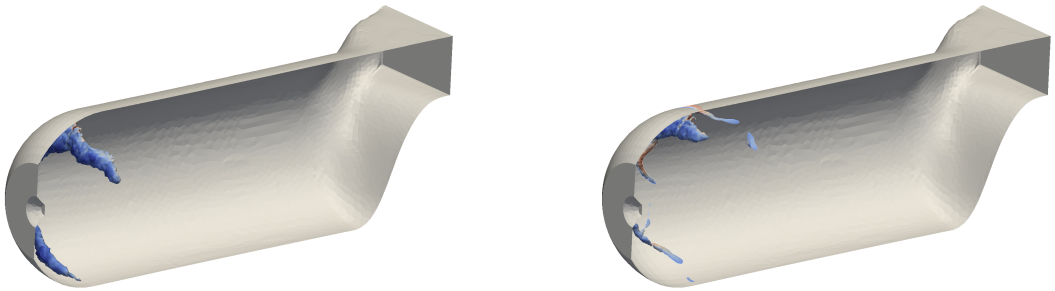

(e) $t = 12 \cdot 10^{-4}$ s

(f) $t = 16 \cdot 10^{-4}$ s

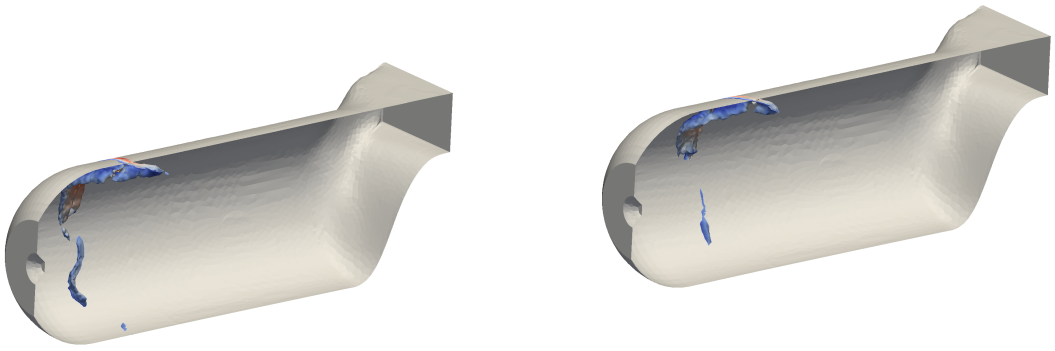

(g) $t = 21 \cdot 10^{-4}$ s

(h) $t = 28 \cdot 10^{-4}$ s

Figure 6.6.7: Flame propagation after removing the ignition source.

6.6.4 Combustion Case Flow Configuration 2

Flow configuration 2 is suggested by Palma [1] to more realistically describe the flow inside the combustion chamber while using solid walls. The flow information is listed in Table 6.3.1. This flow split more adequatelly described the flame front, as seen in Figure 6.6.8. After forced ignition was disable by reducting the fuel inlet temperature to 315 K, the flame front has a well defined shape (a). Three main ignition regions can be seen: the flame at the injectors, the primary and the secondary front. As the flow develops (b,c), the secondary flame front disappears, and the primary flame front intensifies and moves towards the fuel inlet. The flame at the injectors soon dissipates (d, e), and the primary flame front is distorted into a cone like shape by the flow. The primary flame front stays at a constant position, near the recirculation zone (f,g), however, the injector flame front is seen to move downstream and near the walls of the combustor. This behaviour is not intended, as a flame front near the wall increases the temperature of the walls to unmanageable levels. Additionally, a tertiary flame front develops downstream from the dilution holes.

The comparison of flow configuration 2 with experimental data is shown in Figures 6.6.9 and 6.6.9. The comparison of temperature in the mid-vertical plane is visible in Figure 6.6.10. Several observations can be made when comparing the simulation results to experimental data:

- the numerical simulation overpredicted the maximum temperature in the combustion chamber.
- the primary flame front, located in the recirculation zone, is not correctly captured by the numerical simulations, both by temperature and location. The recirculation zone only slightly affects the shape of the flame front,
- numerical simulations are able to capture the increased temperature region behind the primary holes, albeit on a smaller scale,
- the tertiary front developed behind the dilution holes can be seen in the numerical simulation temperature field, as well as the reduction in temperature caused by the dilution holes,

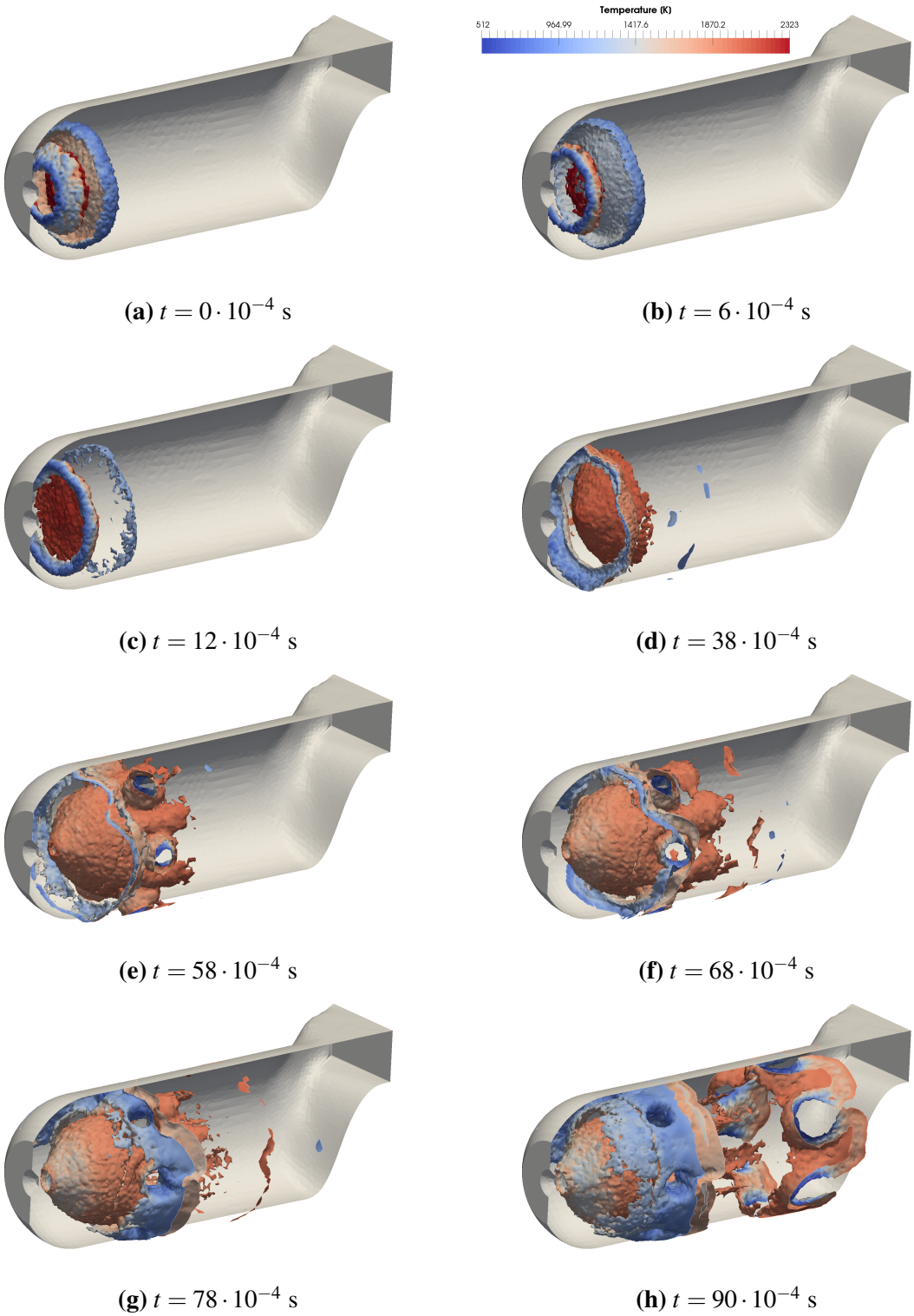

(a) $t = 0 \cdot 10^{-4}$ s **(b)** $t = 6 \cdot 10^{-4}$ s

(c) $t = 12 \cdot 10^{-4}$ s **(d)** $t = 38 \cdot 10^{-4}$ s

(e) $t = 58 \cdot 10^{-4}$ s **(f)** $t = 68 \cdot 10^{-4}$ s

(g) $t = 78 \cdot 10^{-4}$ s **(h)** $t = 90 \cdot 10^{-4}$ s

Figure 6.6.8: Flame propagation after removing the ignition source.

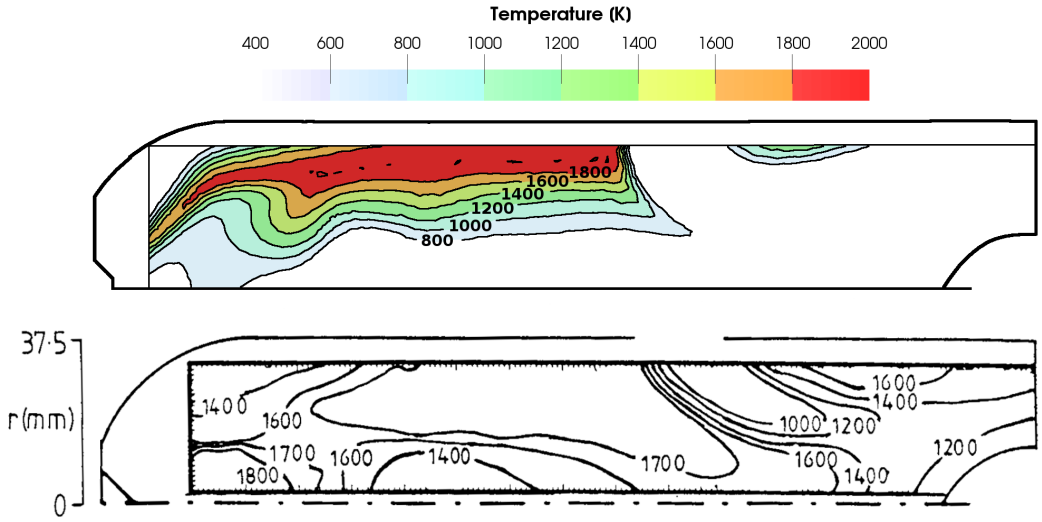

Figure 6.6.9: Temperature field comparison to experimental data - mid-vertical plane [2].

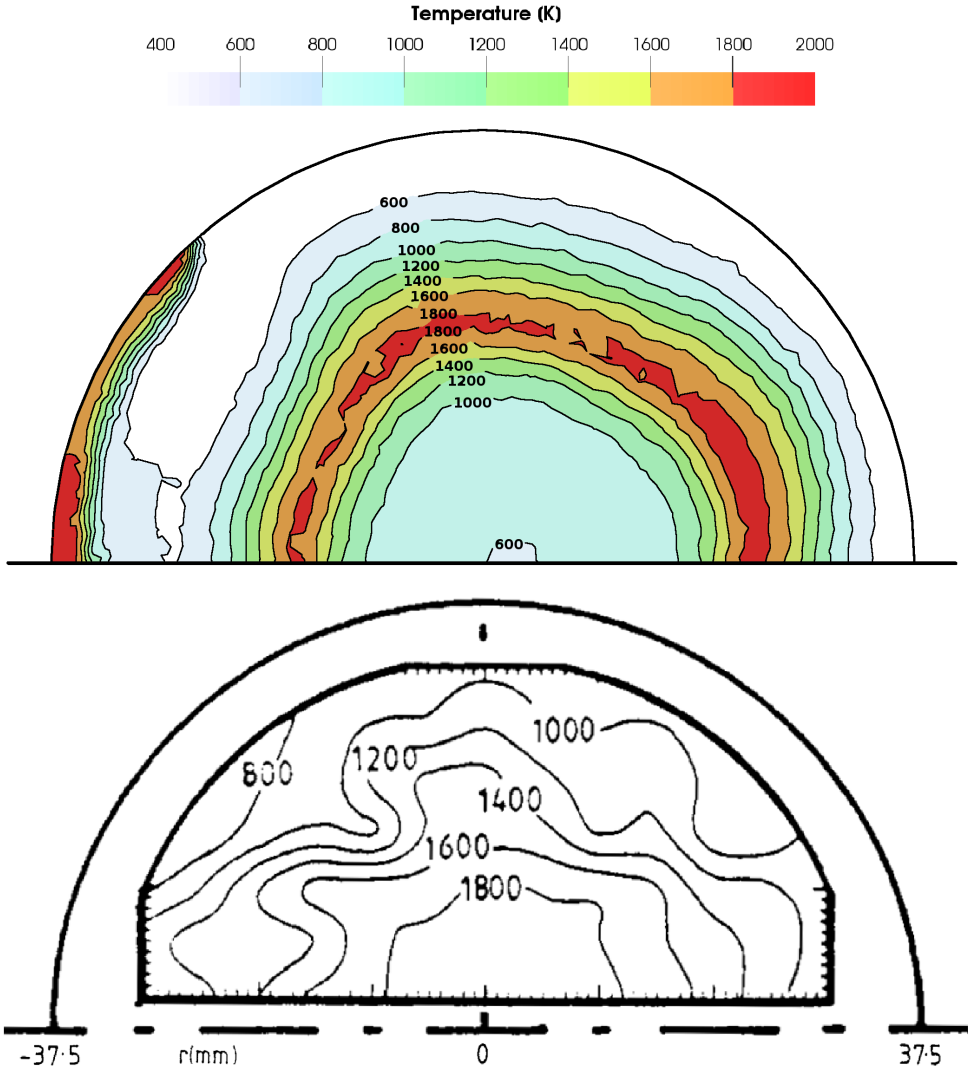

Figure 6.6.10: Temperature field comparison to experimental data - axial plane [2].

Figure 6.6.10 compares the temperature fields in the axial plane, at an axial distance of 20 mm. The secondary flame front can be seen by the increase of temperature on the left side of the combustion chamber, near the wall. Experimental results do not show a secondary flame front, as seen in Figure 6.6.10. The negative effects of the secondary flame font can be seen in Figure 6.6.11. The near wall flame front increases the wall temperature significantly. to over 2000 K. Interestingly, the secondary flame front is only present on the left side of the combustor. The effect of the dilution holes also becomes apparent, as they greatly reduce the wall temperature. Additionally, experimental results show that the peak temperature is in the middle of the combustor, while numerical results indicate that the flame front is situated at half radius.

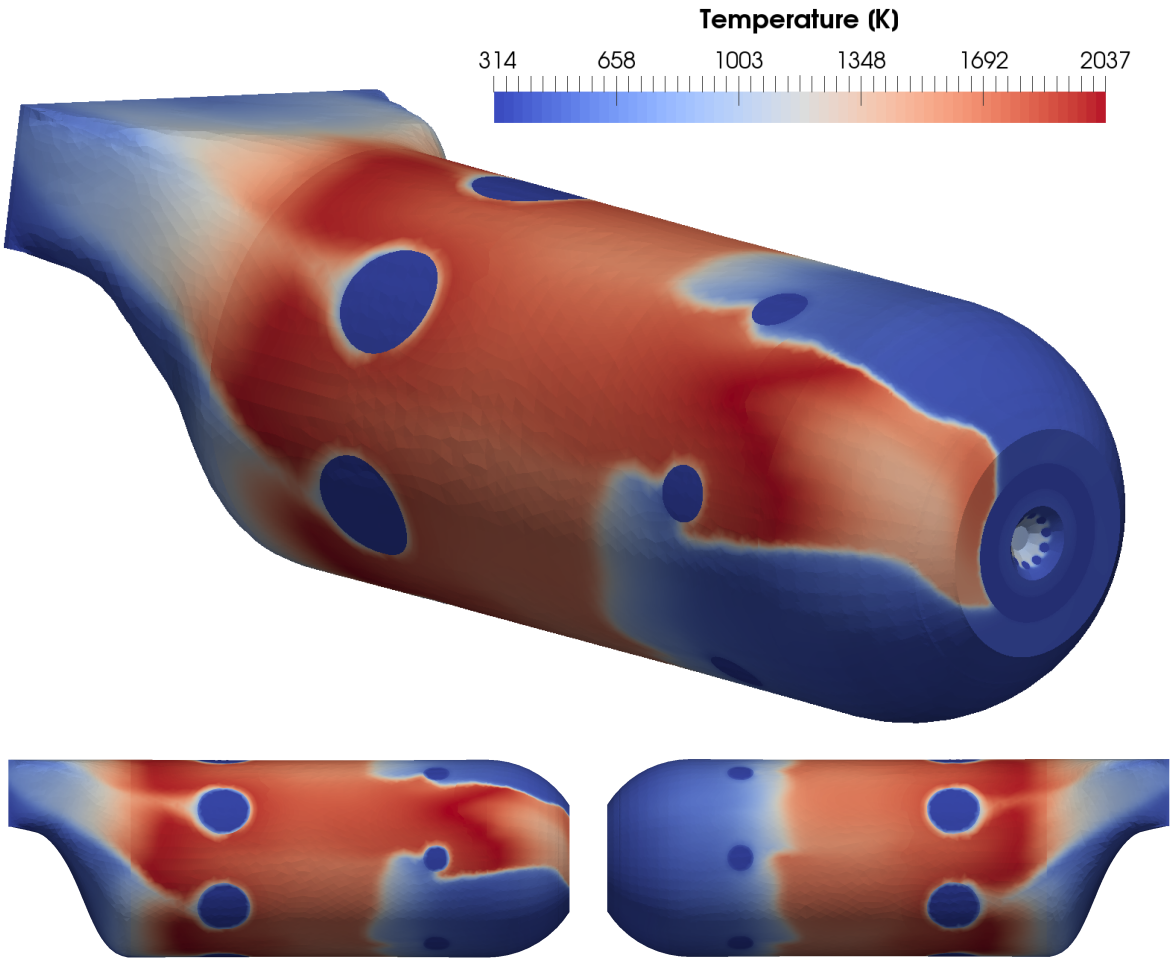

Figure 6.6.11: Combustion chamber wall temperature.

6.7 NOx Emissions

Based on the results of the simulation described in Section 6.6.4, NOx emissions are calculated using the extended Zeldovich mechanism. Figure 6.7.1 shows the NO field which coincides with the flame front shows on Figure 6.6.9. No experimental data is available to compare the NO concentration, however, the ICAO database [13] contains the emission indexes of several regulated pollutants of all operating engines. The emissions index is expressed as grams of pollutants per kilogram of fuel. Data is available for take off, climb out, approach and idle operating conditions. NOx index emission data is available for several variants of the RR Tay engine, ranging from 16.45 to 21.1 in take off conditions. Integrating the NO source term (Equation (3.2.2)) for flow configuration 2, the calculated NOx emission index is 66.90. The overprediction of NO by the extended Zeldovich mechanism can be attributed to the higher flame temperature and larger flame front than in realistic operating conditions.

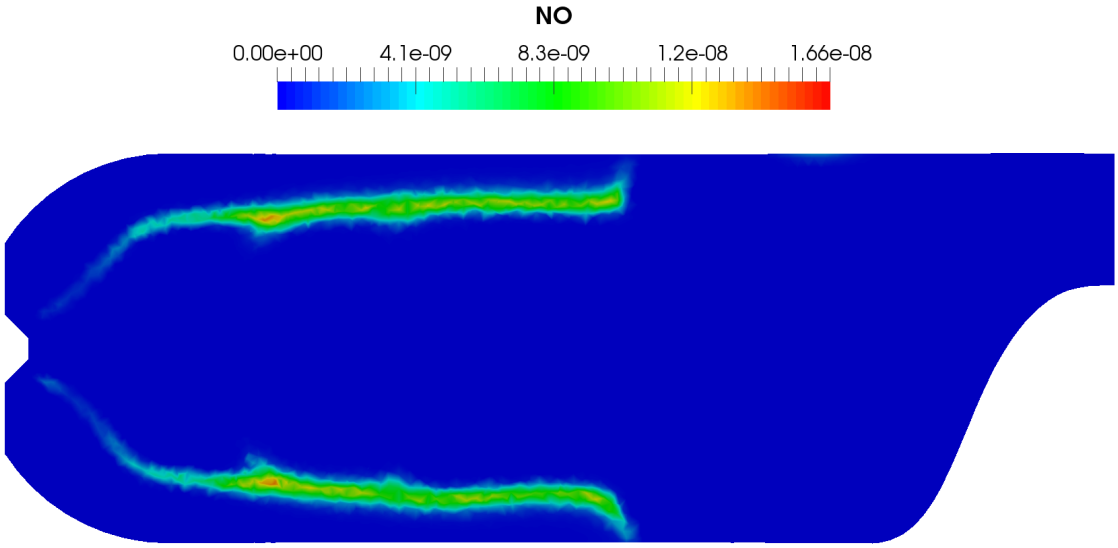

Figure 6.7.1: Concentration of NO computed using the extended Zeldovich mechanism.

6.8 Conclusion

The numerical combustion simulations performed on the Rolls Royce Tay combustion chamber at take off conditions are presented in this chapter. Two flow configurations, suggested by previous research, are simulated and the results are compared to experimental data.
Firstly, the transient non-combusting case is presented. The k-ε turbulence model is capable of correctly calculating the flow field using an unstructured mesh. The resulting flow field matches the experimental data well, reproducing both the main and secondary recirculation zone. The accurate reproduction of the flow field is an integral prerequisite to accurately simulate combustion. Next, the flow field is examined after combustion starts. The combustion is initiated by increasing the inlet fuel temperature. The resulting flame front is stationary and located near the injector holes. The propagation and dissipation of the pressure wave caused by combustion is observed.
By removing the ignition source, the auto ignition of the flame is examined in Section 6.6.3. Flow configuration 1 has an increased swirler mass flow, causing the flame front to be dissipated. More realistic results are calculated when using the second flow configuration, which has a reduced flow through the swirler and primary holes. When comparing the numerical simulation results with experimental data the following is concluded:

- the temperature is overpredicted in the entire domain, likely because radiation was not accounted for, or because of the reduced propane reaction mechanism,
- the primary combustion zone is not captured properly by the simulation. The conic shape is only slightly affected by the recirculation zone,
- the flame front by the injectors is blown out to the wall of the combustion chamber, increasing wall temperature. Possible explanations are the slower flame speed of the reduced reaction mechanism, or the exclusion of porous walls which would direct the flow inwards,

The extended Zeldovich overpredicts the production of NO by a factor of three. Possible causes are the increased combustion temperature and larger flame front in numerical simulations.

Chapter 7

Conclusion

A finite volume based CFD software package called foam-extend is used to simulate combustion is jet engine combustion chambers. The partially stirred reactor model, coupled with the k-ε turbulence model, is validated using Sandia Flame D, a piloted methane flame.

The influence of three-dimensional effects is examined, concluding they can be neglected if axisymmetric boundary conditions are present. Results of simulations using reaction mechanisms of increasing complexity are compared to experimental data, and it is concluded that reduced reaction mechanisms are able to accurately predict main flow characteristics. The extended Zeldovich mechanism is applied to the simulation results and compared with experimental data to determine the influence of reaction mechanism complexity on NOx formation. The extended Zeldovich mechanisms presented the best results when paired with a reduced reaction mechanism.

Numerical combustion simulations are performed on the Rolls Royce Tay geometry, for two flow configurations at take off conditions. At higher swirler mass flow, the flame is extinguished after ignition. Using the configuration with a lower swirl mass flow, a stable conic flame front is developed. Numerical simulations are able to calculate the main flow features. However, part of the flame is directed towards the combustor walls, increasing the wall temperature. The difference between simulation results and experimental data can be attributed to several causes: excluding of radiation heat transfer, neglecting the porosity of the combustor walls and using a reduced fuel chemical mechanism. The extended Zeldovich mechanism is able to predict NOx production with reasonable accuracy, compared to ICAO emissions data.

Future studies should implement radiative and conductive heat transfer and analyse its influence on the Sandia Flame D and Rolls Royce Tay temperature field. Furthermore, appropriate boundary conditions for porous walls should be implemented and their influence on the flow field of the RR Tay engine should be examined. The two-reaction propane reaction mechanism should be validated using experimental data and compared to a more complex reaction mechanism, such as the GRI-Mech 3.0 reaction mechanism.

Bibliography

[1] J. M. L. M. D. Palma, "Mixing in Non-reacting Gas Turbine Combustor Flows," 1989.

[2] A. F. Bicen, D. G. N. Tse, and J. H. Whitelaw, "The Influence of Air/Fuel Ratio and Swirl Number on the Combustion Characteristics of a Model Combustor," in *ASME 1990 International Gas Turbine and Aeroengine Congress and Exposition*, p. V003T06A003, Citeseer, 2015.

[3] FAA, U. O. of Environment, and Energy, "Aviation & Emissions: A Primer," 2005.

[4] R. Barlow and J. Frank, "Piloted CH4/Air Flames C, D, E, and F-Release 2.0," *Sandia National Laboratories CA*, 2003.

[5] Rolls Royce, "Rolls-Royce Tay Engine Information." `https://www.rolls-royce.com/products-and-services/civil-aerospace/business-aviation/tay.aspx`; Accessed: 01.03.2019.

[6] N. J. Wilson, "Developing the Rolls-Royce Tay," in *ASME 1988 International Gas Turbine and Aeroengine Congress and Exposition*, pp. V002T02A017—-V002T02A017, American Society of Mechanical Engineers, 1988.

[7] Stephen R. Turns, "An Introduction to Combustion: Concepts and Applications," *Mechanical Engineering Series. McGraw Hill,*, vol. 33, no. 20, pp. 5823–5828, 2008.

[8] Foam-extend, "Foam-extend Source Files." `https://github.com/Unofficial-Extend-Project-Mirror/foam-extend-foam-extend-4.0`; Accessed: 21.02.2019.

[9] T. Poinsot and D. Veynante, *Theoretical and Numerical Combustion*, vol. 53. RT Edwards, Inc., 2013.

[10] B. E. Jones, W. P. and Launder, "The Prediction of Laminarization with a Two-equation Model of Turbulence," *International journal of heat and mass transfer*, vol. 15, no. 2, pp. 301–314, 1972.

[11] M. Rahimi, G. Esposito, H. Chelliah, and S. Pope, "Chemical Kinetic Model Reduction Based on Partially-Stirred Reactor Simulations with Comparable Chemical and Mixing Time Scales," in *51st AIAA Aerospace Sciences Meeting including the New Horizons Forum and Aerospace Exposition*, p. 155, 2013.

[12] Y. B. Zeldovich, "The Oxidation of Nitrogen in Combustion Explosions," *Acta Physicochimica U.S.S.R.*, vol. 21, pp. 577–628, 1946.

[13] International Civil Aviation Organization, "ICAO Aircraft Engine Emissions Databank - Introduction," 2012. `https://www.easa.europa.eu/easa-and-you/environment/icao-aircraft-engine-emissions-databank`; Accessed: 12.03.2019.

[14] Rolls Royce, *The Jet Engine 5th Edition*. John Wiley & Sons, 1996.

[15] University of California, Berkeley, "GRI-Mech 3.0 Source Files." `http://combustion.berkeley.edu/gri-mech/version30/text30.html`; Accessed: 28.02.2019.

[16] W. Versteeg, H.K. and Malalasekera, *An Introduction to Computational Fluid Dynamics: the Finite Volume Method.* Pearson Education, 2007.

[17] D. G. N. Tse, "Flow and Combustion Characteristics of Model Annular and Can-type Combustors," 1988.

[18] J. J. McGuirk and J. M. L. M. Palma, "The Flow Inside a Model Gas Turbine Combustor: Calculations," *Journal of Engineering for Gas Turbines and Power*, vol. 115, no. 3, p. 594, 2008.

[19] J. J. McGuirk and J. M. Palma, "The Influence of Numerical Parameters in the Calculation of Gas Turbine Combustor Flows," *Computer Methods in Applied Mechanics and Engineering*, vol. 96, no. 1, pp. 65–92, 1992.

[20] P. Koutmos, "An isothermal study of gas turbine combustor flows," 1985.

[21] H. Nguyen and S.-J. Ying, "Critical Evaluation of Jet-A spray Combustion Using Propane Chemical Kinetics in Gas Turbine Combustion simulated by KIVA-II," in *26th Joint Propulsion Conference*, p. 2439, 2013.

[22] A. Fick, "V. On liquid diffusion," *The London, Edinburgh, and Dublin Philosophical Magazine and Journal of Science*, vol. 10, no. 63, pp. 30–39, 1855.

[23] W. Sutherland, " LII. The viscosity of gases and molecular force ," *The London, Edinburgh, and Dublin Philosophical Magazine and Journal of Science*, vol. 36, no. 223, pp. 507–531, 2011.

[24] B. Collonval, *Modeling of Auto-ignition and NOx Formation in Turbulent Reacting Flows*. PhD thesis, Dissertation, Technische Universität München, München, 2015.

[25] R. C. Reid, T. K. Sherwood, and R. E. Street, "The Properties of Gases and Liquids," *Physics Today*, vol. 12, no. 4, pp. 38–40, 2009.

[26] F. D. Rossini, "JANAF thermochemical tables," Tech. Rep. 3, National Standard Reference Data System, 2004.

[27] D. C. Wilcox, *Turbulence Modeling for CFD, 3rd edition*, vol. 2. DCW industries La Canada, CA, 2006.

[28] Launder B. E. and Spalding D. B., "The Numerical Computation of Turbulent Flows," in *Computer Methods in Applied Mechanics and Engineering*, vol. 3, pp. 269–289, Elsevier, 1974.

[29] K. Lindenberg, R. Metzler, and G. Oshanin, *Chemical Kinetics*. No. 544.4 LAI, 2018.

[30] R. J. Kee, F. M. Rupley, E. Meeks, and J. a. Miller, "1ss Chemkin-III: a Fortran Chemical Kinetics Package for the Analysis of Gas-phase Chemical and Plasma Kinetics," Tech. Rep. May, Sandia National Labs., Livermore, CA (United States), 1996.

[31] A. Imren and D. C. Haworth, "On the Merits of Extrapolation-based Stiff ODE Solvers for Combustion CFD," *Combustion and Flame*, vol. 174, pp. 1–15, 2016.

[32] D. B. Spalding, "Combustion Mixing and Chemical Reaction in Steady Confined Turbulent Flames," in *Symposium (International) on Combustion*, vol. 13, pp. 649–657, Elsevier, 1971.

[33] P. Taylor, I. S. Ertesvag, and B. F. Magnussen, "The Eddy Dissipation Turbulence Energy Cascade Model The Eddy Dissipation Turbulence Energy Cascade Model," *Combustion Science and Technology*, vol. 159, no. 1, pp. 213–235, 2007.

[34] P. A. N. Nordin, *Complex Chemistry Modeling of Diesel Spray Combustion*, vol. 18. Chalmers University of Technology Sweden, 2001.

[35] Magnussen, Bjørn F., "The Eddy Dissipation Concept—A Bridge Between Science and Technology," in *ECCOMAS Thematic Conference on Computational Combustion*, vol. 21, p. 24, Libson, Portugal, 2005.

[36] D. Christ, "The Effect of Char Kinetics on the Combustion of Pulverized Coal Under Oxyfuel Conditions," tech. rep., Lehrstuhl für Wärme-und Stoffübertragung, 2013.

[37] S. M. Correa, "Turbulence-Chemistry Interactions in the Intermediate Regime of Premixed Combustion," *Combustion and Flame*, vol. 93, no. 1-2, pp. 41–60, 1993.

[38] A. Stagni, A. Cuoci, A. Parente, and T. Faravelli, "A Partially Stirred Reactor Model for Turbulent Combustion Closure Using Detailed Chemical Time Scales," 2018.

[39] R. C. Flagan and J. H. Seinfeld, *Fundamentals of Air Pollution Engineering*. Courier Corporation, 1988.

[40] Y. Ohtake, "Degradation of Vulcanised Rubber Products – Problems and Solutions (Degradation by Residual Chlorine in Tap Water, Metals and Ozone Due to Deterioration in the Global Environment)," *International Polymer Science and Technology*, vol. 34, no. 4, pp. 57–67, 2018.

[41] L. Stan and D. Mitu, "Simplified Mechanism Used to Estimate the NOx Emission of Diesel Engine," in *2nd International Conference on Manufacturing Engineering, Quality and Production Systems*, pp. 61–64, 2010.

[42] J. Warnatz, R. W. Dibble, and U. Maas, *Combustion, Physical and Chemical Fundamentals, Modeling and Simulation*. Springer, 4th ed., 1996.

[43] F. Moukalled, L. Mangani, and M. Darwish, "Erratum to: The Finite Volume Method in Computational Fluid Dynamics," *An Advanced Introduction with OpenFOAM and Matlab*, pp. E1–E1, 2016.

[44] H. Jasak, "Error Analysis and Estimation for the Finite Volume Method with Applications to Fluid Flows," *02.02.00_Cfd*, vol. M, no. June, p. 394, 1996.

[45] OpenFOAM, "OpenFOAM Documentantion." `https://openfoam.org`; Accessed: 21.02.2019.

[46] A. Jasak, Hrvoje and Jemcov and Z. Tukovic, "OpenFOAM : A C++ Library for Complex Physics Simulations," in *International Workshop on Coupled Methods in Numerical Dynamics*, vol. m, pp. 1–20, IUC Dubrovnik Croatia, 2007.

[47] ParaView, "ParaView User Guide," 2012. `https://www.paraview.org/paraview-guide/`; Accessed: 21.02.2019.

[48] OpenFOAM_guide, "OpenFOAM User Guide," 2014. `https://cfd.direct/openfoam/user-guide/v6-thermophysical/`; Accessed: 21.02.2019.

[49] D. Christ, "Simulating the Combustion of Gaseous Fuels," in *Presentation*, pp. 1–45, 2011.

[50] G. Ermentrout, *Numerical Recipes in C*, vol. 93. Cambridge university press Cambridge, 2002.

[51] CHEMKIN®-Software, "CHEMKIN Tutorials Manual," 2011. `https://www.ems.psu.edu/~radovic/ChemKin_Tutorial_2-3-7.pdf`; Accessed: 24.02.2019.

[52] B. University of California, "GRI-Mech 3.0 Source Files." `http://combustion.berkeley.edu/gri-mech/version30/text30.html`; Accessed: 28.02.2019.

[53] B. J. Mcbride, S. Gordon, and M. A. Reno, "NASA Technical Memorandum 4513, Coefficients for Calculating Thermodynamic and Tansport Properties of Individual Species," 1993.

[54] I. Poinwise, "Pointwise User Guide," 2012. `https://www.pointwise.com/doc/user-manual/index.html`; Accessed: 28.02.2019.

[55] A. Abdalla, D. Bradley, S. Chin, and C. Lam, "Global Reaction Schemes for Hydrocarbon Oxidation," *Oxidation Communication*, vol. 4, no. 3, pp. 113–130, 1983.